THE UNIVERSITY OF MANITOBA

STABLE CRACK GROWTH IN DUCTILE MATERIALS - A FINITE ELEMENT APPROACH

by

Young-Jin Kim

A Thesis
Submitted to the Faculty of Graduate Studies
in Partial Fulfillment of the Requirements for the Degree
of Doctor of Philosophy

Department of Mechanical Engineering

Winnipeg, Manitoba

November 1981

STABLE CRACK GROWTH IN DUCTILE MATERIALS

- A FINITE ELEMENT APPROACH

BY

YOUNG-JIN KIM

A thesis submitted to the Faculty of Graduate Studies of
the University of Manitoba in partial fulfillment of the requirements
of the degree of

DOCTOR OF PHILOSOPHY

ABSTRACT

This thesis presents a new and flexible procedure for analyzing stable crack growth in ductile materials. The analysis is based on an elastic-plastic finite element method which calculates the stress and displacement fields in the vicinity of a growing crack under monotonically increasing loads. A special type of element known as a 'breakable element' together with a nodal force relaxation technique has been incorporated into the usual finite element program in order to simulate stable crack growth. The effective strain value at the crack tip is used as a fracture criterion, and subsequently for mixed mode crack problems is further utilized to assess the direction of crack extension.

An experimental program which generated applied stress vs stable crack growth curves for center-cracked aluminum sheets was undertaken to verify the numerical results. Experiments were conducted for both the mode I and the mixed mode loading conditions.

Numerical studies verified that the proposed algorithm successfully both modelled the stable crack growth and

predicted unstable crack growth. Varying stress and strain distributions in the region of the crack tip were analyzed phenomenologically, and various crack tip parameters were evaluated and assessed as fracture criteria.

ACKNOWLEDGEMENT

The author wishes to express his deepest gratitude to Dr. T.R. Hsu for the valuable advice and guidance throughout the course of the study. Sincere appreciation is also due to Dr. J. Shewchuk, Dr. R.B. Pinkney and Dr. A.S. Kobayashi for their valuable suggestions.

Thanks are also extended to his colleagues; Messrs. G. Pizey, B. McAllister and D. Scarth for their useful discussions and constructive criticisms. The technical assistance by Mr. D. Fedorowich during the experimental study is also appreciated.

The financial support provided by the University of Manitoba and Atomic Energy of Canada Limited are greatly acknowledged.

Above all, the author would like to thank his wife Shin-In for her patience during long period of the study and preparation of this dissertation and also his father and mother in Korea for their sincere support and encouragement across the thousands of miles that separate us.

TABLE OF CONTENTS

LIST OF TABLES

LIST OF FIGURES

NOMENCLATURE

a, a_o	Crack length and initial crack length respectively
a_1, a_2, etc. a_{11}, a_{22}, etc.	Mathematical constants
Δa	Increment of crack length
A	Cracked area
B	Thickness of the specimen
$[B]$	Stress-displacement transformation matrix
C	New crack location in Dugdale model
$[C]$	Stress-strain constitutive matrix
$[C^e]$, $[C^{ep}]$	Elastic and elastic-plastic matrices respectively
d	Distance from the crack tip
E, E_o	Elastic modulus
E'	Plastic modulus
F	Nodal reaction force
G	Strain energy release
H'	Slope of the tangent to $\bar{\sigma}$ - $\bar{\varepsilon}^p$ curve
I	Intensely non-linear zone inside the plastic zone
J	Path-independent contour integral
J_2	Second deviatoric stress invariant
k	Work hardening parameter
K	Stress intensity factor
K_I, K_{II}, K_{III}	Mode I, Mode II and Mode III K respectively

K_C, K_{IC}	Plane stress and plane strain fracture toughnesses respectively
K_R	Crack growth resistance
K_G	Crack driving force
$[K]^e$, $[K]$	Element and global stiffness matrices respectively
n	Power hardening coefficient in the stress-strain law
{N}	Matrix containing the interpolation (or shape) function
P	Applied load
{q}	Nodal displacement vector
{Q}	Global vector of applied nodal forces
r_y	Half plastic zone
R	Crack growth resistance curve
ds	Differential element of an arc length along the contour path
S	Strain energy density factor
T	Surface traction vector for J-integral evaluation
u	Displacement
{u}, {Δu}	Displacement and incremental displacement vectors respectively
U	Potential energy
v	Volume of the element
w	Strain energy density function
W	Width of the specimen
x,y,z r,θ	Coordinate system

α_o	Crack opening angle
α_ℓ	Crack tip opening angle
β	Inclined crack angle in mixed mode
Γ	Contour path in J-integral evaluation
δ	Crack opening displacement
δ_i, δ_c	Crack opening displacement at crack initiation and unstable crack growth respectively
ε_{xx}, ε_{yy}, ε_{zz}, etc.	Strain components
$\bar{\varepsilon}$, $\bar{\varepsilon}_p$	Effective strain and effective plastic strain
$\bar{\varepsilon}_{ext.}$	Extrapolated strain at the crack tip
$\bar{\varepsilon}_{rup.}$	Rupture strain
$\{\varepsilon\}, \{\delta\varepsilon\}$	Strain and incremental strain vectors respectively
$\{\delta\varepsilon^e\}$, $\{\delta\varepsilon^p\}$	Elastic and plastic components of strain increment respectively
θ_o	Angle between the crack line and crack initiation direction
κ	Material constant
$d\lambda$	Proportionality factor
ν	Poisson's ratio
σ_{xx}, σ_{yy}, σ_{xy}, etc.	Stress components
$\bar{\sigma}$	Effective stress
σ_k	Auxiliary stress close to the elastic-plastic transition
σ_{ys}	Yield strength of the material
σ'_{ij}	Deviatoric stress components
μ	Shear modulus

$\{\sigma\}$	Stress vector
τ_{ys}	Experimentally determined yield stress in pure shear
ASTM	American Society for Testing and Materials
COA	Crack Opening Angle
COD	Crack Opening Displacement
CTOA	Crack Tip Opening Angle
LEFM	Linear Elastic Fracture Mechanics
TEPSA	Thermo Elasto-Plastic Stress Analysis

CHAPTER 1

INTRODUCTION

1.1 Introduction

A well known fact in the engineering field is that many structures contain flaws or cracks, either from the time of fabrication or due to adverse loading conditions in service. A major concern for design engineers is the potential growth of these flaws or cracks which may, under particular loading conditions, trigger a catastrophic failure. A useful design methodology for the assessment of such structural integrity and materials selection problems is the engineering science of fracture mechanics [1, 2]+.

During the past decade, the linear elastic fracture mechanics (LEFM) approach has attained a high level of sophistication and acceptance by design engineers for the analysis of brittle fracture problems, in which the onset of crack growth is usually tantamount to crack instability and structural failure. However, there exists a large class of fracture problems involving the fracture of ductile materials which cannot be characterized completely by LEFM.

+Numbers in the bracket denote the references at the end of the thesis.

Consider a large sheet of ductile material with a through-the-thickness crack subjected to a monotonically increasing load. The plate of width, W, illustrated in Fig. 1.1(a) contains a central crack of length $2a_0$. The axial tensile load, P, produces a uniform stress, σ, at some distance far from the crack. The initial crack of half length, a_0, at a particular load will undergo an extension to a new stable length, $a_0 + \Delta a$. As the load increases further, this process of 'stable crack growth' may be repeated several more times. Finally, a combination of applied stress and crack length is reached such that stable crack growth continues without a further load increase. This transition, the onset of rapid crack growth, generally leads to complete fracture of the sheet.

This experiment shows that under a monotonically increasing load to failure ductile materials experience considerable plastic deformation at the crack tip and a significant amount of stable crack growth prior to the onset of unstable fracture. Thus, a substantial margin of safety may still exist even when the onset of crack growth is imminent. As a consequence of this high resistance to catastrophic failure, ductile sheet materials are used widely in the aerospace and other industries. The obvious requirement for rigorous design safety in these industries

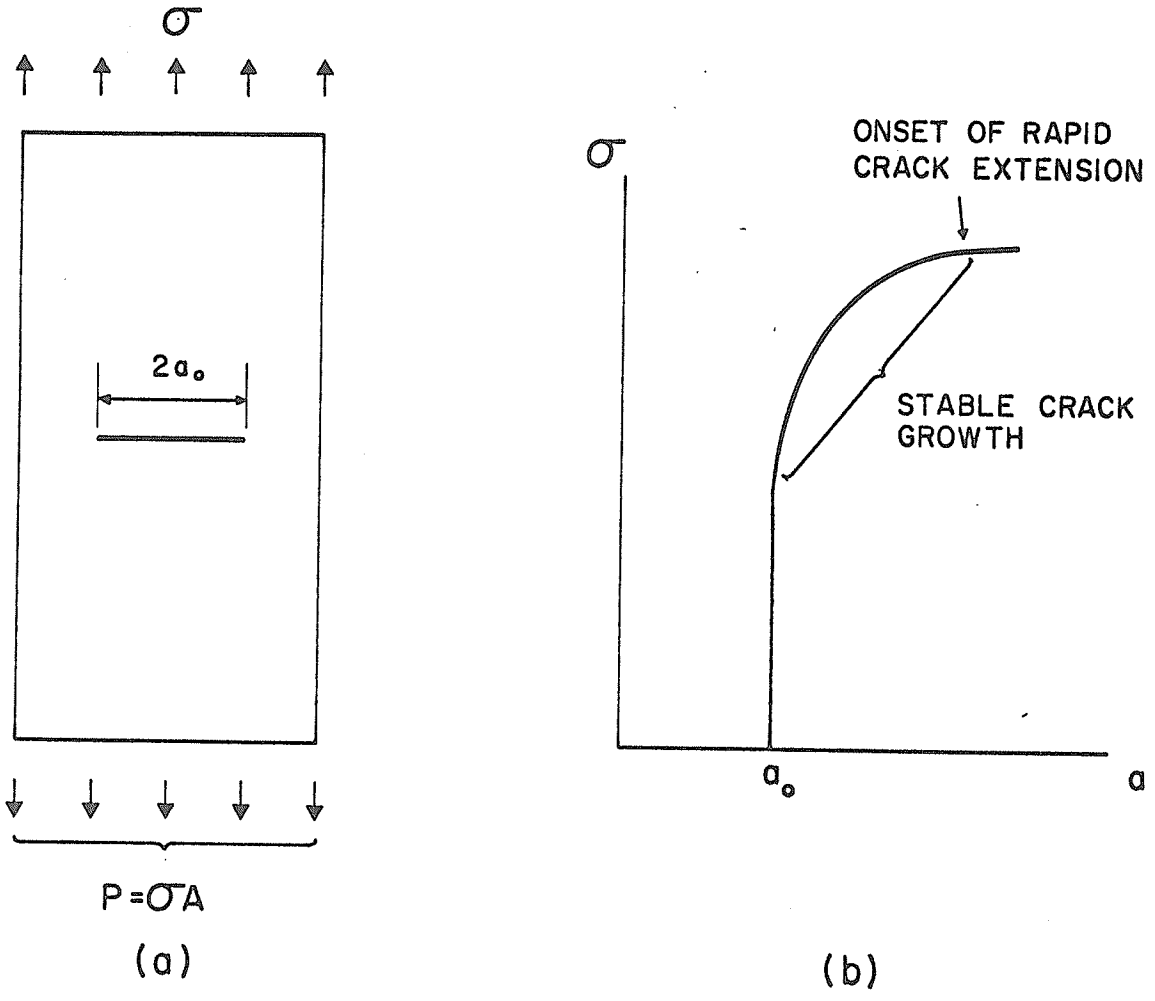

Fig. 1.1 Stable Crack Growth Under Increasing Load

(a) Geometry of the Specimen
(b) Applied Stress vs Stable Crack Growth Curve

demands both a detailed understanding of the mechanism of stable crack growth, and an accurate procedure for predicting unstable fracture.

Attempts at extending the LEFM approach into the stable crack growth regime are precluded by its inability to treat the inelastic effects arising from large scale plasticity and material unloading. In recent years the increasing sophistication of digital computers has enhanced the selection of numerical solution procedures as an alternative to the mathematical complexities inherent in the continuum description of a growing crack. Chief among these numerical techniques is the finite element method, a powerful and widely used technique for elastic-plastic stress analysis problems. This method has been used to obtain useful information such as the stress, strain distribution about the crack tip and the fracture criterion governing the crack tip. While some recent attempts at predicting the unstable fracture of ductile materials have been made, to date no reasonable correlation has been observed between numerical and experimental results under plane stress conditions.

1.2 Objective of Thesis

This thesis describes a research effort leading to an elastic-plastic fracture mechanics methodology designed to treat large-scale yielding and stable crack growth problems. Due to slant-type fracture, the fracture of sheet material is a three-dimensional problem. However, for simplicity a two-dimensional model has been assumed. An elastic-plastic stress analysis based on the finite element variational technique was used to determine the distribution of the stress and deformation fields associated with an extending crack tip under plane stress conditions. The key element of the research is the development of a numerical technique which simulates stable crack growth in ductile materials. The proposed rupture strain criterion is suitable not only for mode I fracture problem but also for determining the direction of crack propagation in the mixed mode fracture problem.

1.3 Scope of Thesis

The thesis is divided into eight chapters.

Chapter 1 is an introduction to the field of stable crack growth.

Chapter 2 is a general review of the development of fracture mechanics concepts and computational fracture mechanics.

Chapter 3 describes the finite element formulations in elastic-plastic stress analysis.

Chapter 4 presents a numerical modelling technique for stable crack growth.

Chapter 5 is devoted to a description of the experimental program which was carried out to check the accuracy of the numerical analysis.

Chapter 6 presents the results of the case study for mode I fracture problem.

Chapter 7 presents the results of the case study for mixed mode fracture problem.

Chapter 8 is the conclusions and recommendations for further study.

A bibliography is presented at the conclusion of the thesis.

CHAPTER 2

REVIEW ON FRACTURE MECHANICS CONCEPTS AND COMPUTATIONAL FRACTURE MECHANICS

2.1 Introduction

The mechanisms of fracture which may be encountered in engineering structures can be classified into two general groups. The first category is termed 'brittle fracture', which occurs in brittle materials such as glass, or in mild steel at very low temperature. Brittle fracture may also occur in most other engineering materials under very high loading rates or under the 'plane strain' conditions encountered in heavy sectioned structural parts where the dimensions of the original defect are small compared to the characteristic dimensions of the part. This type of fracture is associated with relatively low fracture energy (i.e. the input energy required to propagate the crack) and small plastic deformation prior to and during crack extension. The second type of fracture falls into the general category of 'ductile fracture' or high energy fracture[+], and usually

[+]The term 'high energy' refers to the high input energy required to propagate the crack (usually dissipated as heat), and should not be confused with the high time rate of energy input as occurs in dynamic fracture.

occurs in non-brittle materials under 'plane stress' conditions. For example, thin-walled tubes and shell structures, composed of materials with high ductility, would be expected to undergo large plastic deformation prior to and during a rupture process.

Research in the field of fracture mechanics was initially concerned with investigating brittle fracture problems, since these types of failures are of more disastrous consequences and easier to analyze than ductile fracture cases. In this chapter, the concept of linear elastic fracture mechanics (LEFM) is briefly described, and the current level of development of elastic-plastic fracture mechanics is also discussed. A review of the literature on the application of the finite element method to fracture mechanics problems is presented at the end of this chapter.

2.2 Linear Elastic Fracture Mechanics

The linear elastic fracture mechanics approach to evaluating stresses and displacements associated with each fracture mode follows the Griffith-Irwin theory [1, 2]. In this approach, the general stress field near a crack tip can be expressed as the superposition of stress fields due

to the three modes of fracture, each mode associated with a kinematic movement of two crack surfaces relative to each other. These deformation modes, illustrated in Fig. 2.1 are denoted as the opening mode, the edge sliding mode and the tearing mode.

- The opening mode (mode I) is associated with local displacements in which the crack surfaces move apart in a direction perpendicular to these surfaces (symmetric with respect to the x-y and z-x planes).
- The edge sliding mode (mode II) is characterized by displacements in which the crack surfaces slide over one another and remain perpendicular to the leading edge of the crack. (symmetric with respect to the x-y plane and skew-symmetric with respect to the z-x plane).
- The tearing mode (mode III) is defined by the crack surfaces sliding with respect to one another parallel to the leading edge of the crack. (skew-symmetric with respect to the x-y and x-z planes).

Griffith theory [4], first proposed in 1921, was based on the assumption that incipient fracture in ideally brittle materials occurs when the magnitude of the elastic

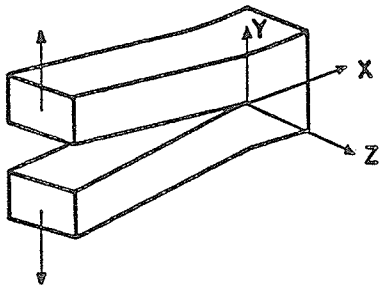

(a)

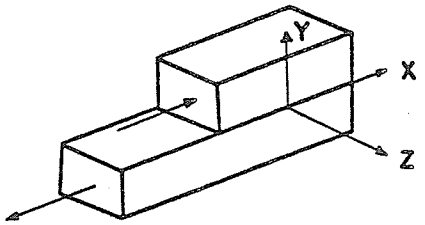

(b)

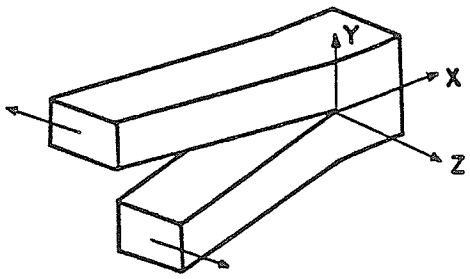

(c)

Fig. 2.1 Three Modes of Fracture
(a) Mode I (b) Mode II (c) Mode III

energy supplied to the crack tip during an incremental increase in crack length exceeds the magnitude of the energy required to create the new crack surface during the same incremental increase in crack length. This strain energy release rate G, or the elastic energy made available per unit extension of the crack area, is:

$$G = - \frac{dU}{dA} \tag{2.1}$$

where U is the potential energy of the structure and

A is the cracked area.

In 1956, Irwin [5] developed the analytical basis of the elastic crack tip stress field theory, which in turn was the starting point of modern fracture mechanics. In his theory the stress intensity factor[+], K, is extracted from the solutions for stresses and displacements near the crack tip and is a combination of applied load P, crack length a and specimen configuration.

$$K = P \cdot f\ (a,\ \text{geometry}) \tag{2.2}$$

K is said to be the controlling parameter of a crack tip field, because stresses and displacements are proportional

---

[+] K_I, K_{II} and K_{III} are defined as mode I, mode II and mode III stress intensity factors, respectively.

to this factor. In general, the stress and displacement fields can be expressed mathematically as follows:

$$\sigma_{ij} = \frac{K}{\sqrt{r}} f_{ij}(\theta) + \ldots \qquad (2.3a)$$

$$u_i = K\sqrt{r}\, g_i(\theta) + \ldots \qquad (2.3b)$$

where r, θ is a polar coordinate system at the crack tip shown in Fig. 2.2. The truncated terms of equation (2.3) are the terms with higher order in r, and for small radius of r (i.e. very close to the crack tip), only the first term is significant. Crack extension will occur when the intensity of the stress field in the close vicinity of the crack tip reaches a critical value. This means that fracture must be expected to occur when K reaches a critical value, K_c.

Irwin et al [6] also showed that there exists a unique relationship between K and G as follows:

$$G = \frac{K^2}{E_o} \qquad (2.4)$$

in which E_o = E (plane stress)

= $E/(1-\nu)$ (plane strain)

where E is a Young's modulus and

ν is Poisson's ratio.

Thus the consistency of the two theories, Griffith theory and Irwin theory, was apparent.

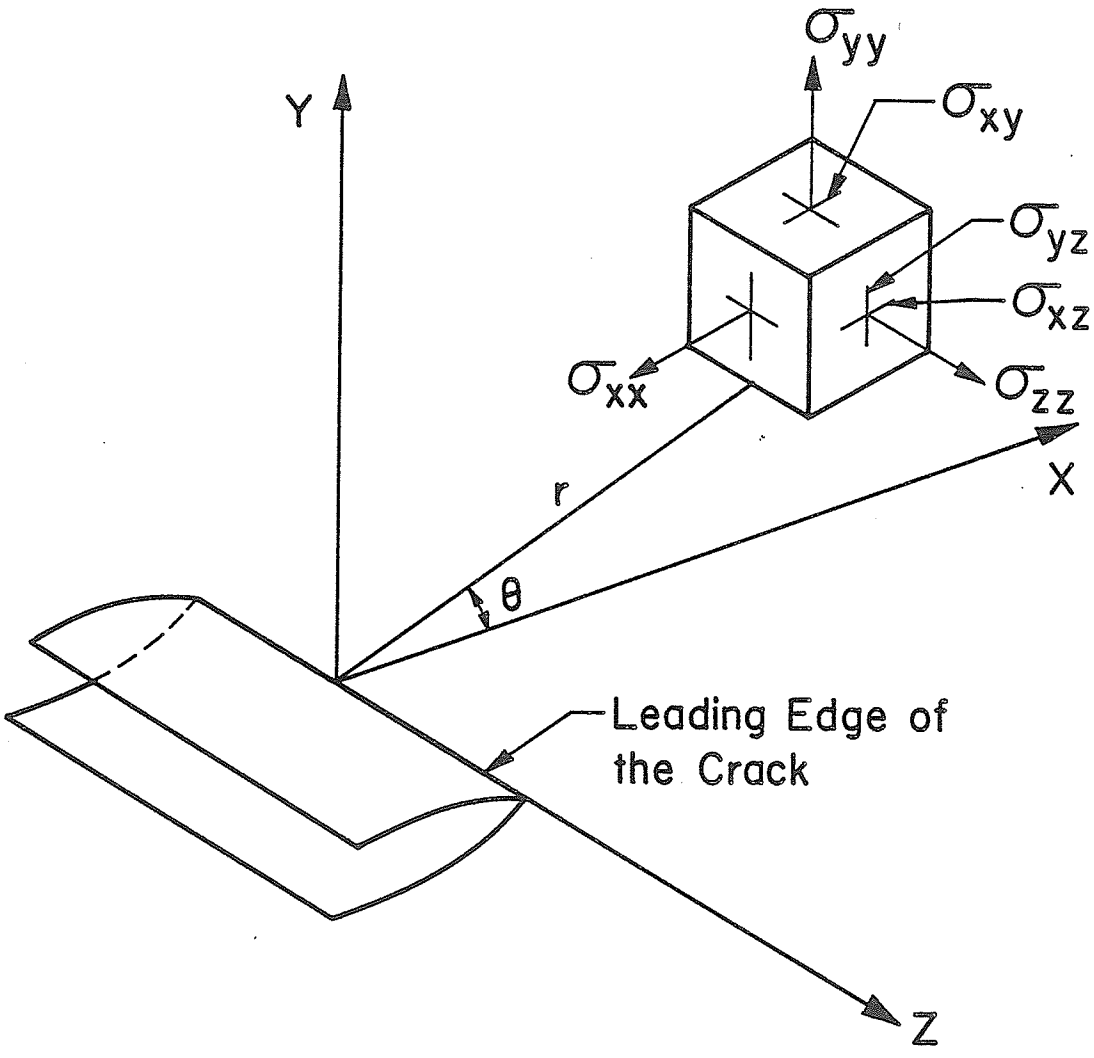

Fig. 2.2 Coordinate System at the Crack Tip.

Due to the singular nature of the equation (2.3a), a plastic zone is always formed at the crack tip where the stress field exceeds the yield strength of the material. Since equation (2.3) is based on the theory of elasticity, K has significance only when the geometry of the crack or remaining ligament exceeds the plastic zone size by a factor of about 50 [1], a criterion which is met by the plane strain condition. In order to use an experimentally determined plane strain fracture toughness K_{IC} value as a fracture criterion, the American Society for Testing and Materials (ASTM) specifies the following thickness requirement.

$$B > 2.5 \frac{K_{IC}^2}{\sigma_{ys}^2} \tag{2.5}$$

where B is the thickness of the specimen and

σ_{ys} is the yield strength of the material.

2.3 Elastic Plastic Fracture Mechanics

Most of the large complex engineering structures such as airplane frames, ships, pipelines, etc. have such small wall thickness that plane stress conditions prevail. Also, these structures are usually composed of ductile materials. Thus for many structural applications, the linear elastic analysis used to calculate the stress

intensity factor K, is invalidated by the formation of large plastic zones around the crack tip. Currently, much effort is being devoted to the development of elastic-plastic fracture mechanics analysis as an extension of LEFM [1, 2]. Among the various techniques the following approaches are most popular:

(1) Plastic zone corrections.

(2) Crack opening displacement.

(3) J-integral.

(4) Crack growth resistance R-curve.

The above techniques hold considerable promise for appraising structural integrity in terms of an allowable loading or crack size. The engineering significance of each technique is reviewed in the following sections.

2.3.1 Plastic Zone Corrections

The first attempt in extending fracture mechanics beyond the LEFM limits involved a correction to the crack length to account for the effect of the plastic zone while continuing to use the LEFM approach. This procedure, proposed by Irwin [6], involved moving the crack tip to the center of the plastic zone, a distance r_y, i.e.

$$a \rightarrow a + r_y \quad . \tag{2.6}$$

The distance r_y is evaluated as:

$$r_y = \frac{1}{2\pi} \frac{K_c^2}{\sigma_{ys}^2} \qquad \text{(plane stress)}$$
$$= \frac{1}{6\pi} \frac{K_{IC}^2}{\sigma_{ys}^2} \qquad \text{(plane strain)} \; . \tag{2.7}$$

Although Irwin's plastic zone correction gives consistent results for small scale yielding, the limits of its applicability are uncertain.

A more rigorous correction for the plastic zone size was proposed by Dugdale [7]. He assumed that yielding occurs in a thin strip-like zone at the crack tip, extending the crack by a distance c-a (Fig. 2.3). The stresses in this yielded zone are considered to be a continuous distribution of point loads, which act to restrain the crack from opening. An expression for the restraining stress intensity factor can then be obtained by integrating from a to c with the appropriate Westergaard stress function as:

$$K = 2 \sigma_{ys} \left(\frac{c}{\pi}\right)^{\frac{1}{2}} \cos^{-1} \left(\frac{a}{c}\right) \; . \tag{2.8}$$

The size of the plastic zone is obtained by equating the restraining stress intensity factor (2.8) with the K value for the opening of the crack, $K = \sigma\sqrt{\pi c}$.

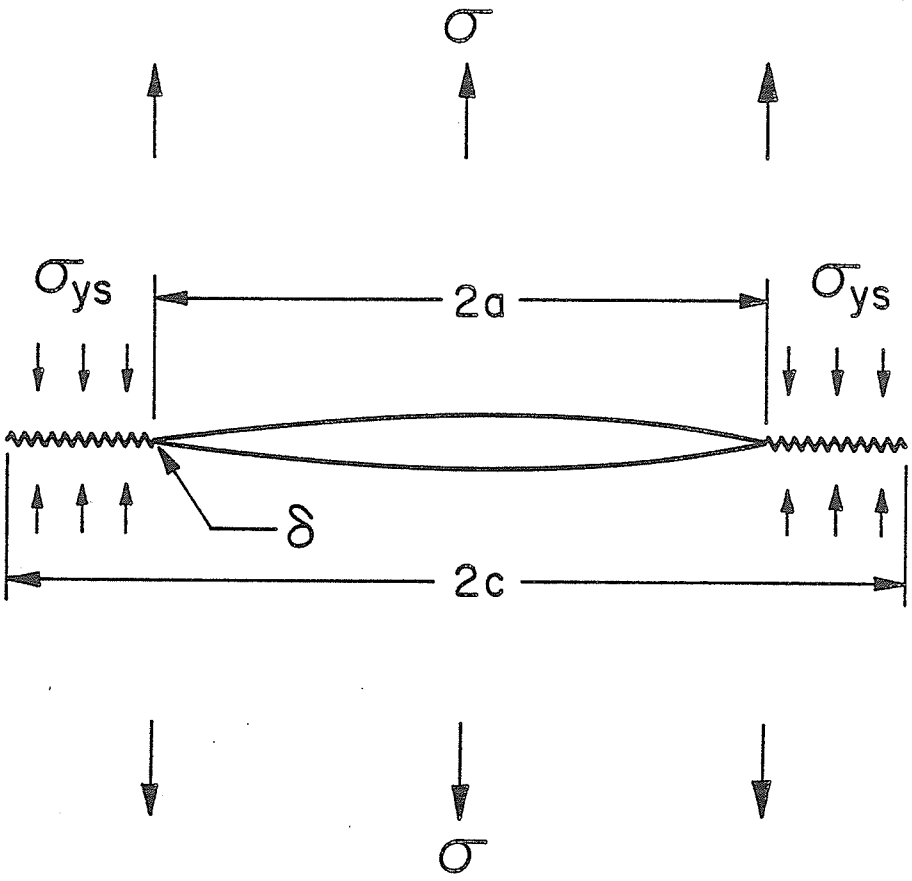

$$\frac{a}{c} = \cos\frac{\pi\sigma}{2\sigma_{ys}}$$

Fig. 2.3 Dugdale Model.

Thus

$$r_y = \frac{\pi}{16} \frac{K^2}{\sigma_{ys}^2} \quad . \tag{2.9}$$

The plastic zone size calculated by equation (2.9) is about 20% bigger than that calculated by equation (2.7) for the plane stress case.

2.3.2 Crack Opening Displacement

Wells [8] proposed that the fracture behavior in the vicinity of a crack could be characterized by the opening of the crack faces - namely the crack opening displacement (COD), as shown in Fig. 2.3. Furthermore, he showed that the COD concept was analogous to the G value, thus the COD value could be related to the plane-strain fracture toughness K_{IC}. Since COD measurement can be made when there is considerable plastic flow around the crack tip, this technique gives useful information for elastic-plastic fracture analysis.

An extension of the Dugdale analysis yields an expression for the crack opening displacement normal to the crack plane at the crack tip, δ:

$$\delta = \frac{8}{\pi} \frac{\sigma_{ys}}{E} a \, \ell n \left[\sec \frac{\pi}{2} \frac{\sigma}{\sigma_{ys}}\right] \tag{2.10}$$

which for $\sigma/\sigma_{ys} << 1$ reduces to

$$\delta = \frac{K_I^2}{\sigma_{ys} E} \quad . \tag{2.11}$$

Equation (2.11) implies that at the onset of crack instability, where K_I reaches K_{IC}, the COD value reaches a critical value δ_C. Under plane strain conditions, unstable fracture will occur upon crack initiation, and thus $\delta_i = \delta_C$. Like K_{IC}, a δ_C value under plane strain conditions is a material property, and is independent of specimen geometry. However, under plane stress conditions, stable crack growth can occur after the COD value reaching δ_i. The COD value will rise to a value designated as $\delta_{max.}$ ($> \delta_i$), upon which unstable crack extension will occur. Under plane stress conditions, values of δ_i and $\delta_{max.}$ are dependent on specimen geometry.

2.3.3 J-Integral

Rice [9] proposed a path-independent contour integral, the J-integral, for a two-dimensional deformation field, evaluated over the contour Γ in a counter-clockwise direction, as illustrated in Fig. 2.4,

$$J = \int_{\Gamma} \left(w dy - T_i \frac{\partial u_i}{\partial x} ds \right) \tag{2.12}$$

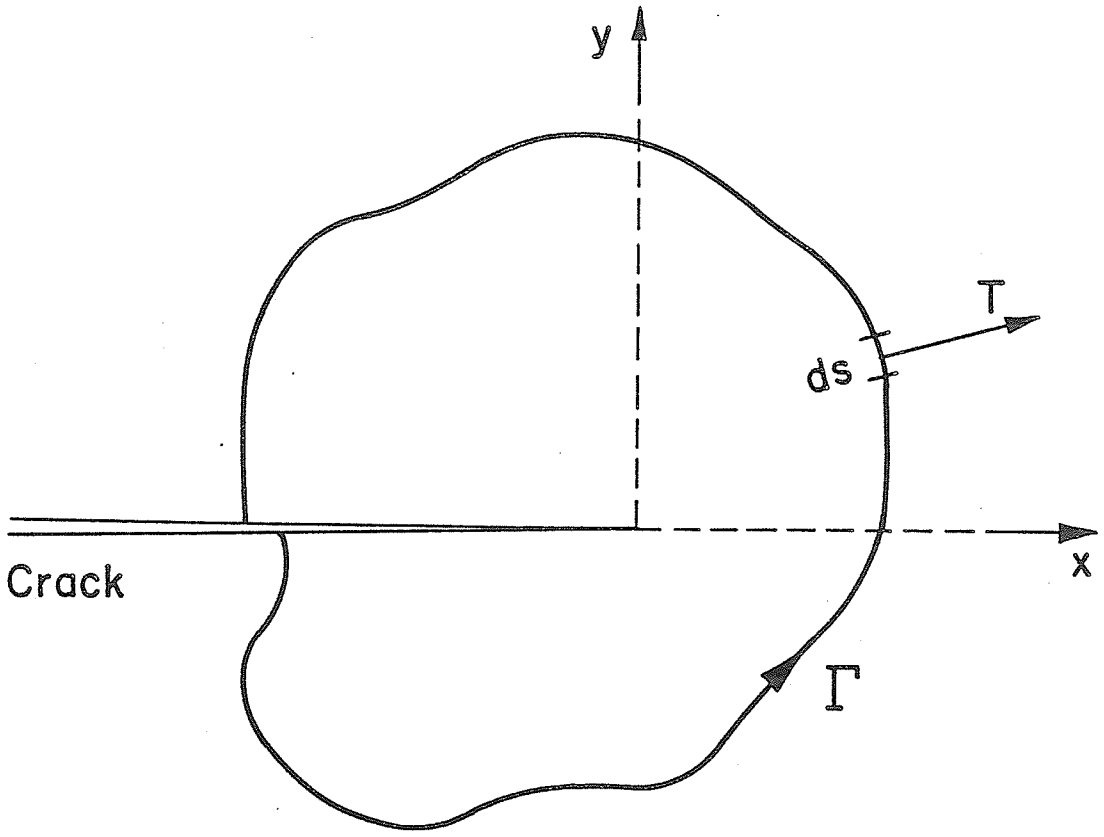

Fig. 2.4 J-Integral.

where w is the strain energy density function,

T_i is the surface traction vector ($= \sigma_{ij}\, n_j$),

u_i is the displacement vector and

ds is a differential element of an arc length along Γ.

The J-integral, derived under the assumption of non-linear elastic material behavior, is defined as the elastic energy release rate (per unit crack extension) to the crack tip. Since Rice [9] proved J to be path independent, one may evaluate J remote from the crack tip, where a well defined elastic field prevails, and use this value of J to represent the energy release rate to the crack tip, that is, paths adjacent to or remote from the crack tip produce the same result. This scheme is suitable in the case of small scale yielding, for which the concept of path independence of energy release rate to the crack tip is assumed to remain valid.

Just as K was found to describe the elastic crack tip stress field in the LEFM approach, Hutchinson [10] and Rice and Rosengren [11] showed that the stress-strain field at the crack tip may be expressed as

$$\sigma_{ij} = \left(\frac{J}{r}\right)^{\frac{1}{n+1}} f_{ij}\,(\theta,n) + \ldots$$

$$\varepsilon_{ij} = \left(\frac{J}{r}\right)^{\frac{n}{n+1}} g_{ij}\,(\theta,n) + \ldots \qquad (2.13)$$

where r and θ are polar coordinates centered at the crack tip and n is the power hardening coefficient in the assumed uniaxial stress-strain law, which is of the form $\varepsilon \propto \sigma^n$. For the linearly elastic case, n=1, equation (2.13) reduces to LEFM equations with $J = K^2/E_o$.

Just as the plastic zone size governs the validity of LEFM, so the size of the intensely non-linear zone restricts the application of J-integral approach. According to Paris [12], if the analysis using J is to be relevant, the size of this zone, I, must satisfy

$$I = 2 \frac{J}{\sigma_{ys}} \ll \text{planar dimensions.} \qquad (2.14)$$

Further, if plane strain behavior is to be maintained, the thickness B must satisfy

$$B \geq 25 \frac{J}{\sigma_{ys}} \quad . \qquad (2.15)$$

This restriction is an order of magnitude less severe than the corresponding LEFM requirement in equation (2.3).

2.3.4 Crack Growth Resistance R-Curve

The COD and J-integral methods described previously relate their values at crack initiation to K_{IC} under plane

strain conditions. These values may not be applied to determine the fracture toughness under plane stress conditions. The plane stress fracture toughness K_C, is generally 2-10 times larger than K_{IC} and varies with specimen thickness.

Representation of the fracture toughness of thin sheet materials by a resistance curve has been attempted by a number of scientists [13-16], and is still under development. The concept of the crack growth resistance R-curve is based on the observation that during the fracture process of most sheet materials, the unstable fracture is always preceded by a certain amount of stable crack growth under a monotonically rising load.

Fig. 2.5 illustrates a typical R-curve with the crack length as the abscissa and the crack growth resistance as the ordinate. The curve labeled K_R is the R-curve, determined from experiment, with the stress intensity factor K_R at any crack length a being that required to propagate the crack from length a_0 to a. The first stage of the R-curve is a vertical line representing a 'no crack growth' situation. The point where the R-curve deviates from a vertical line is the initiation of 'stable crack growth'. As the crack extends, the crack growth resistance also increases. This increased crack growth resistance is due to the increased size of the plastic zone and work hardened material ahead of the crack tip, which increases the amount of work required

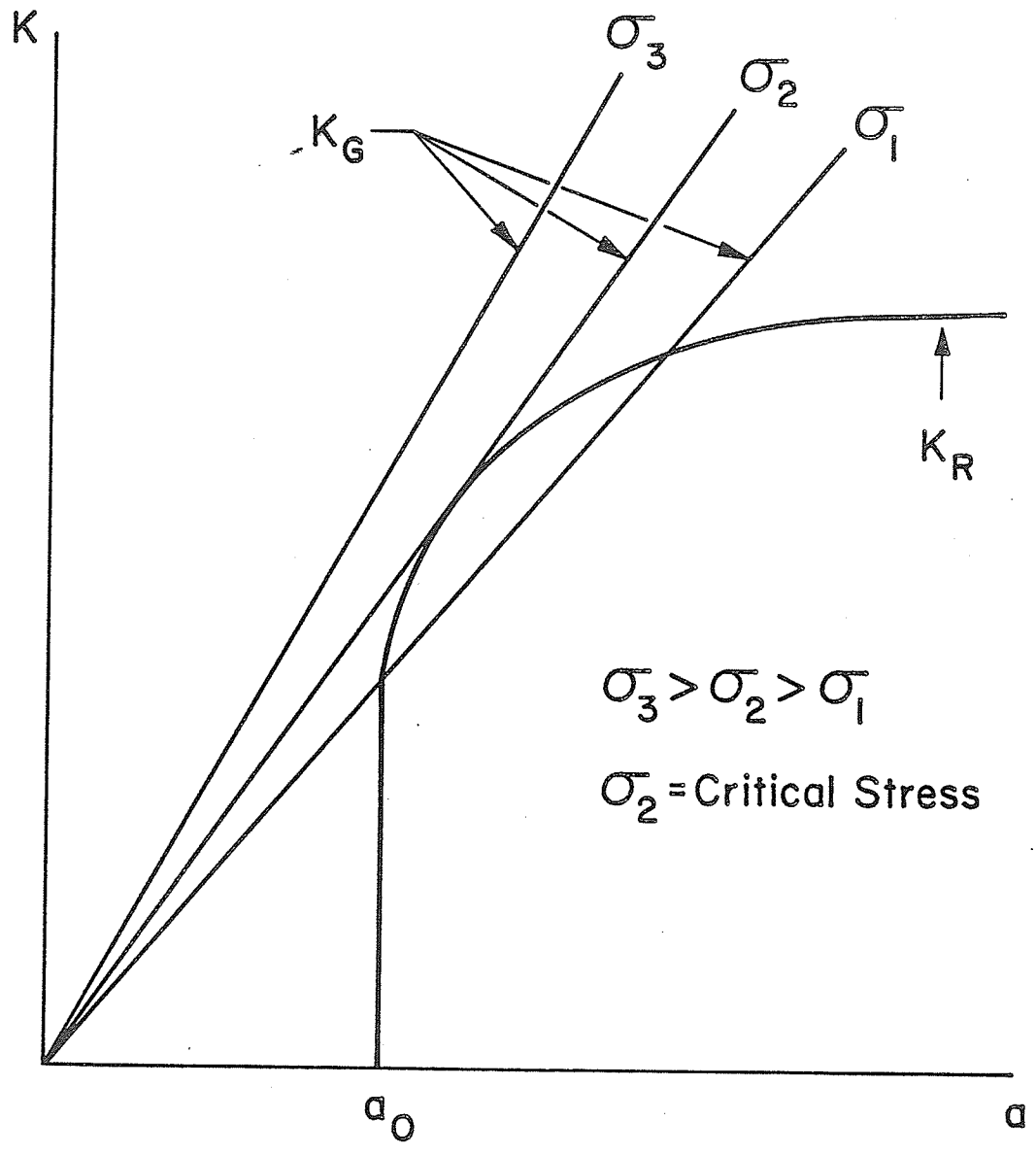

Fig. 2.5 R-Curve.

to move the crack tip. Finally, a stage is reached on the R-curve where no increased crack growth resistance accompanies crack growth, where the effects of increased crack length and decreased ligament size overcome the effect of work hardening ahead of the crack tip.

The fracture criterion in the R-curve concept is that for a given initial crack length a_0, failure will occur when the stress intensity factor from the applied loading, known as the crack driving force K_G, equals K_R. Note that this condition must be fulfilled at the same instantaneous crack length a. Thus a family of K_G curves is drawn at various applied stress levels σ_1, σ_2 etc. The K_G curve that fulfills the fracture criterion is tangent to the K_R curve at the critical point. The stress corresponding to this K_G curve will be the critical failure stress for an initial crack length a_0. Instability occurs since at the point of tangency of K_G curve will always exceed tangency of K_R curve for further crack extension.

$$\frac{\partial K_G}{\partial a} \geq \frac{\partial K_R}{\partial a} \quad . \tag{2.16}$$

Analytical studies on stable crack growth [17, 18] have indicated that the strain field ahead of an extending crack is governed by a logarithmic singularity rather than the stronger inverse square root singularity as in the stationary

case. This weaker singularity is due to the extension of the crack into the zone where the material is less plastically deformed, thus preventing complete refocusing of the strain field at the tip of the extended crack. This reduction in strain concentrations accompanying the crack tips may be one of the main reasons for stable crack growth.

2.4 Application of the Finite Element Method to Fracture Mechanics

Due to mathematical complexities, only a few crack problems, encompassing simplified boundary conditions have been solved analytically. However, the finite element method has been widely employed to solve a large variety of fracture problems. This well known numerical technique is capable of performing an elastic or elastic-plastic stress analysis to any two-or three-dimensional crack problem. Stress intensity factors under complicated geometry and loading conditions have been obtained using the linear elastic finite element method. Stress analysis, the determination of fracture criteria and the prediction of fracture instability have been attempted using the elastic-plastic finite element method.

2.5.1 Computation of Stress Intensity Factors

Kobayashi et al [19] and Chan et al [20] were the first to use the finite element method to calculate the stress intensity factor. Once the numerical values of the nodal displacements and the element stresses near the crack tip are obtained, the K value can be calculated using equation (2.3) at several points. The K value at the crack tip is evaluated by extrapolating these values to the crack tip and by disregarding the first few points very close to the crack tip.

Watwood [21] calculated the K value by computing the strain energy release rate G. The total strain energy of the structure, calculated for a given crack length, may be lacking in accuracy for a certain finite element mesh. However, there is a cancellation of these errors when taking the difference in strain energy for two different crack lengths, so reasonable accuracy is obtained with a relatively coarse mesh.

A number of special singular elements (Wilson [22], Byskov [23], Hilton and Sih [24], Tracey [25]) have been presented to accommodate the singularity at the crack tip. These elements are the result of incorporating both the eigen-function expansions for the crack tip field conditions and the finite element method. The theoretical background

of this approach is based on the mathematical properties of the two numerical techniques employed, i.e. the asymptotic expansion becomes increasingly more accurate as one approaches the crack tip, while the finite element method is very accurate everywhere except near the crack tip.

Another class of special singular elements is the quarter point element, used in conjunction with the standard isoparametric element. The Jacobian transformation from physical to isoparametric coordinates will produce spatial derivatives (i.e. strains) which are singular at the crack tip, if nodal points along the sides of the element are positioned in a certain way. Henshell [26] and Barsoum [27, 28] perceived that by moving the middle nodal point of a quadratic isoparametric element to the quarter point closest to the crack tip, the strain singularity is achieved.

2.5.2 Elastic-Plastic Analysis of a Stationary Crack

Swedlow et al [29-31] and Marcal and King [32] pioneered the application of elastic-plastic finite element analysis to ductile crack problems. They analyzed edge- and center-cracked plate under plane stress and plane strain conditions, and reasonable agreement was obtained between the numerical and experimental results. Since then the numerical accuracy of these predictions has been improved

through the better description of elastic-plastic material behavior and improved computing capability.

Miyamoto et al [33] presented results for two- and three-dimensional analyses of cracked plates and also showed results for cyclic loading, although not accurate enough for useful application. A more accurate analysis has been performed by Larsson and Carlsson [34] by which crack tip plastic zones are assumed to respond only to an elastic outer field of the singular stress field.

Precise stress analyses at the crack tip have been attempted by Rice and his co-workers [35-39]. Solutions for small scale yielding of plane strain cases have been obtained for non-hardening material [35, 36] and also for hardening material [37]. These investigations have been further extended to the analysis of large crack tip geometry change by using the finite strain theory [38].

Wells [40] and Turner and Cheung [41] calculated the COD value by the finite element method and showed that the crack initiation may be characterized by the critical value of COD.

Sumpter and Turner [42], Parks [43] and Miyamoto and Kageyama [44] showed that the finite element method can be used to calculate the path-independent J-integral and the crack initiation can be characterized by the critical value of the J-integral.

2.5.3 Elastic-Plastic Analysis of a Growing Crack

Kobayashi et al [45] and Anderson [46] proposed a nodal force relaxation technique simulating crack growth in the finite element model. Hsu and Bertels [47] also proposed the breakable element concept which can model the crack growth. Since then the finite element method has been used to investigate stable crack growth behavior for plane stress [48-53] and plane strain [54-60] cases under monotonically increasing loading condition.

Sorensen [56, 59] investigated stable crack growth of anti-plane shear and plane strain cases under an arbitrary loading history. His results showed that while the stress distribution ahead of a growing crack was found to be nearly the same as that ahead of a stationary crack, the strain values were lower for a growing crack.

Shih et al [57] and Kanninen et al [58] investigated several fracture criteria characterizing stable crack growth by using the experimentally obtained applied load vs stable crack growth curve as input information. The fracture criteria examined in their studies include the J-integral, its rate of change during crack growth dJ/da, the crack tip opening angle (CTOA), the energy release rate G and the crack tip force F.

d'Escatha and Devaux [60] evaluated stable crack growth based on microscopic development, i.e. void nucleation, void growth and coalescence. The purpose of this model was to predict the fracture properties of a material during the process of crack initiation, stable crack growth and crack instability. Various parameters used to correlate stable crack growth were evaluated by this model, including CTOA, the J-integral and F.

Lee and Liebowitz [54] used the applied load vs crack growth curve as an input information, to produce a linear relationship between the plastic energy and crack growth.

Newman [61] performed finite element analyses using one of the fracture criteria to determine applied load vs crack growth behavior and instability for a given specimen geometry. He studied the effects of various parameters such as mesh size, strain hardening and critical strain on finite element fracture predictions for both monotonic and cyclic loading conditions. While some interesting observations were made, no attempts were made to correlate the predictions with actual material behaviour.

Varanasi [49] used ultimate tensile strength as a fracture criterion to predict the unstable crack growth. Belie and Reddy [53] used critical strain as a fracture criterion and adopted the 'zero modulus-unload reload' scheme

as a technique for crack growth modelling. Even though some comparisons were made between experimental results and numerical results in these two papers, the accuracy was very crude due to their unrealistic computational method.

The elastic-plastic finite element method was also used to investigate crack growth under cyclic loading conditions with simplified assumptions [61-63].

CHAPTER 3

FINITE ELEMENT FORMULATIONS FOR ELASTIC-PLASTIC STRESS ANALYSIS

3.1 Introduction

The finite element method is a versatile numerical technique for the determination of forces and displacements in a structure. This method offers generous flexibility for the incorporation of non-linear material behavior (plasticity) and changing boundary conditions (crack growth). Presented in this chapter are the finite element formulations for elastic-plastic stress analysis of planar type structures, which were subsequently used for the analysis of stable crack growth in ductile materials.

3.2 Basic Matrix Formulations

The basis of the method is in the division of the structure into a finite number of discrete parts (elements) which interconnect at their apexes (nodes) and form an idealized structure system as shown in Figure 3.1. The displacements at the nodes are normally chosen to be primary unknown quantities, while the displacements in the elements are commonly assumed to vary according to some simple polynomial functions, called shape or interpolation functions. The displacements are usually continuous across the element boundaries.

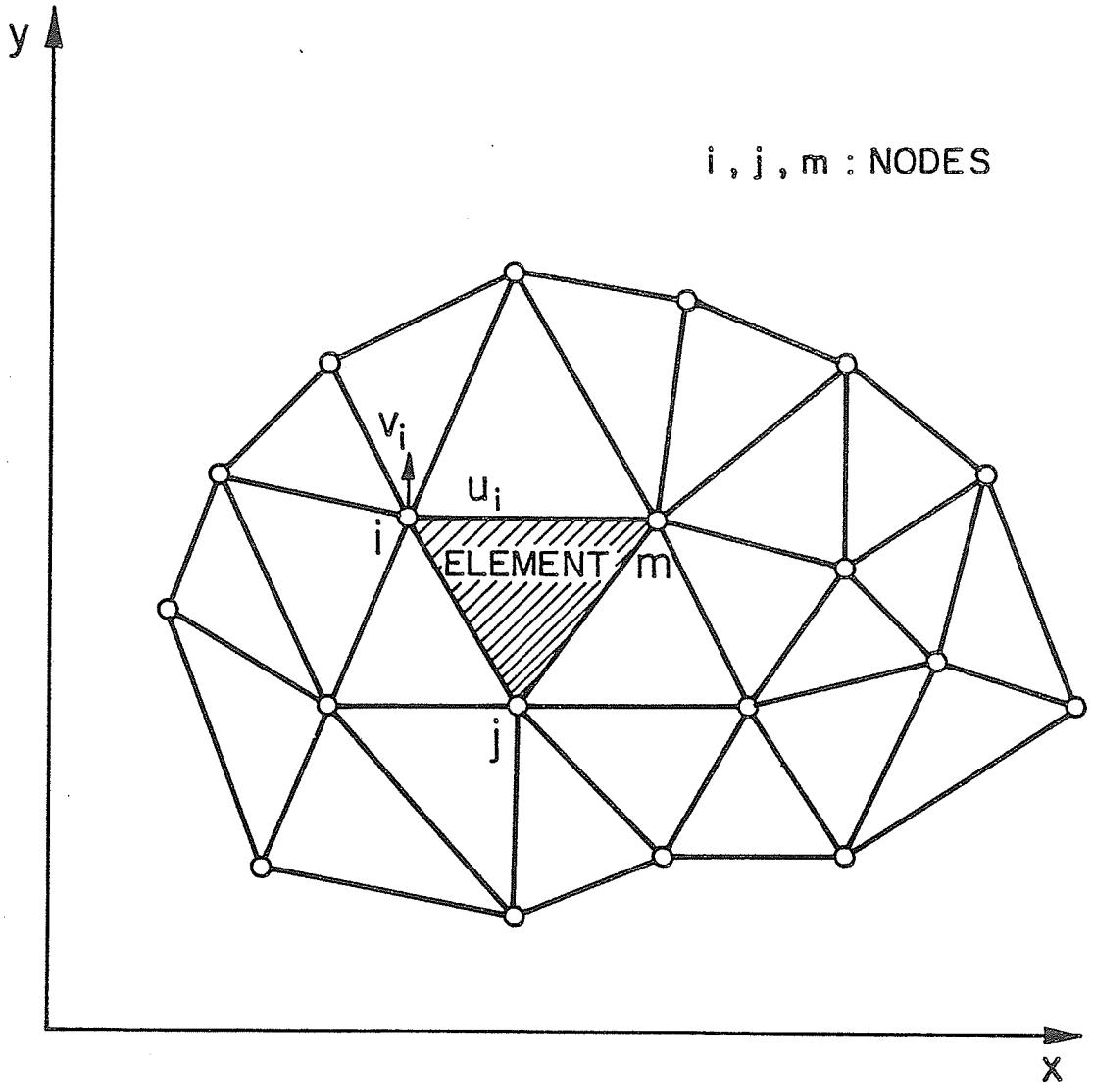

Fig. 3.1 Discretization of a Structure.

The governing matrix formulations for the finite element analysis have been well documented [64, 65] and are briefly reviewed below.

Element Interpolation Function:

$$\{u\} = [N]\{u\}^e \quad (3.1)$$ [+]

where $\{u\}$ is the displacement vector for any point within an element,

$[N]$ is the matrix containing the interpolation (or shape) function and

$\{u\}^e$ is the vector made up of the nodal displacements.

Strain-Displacement Relation:

$$\{\varepsilon\} = [B]\{u\} \quad (3.2)$$

where $\{\varepsilon\}$ is the strain vector and

$[B]$ is the strain-displacement transformation matrix containing spatial derivatives of the interpolation function.

Stress-Strain Relation:

$$\{\sigma\} = [C]\{\varepsilon\} \quad (3.3)$$

[+] A 'e' superscript denotes the element.

where $\{\sigma\}$ is the stress vector and

$[C]$ is the stress-strain constitutive matrix.

Element Stiffness:

$$[K]^e = \int_v [B]^T [C][B] \, dv \qquad (3.4)$$

where $[K]^e$ is the element stiffness matrix and

v denotes the volume of the element.

Global Stiffness:

$$[K]\{u\}^e = \{Q\} \qquad (3.5)$$

where $[K]$ is the global stiffness matrix and

$\{Q\}$ is the global vector of applied nodal forces.

The global stiffness matrix $[K]$ is formed as an assemblage of the stiffness matrices of each individual element in the finite element mesh. Equation (3.5) can be used to solve for the unknown displacements $\{u\}^e$ after applying appropriate boundary conditions. Strain and stress components for each element are then subsequently calculated using equations (3.2) and (3.3).

+A 'T' superscript denotes the transpose of a matrix.

3.3 Elastic-Plastic Analysis

A number of finite element computer codes based on elastic-plastic stress analysis have been reported in the literature [66-72]. Among them, two major approaches are commonly used, namely the initial stress/strain and the incremental strain methods. The latter approach is adopted in this analysis since it is more practical to use for the analysis of crack growth. This method is essentially a step-wise linear incremental analysis to simulate the non-linear elastic-plastic material behavior. The derivations presented here are based on the works of Ueda [66], Yamada et al [67], Hsu et al [71] and Wu [72].

If the existence of incremental stationarity of the potential energy in a system of finite elements at a linearly approximated stress-strain state is postulated, the incremental stiffness equation of the structure is obtained as:

$$[K]_{\ell} \{\Delta u\}_{\ell} = \{\Delta Q\}_{\ell} \tag{3.6}$$

where $[K]_{\ell}$ is the variable stiffness matrix,

$\{\Delta u\}_{\ell}$ is the incremental displacement vector and

$\{\Delta Q\}_{\ell}$ is the incremental global load vector for the loading step ℓ.

The variable stiffness matrix $[K]_{\ell}$ in equation (3.6) may be updated after each load increment to account for the change in the stress-strain relations of equation (3.3) due to the elastic-plastic effects. For the elastic situation the procedure is simply a step-wise summation of the incremental elastic strains, $\{\delta\varepsilon^e\}$, with the stiffness matrix unchanged. When the stress level of one or more of the elements of a structure exceeds the yield strength of the material, these elements are said to have deformed plastically. Such plastic material behavior can be accounted for by the formulation of $[K]^e$ in equation (3.4). In addition to the elastic components, the total strain at this step should also include the plastic component $\{\delta\varepsilon^p\}$:

$$\{\delta\varepsilon\} = \{\delta\varepsilon^e\} + \{\delta\varepsilon^p\} \ . \qquad (3.7)$$

To complete the elastic-plastic stress analysis, it is necessary to have:

(1) A yield criterion to ascertain the state of stress at which initial yielding is considered to begin.

(2) A flow rule relating the plastic strain increments to the stresses and stress increments.

(3) A hardening rule to establish conditions for subsequent yielding from a plastic state.

Because of the complexity associated with plastic deformation, no universally applicable laws characterizing the material behavior in the plastic range have yet been developed. Thus any attempt to predict analytically the behavior of structures in the plastic range must begin with a choice among the several available plasticity theories of one which successfully combines mathematical simplicity with a reasonably faithful representation of experimentally observed material behavior.

3.3.1 Von Mises Yield Criterion

The Von Mises yield criterion is considered to be the most practical and reliable of the numerous yield criteria. It is based on the theory that yielding of a material is initiated when the distortion energy of the material reaches a certain critical value. This is equivalent to a combination of the principal stresses reaching a critical value, so as to form a locus called the yield surface. For an isotropic material, the yield surface is defined by:

$$F = J_2 - \tau_{ys}^2 = J_2 - \frac{1}{3}\sigma_{ys}^2 \qquad (3.8)$$

in which J_2 = second deviatoric stress invariant

$$= \frac{1}{2}\sigma'_{ij}\,\sigma'_{ij}$$

σ'_{ij} = deviatoric stress components

$= \sigma_{ij} - \sigma_{kk}\delta_{ij}$

δ_{ij} = Kronecker delta = $\begin{cases} 0 & (i \neq j) \\ 1 & (i = j) \end{cases}$

and τ_{ys}, σ_{ys} are the experimentally determined yield stresses in pure shear and in uniaxial tension respectively.

This criterion further implies that if the state of stress is such that $F < 0$ then the material is in the elastic region, i.e. $\{\delta\varepsilon^p\} = 0$, while if $F = 0$ a plastic state has been attained and plastic behavior must be taken into account.

3.3.2 Prandtl-Reuss Flow Rule

The incremental Prandtl-Reuss flow rule assumes that the incremental plastic strain components are a function of the current stress state, the strain increments, and work hardening parameter k, which is a function of the plastic deformation:

$$\{d\varepsilon^p\} = \{d\varepsilon^p\}\ (\{\sigma\},\ \{d\varepsilon\},\ k)\ . \qquad (3.9)$$

Now, equation (3.7) can be written in the incremental form:

$$\{d\varepsilon\} = \{d\varepsilon^e\} + \{d\varepsilon^p\} \tag{3.10}$$

in which from incremental form of equation (3.3)

$$\{d\varepsilon^e\} = [C^e]^{-1} \{d\sigma\} \quad . \tag{3.11}$$

From equations (3.10) and (3.11), it can be shown that:

$$\{d\sigma\} = [C^e] (\{d\varepsilon\} - \{d\varepsilon^p\}) \tag{3.12}$$

which may be rewritten as

$$\{d\sigma\} = [C^{ep}] \{d\varepsilon\} \tag{3.13}$$

where $[C^{ep}]$ is called the elastic-plastic matrix and is expressed as

$$[C^{ep}] = [C^e] - [C^p] \tag{3.14}$$

in which $[C^e]$ is the elastic matrix and

$[C^p]$ is the plastic matrix.

Equation (3.14) indicates that the plastic deformation reduces the strength of the material by reducing the magnitudes of the parameters in the $[C^e]$ matrix.

To derive the $[C^{ep}]$ matrix, it is necessary to obtain both the slope (H') of the tangent to the effective stress - effective plastic strain ($\bar{\sigma}$ - $\bar{\varepsilon}^p$) curve, and the flow rule

description of the differential changes in the plastic strain component $\{d\varepsilon^p\}$ as expressed in equation (3.9). It is apparent from Fig. 3.2 that

$$H' d\bar{\varepsilon}^p = d\bar{\sigma} \tag{3.15}$$

in which effective stress $\bar{\sigma}$ and effective plastic strain increment $d\bar{\varepsilon}^p$ are defined as:

$$\bar{\sigma} = \left(\frac{3}{2}\, \sigma'_{ij}\ \sigma'_{ij}\right)^{\frac{1}{2}}$$

$$= \frac{1}{\sqrt{2}} \left[(\sigma_{xx} - \sigma_{yy})^2 + \sigma_{xx}^2 + \sigma_{yy}^2 + 6\, \sigma_{xy}^2\right]^{\frac{1}{2}} \tag{3.16}$$

$$d\bar{\varepsilon}^p = \left(\frac{2}{3}\, d\varepsilon^p_{ij}\ d\varepsilon^p_{ij}\right)^{\frac{1}{2}}$$

$$= \frac{\sqrt{2}}{3} \left[(d\varepsilon^p_{xx} - d\varepsilon^p_{yy})^2 + (d\varepsilon^p_{yy} - d\varepsilon^p_{zz})^2\right.$$

$$\left. + (d\varepsilon^p_{zz} - d\varepsilon^p_{xx})^2 + 6\, d\varepsilon^{p\,2}_{xy}\right]^{\frac{1}{2}} \tag{3.17}$$

The Prandtl-Reuss flow rule representation with isotropic hardening states that the plastic strain component increments are proportional to the deviatoric stress components (σ') [67], or:

$$\{d\varepsilon^p\} = \{\sigma'\}\ d\lambda \tag{3.18}$$

where $d\lambda$ is a proportionality factor.

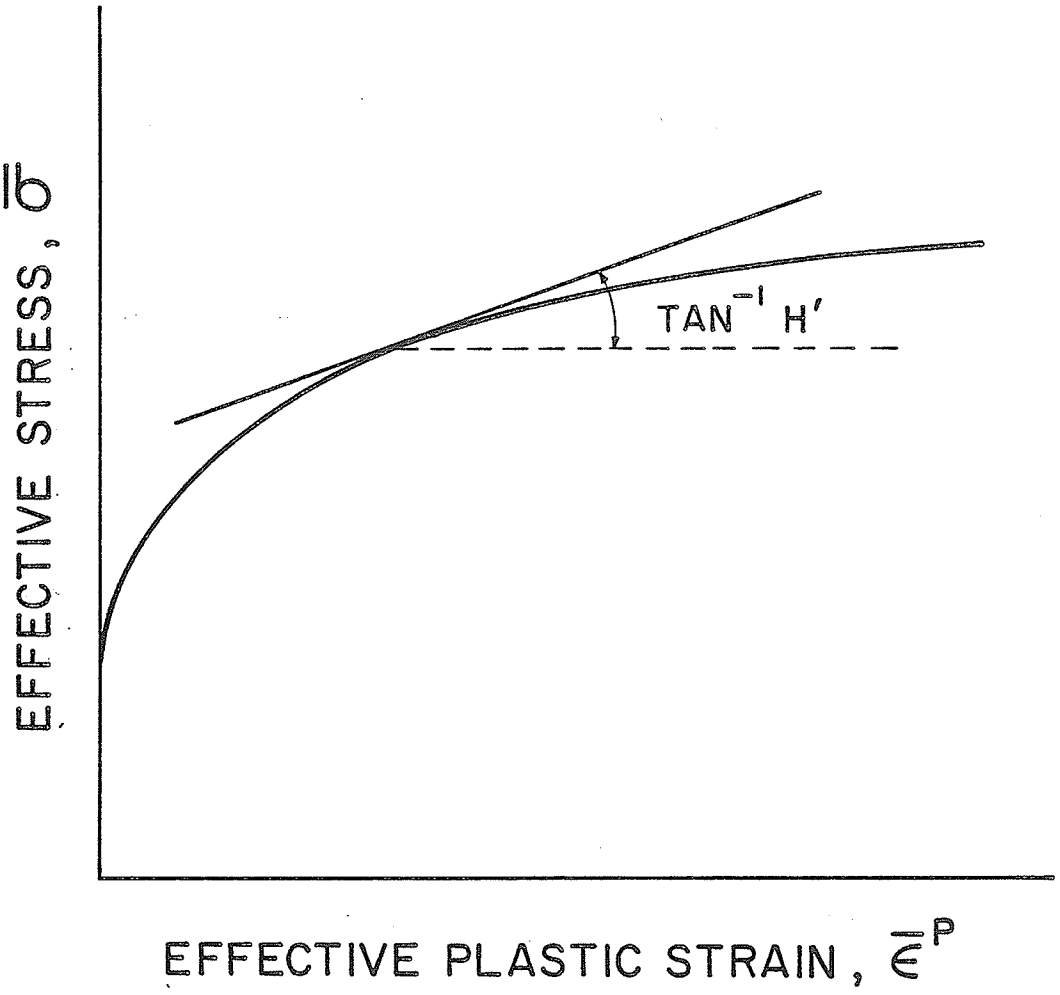

Fig. 3.2 Effective Stress-Effective Plastic Strain Curve.

3.3.3 Isotropic Hardening Rule.

The general yielding criterion which takes only the current stress state $\{\sigma\}$ and hardening parameter k into account, is

$$F(\{\sigma\}, k) = 0 \tag{3.19}$$

and its differential form is:

$$dF = \left\{\frac{\partial F}{\partial \sigma}\right\}^T \{d\sigma\} + \frac{\partial F}{\partial k}\, dk \tag{3.20}$$

Equation (3.20) can be expressed as follows when the plastic strains are introduced:

$$dF = \left\{\frac{\partial F}{\partial \sigma}\right\}^T \{d\sigma\} + \frac{\partial F}{\partial k} \left\{\frac{\partial k}{\partial \varepsilon^p}\right\} \{d\varepsilon^p\} \quad . \tag{3.21}$$

Substituting equations (3.12) and (3.18) into equation (3.22), one obtains:

$$\left\{\frac{\partial F}{\partial \sigma}\right\}^T [C^e] (\{d\varepsilon\} - \{\sigma'\}\, d\lambda) + \frac{\partial F}{\partial k} \left\{\frac{\partial k}{\partial \varepsilon^p}\right\} \{\sigma'\}\, d\lambda = 0 \quad . \tag{3.22}$$

Solving for $d\lambda$ using equation (3.22), the following equation is obtained:

$$d\lambda = \frac{\{\frac{\partial F}{\partial \sigma}\}^T [C^e] \{d\varepsilon\}}{\{\frac{\partial F}{\partial \sigma}\}^T [C^e] \{\sigma'\} - \frac{\partial F}{\partial k} \{\frac{\partial k}{\partial \varepsilon^p}\}^T \{\sigma'\}} \quad . \tag{3.23}$$

Substituting equation (3.23) into equation (3.18), one obtains:

$$\{d\varepsilon^p\} = \{\sigma'\} d\lambda$$

$$= \frac{\{\sigma'\} \{\frac{\partial F}{\partial \sigma}\}^T [C^e]}{S} \{d\varepsilon\} \tag{3.24}$$

where

$$S = \{\frac{\partial F}{\partial \sigma}\}^T [C^e] \{\sigma'\} - \frac{\partial F}{\partial k} \{\frac{\partial k}{\partial \varepsilon^p}\}^T \{\sigma'\} \quad . \tag{3.25}$$

Comparison between equations (3.12), (3.14) and equation (3.24) yields:

$$[C^p] = \frac{[C^e] \{\sigma'\} \{\frac{\partial F}{\partial \sigma}\}^T [C^e]}{S} \quad . \tag{3.26}$$

The elastic-plastic matrix $[C^{ep}]$ can be expressed as:

$$[C^{ep}] = [C^e] - [C^p]$$

$$= [C^e] - \frac{[C^e] \{\sigma'\} \{\frac{\partial F}{\partial \sigma}\} [C^e]}{S} \quad . \tag{3.27}$$

It is also shown [67] that:

$$\left\{\frac{\partial F}{\partial \sigma}\right\} = \frac{3}{2\bar{\sigma}} < \sigma'_{11},\ \sigma'_{22},\ 2\sigma'_{12} >^T$$

$$\frac{\partial F}{\partial k} = -\frac{2}{3} H' \qquad (3.28)$$

$$\left\{\frac{\partial k}{\partial \varepsilon^p}\right\} = \{\sigma\}^T \ .$$

The elasticity matrix $[C^e]$ for plane stress case takes the form:

$$[C^e] = \frac{E}{1-\nu^2} \begin{bmatrix} 1 & \nu & 0 \\ & 1 & 0 \\ \text{sym.} & & \frac{1-\nu}{2} \end{bmatrix} \ . \qquad (3.29)$$

Thus

$$[C^e] \left\{\frac{\partial F}{\partial \sigma}\right\}^T = \frac{3E}{2\bar{\sigma}(1-\nu^2)} \begin{Bmatrix} \sigma'_{11} + \nu\sigma'_{22} \\ \nu\sigma'_{11} + \sigma'_{22} \\ (1-\nu)\,\sigma'_{12} \end{Bmatrix} \ . \qquad (3.30)$$

and

$$[C^e] \left\{\frac{\partial F}{\partial \sigma}\right\}^T \left\{\frac{\partial F}{\partial \sigma}\right\} [C^e]$$

$$= \frac{9E^2}{4\bar{\sigma}^2(1-\nu^2)^2} \begin{bmatrix} (\sigma'_{11}+\nu\sigma'_{22})^2 & (\sigma'_{11}+\nu\sigma'_{22})(\nu\sigma'_{11}+\sigma'_{22}) & (1-\nu)\sigma'_{12}(\sigma'_{11}+\nu\sigma'_{22}) \\ & (\nu\sigma'_{11}+\sigma'_{22})^2 & (1-\nu)\sigma'_{12}(\nu\sigma'_{11}+\sigma'_{22}) \\ & & (1-\nu)^2\sigma'^2_{12} \end{bmatrix}$$

(3.31)

Let

$$S_1 = \frac{E}{(1 - \nu^2)} \left(\sigma'_{11} + \nu\sigma'_{22}\right)$$

$$S_2 = \frac{E}{(1 - \nu^2)} \left(\nu\, \sigma'_{11} + \sigma'_{22}\right) \tag{3.32}$$

$$S_3 = \frac{E}{1 + \nu}\, \sigma'_{12} \quad .$$

Equation (3.31) may be expressed as:

$$[C^e] \left\{\frac{\partial F}{\partial \sigma}\right\}^T \left\{\frac{\partial F}{\partial \sigma}\right\} [C^e] = \frac{9}{4\bar{\sigma}^2} \begin{bmatrix} S_1^2 & S_1S_2 & S_1S_3 \\ & S_2^2 & S_2S_3 \\ \text{sym.} & & S_3^2 \end{bmatrix} \tag{3.33}$$

and

$$\left\{\frac{\partial F}{\partial \sigma}\right\}^T [C^e] \left\{\frac{\partial F}{\partial \sigma}\right\} = \frac{9}{4\bar{\sigma}^2} \left[\sigma'_{11}S_1 + \sigma'_{22}S_2 + 2\sigma'_{12}S_3\right] . \tag{3.34}$$

Substituting equations (3.29), (3.33) and (3.34) into equation (3.27), it can be derived that:

$$[C^{ep}] = \frac{E}{1 - \nu^2} \begin{bmatrix} 1 & \nu & 0 \\ & 1 & 0 \\ \text{sym.} & & \frac{1 - \nu}{2} \end{bmatrix} - \begin{bmatrix} \frac{S_1^2}{S_0} & \frac{S_1S_2}{S_0} & \frac{S_1S_3}{S_0} \\ & \frac{S_2}{S_0} & \frac{S_2S_3}{S_0} \\ \text{sym.} & & \frac{S_3^2}{S_0} \end{bmatrix} \tag{3.35}$$

with

$$S_0 = \frac{4}{9}\bar{\sigma}^2 H' + (S_1 \sigma'_{11} + S_2 \sigma'_{22} + 2S_3 \sigma'_{12}) \qquad (3.36)$$

in which S_1, S_2 and S_3 were defined in equation (3.32).

3.4 Material Constitutive Relation

In the present analysis, experimentally determined elastic-plastic constitutive relations of $\bar{\sigma}$ and $\bar{\varepsilon}$ are approximated by a generalized family of continuous functions [71, 73]:

$$\bar{\sigma} = \frac{\bar{E}\bar{\varepsilon}}{\left\{1 + \left[\frac{\bar{E}\bar{\varepsilon}}{(1 - \frac{\bar{E}'}{\bar{E}})\,\bar{\sigma}_K + \bar{E}'\bar{\varepsilon}}\right]^n\right\}^{1/n}} \qquad (3.37)$$

in which $\bar{E} = \frac{3E}{2(1+\nu)}$ and

$$\bar{E}' = \frac{3E'}{[3 - \frac{(1-2\nu)E'}{E}]}$$

where $E' = \lim_{\varepsilon \to \infty} E$,

$\bar{\sigma}_K$ is auxiliary stress close to the elastic-plastic transition (as shown in Fig. 3.3) and

n is a factor which determines the abruptness of the transition.

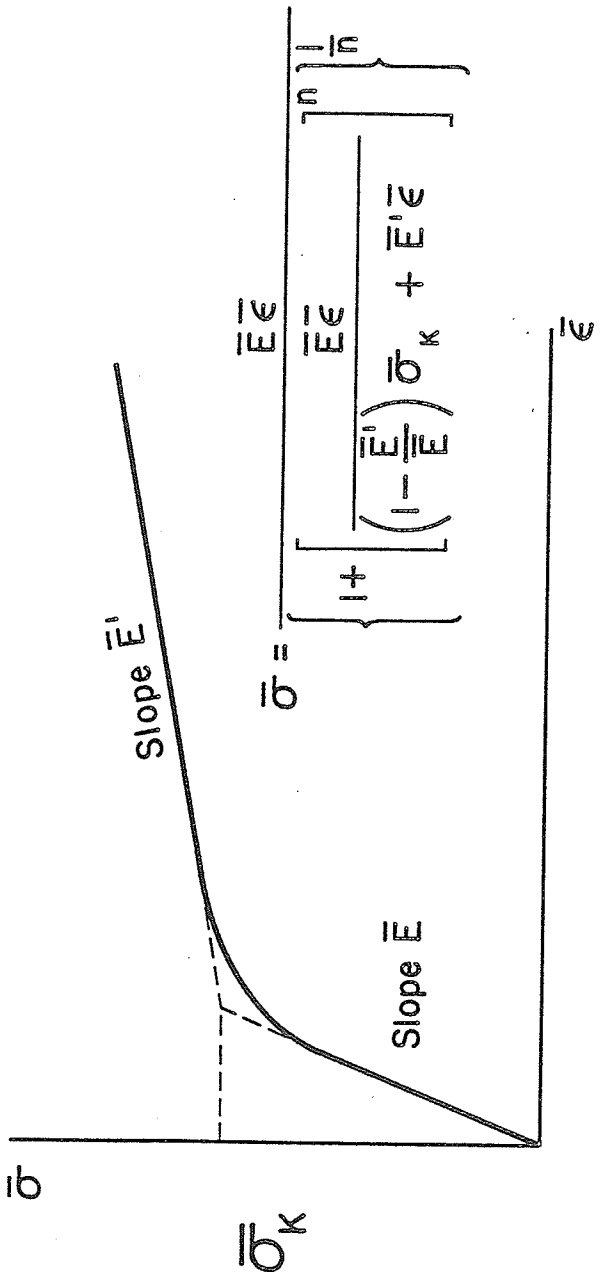

Fig. 3.3 Polynomial Approximation of Stress-Strain Relations.

The value H', which was defined in equation (3.13) as

$$H' = \frac{d\bar{\sigma}}{d\bar{\varepsilon}^p}$$

may be approximated by

$$H' = \frac{1}{\partial\bar{\varepsilon}^p/\partial\bar{\sigma}}$$

$$\doteq \frac{1}{\frac{\partial\bar{\varepsilon}}{\partial\bar{\sigma}} - \frac{\partial\bar{\varepsilon}^e}{\partial\bar{\sigma}}}$$

$$\doteq \frac{1}{\frac{1}{E_t} - \frac{1}{\bar{E}}} \quad . \tag{3.38}$$

From equation (3.37), E_t can be calculated by the following relation:

$$E_t = \frac{d\bar{\sigma}}{d\bar{\varepsilon}} = \frac{\bar{E}\left\{1 + \left[\frac{\bar{E}\bar{\varepsilon}}{(1 - \frac{\bar{E}'}{\bar{E}})\,\bar{\sigma}_K + \bar{E}'\bar{\varepsilon}}\right]^{n+1} \frac{\bar{E}'}{\bar{E}}\right\}}{\left\{1 + \left[\frac{\bar{E}\bar{\varepsilon}}{(1 - \frac{\bar{E}'}{\bar{E}})\,\bar{\sigma}_K + \bar{E}'\bar{\varepsilon}}\right]^{n}\right\}^{\frac{n+1}{n}}} \tag{3.39}$$

CHAPTER 4

NUMERICAL MODELLING OF STABLE CRACK GROWTH

4.1 Introduction

Stable crack growth preceding fracture instability in ductile materials may occur when the plastic zone size at the crack tip is large as compared to the thickness of the material. The problem is of particular theoretical interest since the plastic zone behind the extending crack tip is unloaded to an elastic state, while that portion of the plastic zone ahead of the crack tip expands. The variation of the crack tip parameters during this crack extension process yields useful information which may lead to a fracture criterion in the presence of large scale yielding.

In order to accomplish this, proper implementation of the fracture criterion and the crack growth simulation algorithm is necessary. This chapter describes the proposed numerical technique that simulates stable crack growth in the finite element model.

4.2 Fracture Criterion

The continuum equations governing the stress-strain field near a growing crack tip may not be expected to account for the microstructural phenomenon of separation inherent in the fracture process. The same is true in the finite element modelling of a growing crack tip, but for this analysis the difficulty is usually obviated through the use of a fracture criterion based on some macroscopic field quantity. Extensive research to this point has identified nine possible requirements [57] which must be fulfilled by a candidate fracture criterion. However, an acceptable fracture criterion still remains open to discussion.

Schaeffer et al [74], Gavigan et al [75] and Evans et al [76] attempted to measure the strain field around the crack tip. Their results indicated that the strains at a small distance away from the crack tip are independent of geometry and, to a lesser extent, of material. As a consequence of this it is postulated that a rupture surface exists as an extension of the von Mises yield surface [77]. Fracture is assumed to occur when the state of strain at the crack tip has reached the rupture surface; the corresponding value of the effective strain is used as a fracture criterion. This value is calculated by numerically

modelling a stable crack growth experiment. The effective strain corresponding to the maximum applied load with no crack extension is designated as the effective rupture strain, $\bar{\varepsilon}_{rup.}$.

4.3 The 'Breakable Element'

The 'breakable element' concept is based on the successive reduction of the stiffness matrix of the crack tip element during the simulated crack growth. One stiffness reduction scheme that has been used in the past to treat crack propagation in concrete structures [78] consisted of setting Young's modulus to zero. Another procedure [79] used a zero Young's modulus for the crack tip element to achieve the singularity present in elastic crack analysis.

In 1976, Hsu and Bertels [47] proposed the stiffness reduction scheme to model crack growth, referred to as the 'breakable element'. However, in their case study breakable elements were skipped during crack growth. After a similar attempt to model crack growth by a simple reduction of the stiffness matrix [80], the author found that the computational accuracy can be further improved by creating a pseudo nodal point in the breakable element used in the stiffness reduction scheme. This pseudo nodal point moves through the

breakable element as the crack tip extends, producing smoother crack growth.

In this analysis breakable elements are positioned along the expected crack path (Fig. 4.1(a)). The following steps are then employed to simulate crack growth in the finite element model at any given load step.

Step 1: Upon completion of the stress analysis at any load step, the effective strains in the breakable elements are extrapolated as a smooth curve toward the crack tip using a least squares curve fitting technique [81]. The best numerical results were obtained by extrapolating the average effective strains at the centroids of the first four elements immediately in front of the crack tip. The distribution of the effective strain ahead of the crack tip can be expressed as:

$$\bar{\varepsilon}(x) = a_1 x^3 + a_2 x^2 + a_3 x + a_4 \qquad (4.1)$$

where x denotes the distance from the crack tip along the crack path and

a_1, a_2, a_3 and a_4 are constants derived from the least squares analysis of the average strains at the element centroids (x_1, x_2, x_3, x_4).

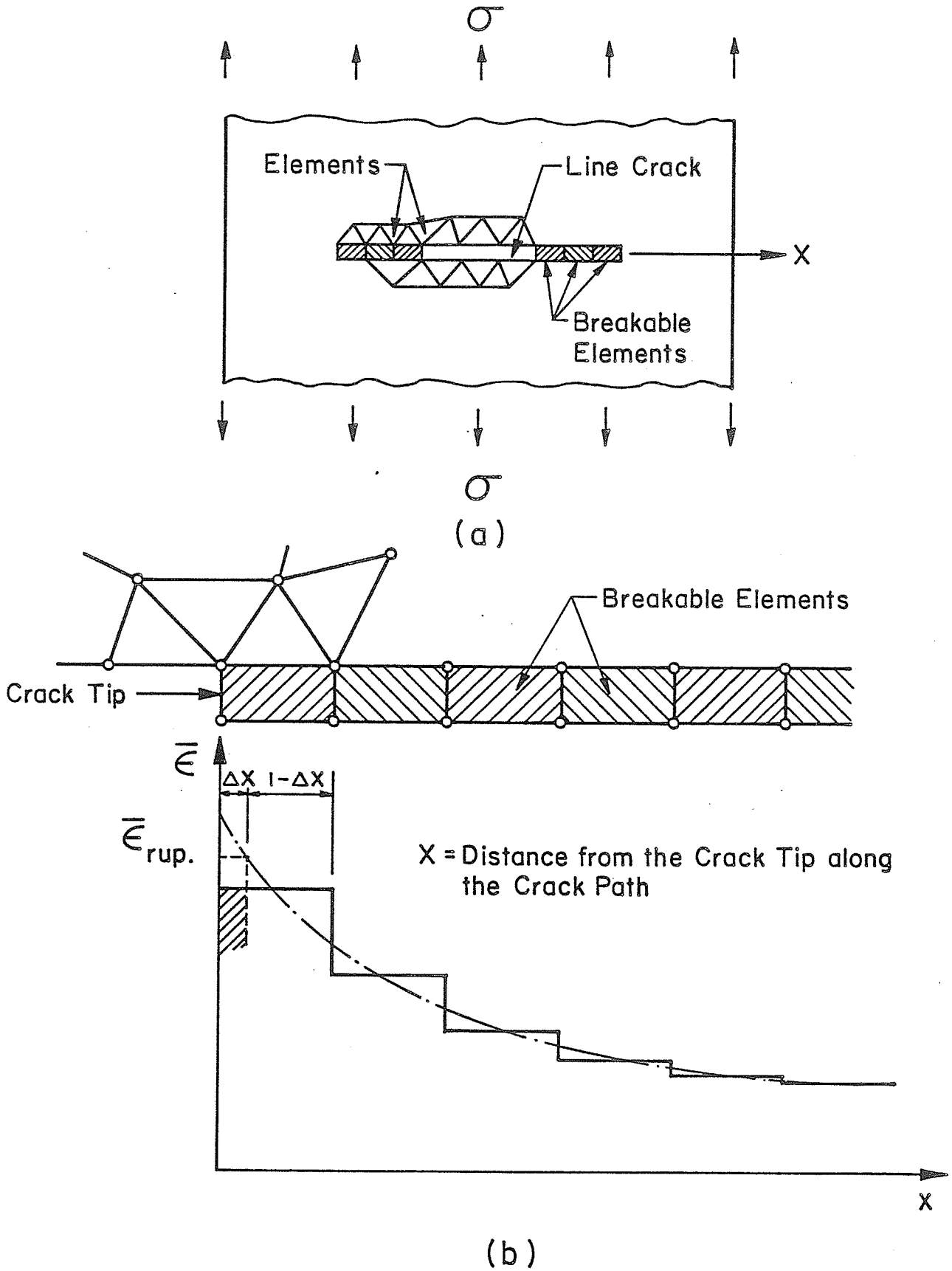

Fig. 4.1 Numerical Modelling of Crack Growth
(a) Geometry and Breakable Elements
(b) Step i

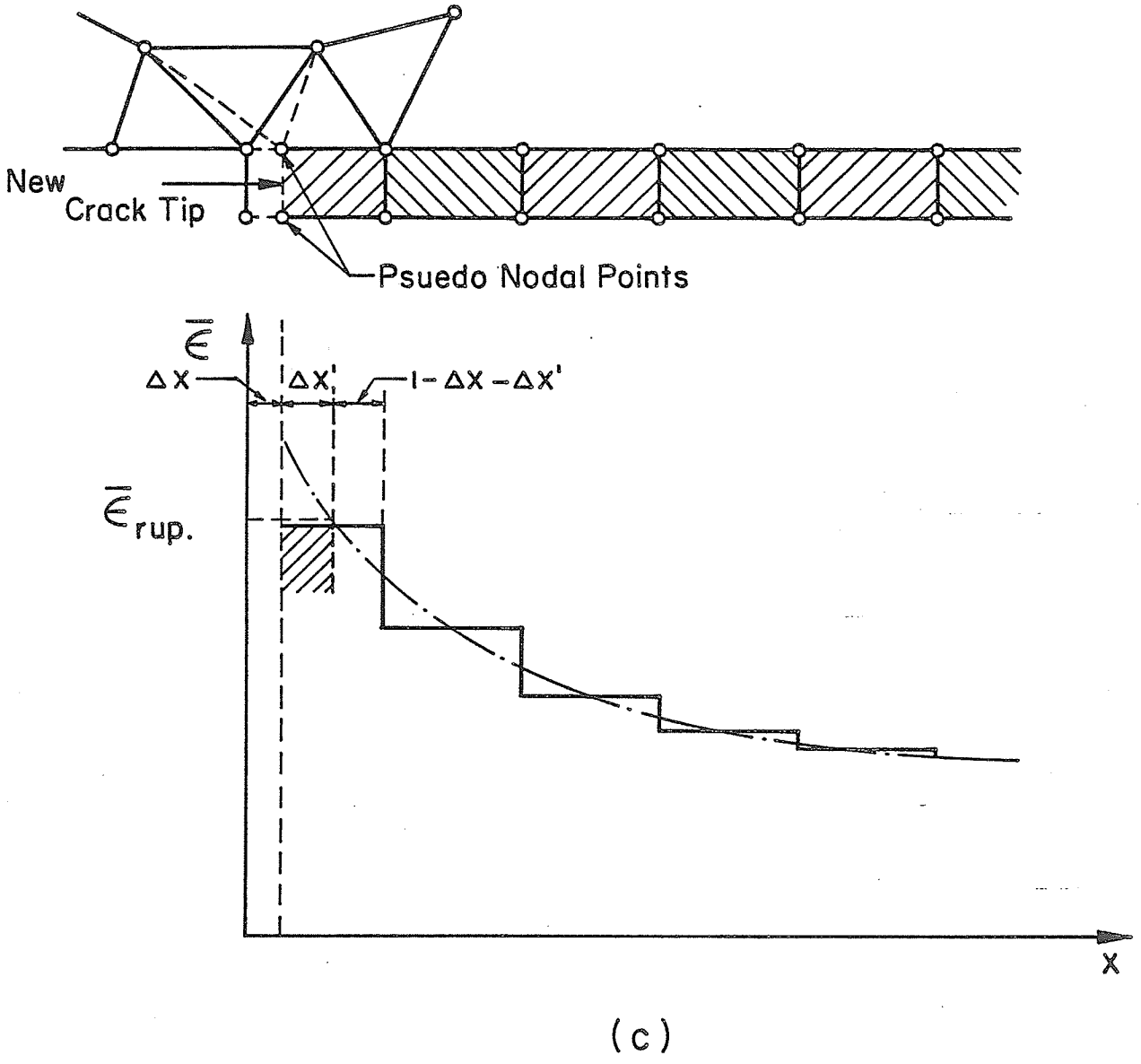

Fig. 4.1 Numerical Modelling of Crack Growth
(c) Step i+1

If the extrapolated strain at the crack tip, $\bar{\varepsilon}_{ext.}$ ($\bar{\varepsilon}(0.0)$), does not exceed the assigned fracture criterion, $\bar{\varepsilon}_{rup.}$, then the stress analysis proceeds with the application of the next load increment.

Step 2: If $\bar{\varepsilon}_{ext.}$ exceeds $\bar{\varepsilon}_{rup.}$, the crack growth process begins. Fig. 4.1(b) illustrates schematically the start of crack growth at load step i. The strains in the proportional length Δx of the breakable element adjacent to the crack tip (crack tip element) are estimated to have exceeded $\bar{\varepsilon}_{rup.}$. Thus the portion Δx of the element is deemed to have fractured and become incapable of carrying any load. The amount of crack extension, Δx, is evaluated by solving for the value of x in equation (4.1) at which $\bar{\varepsilon}(x) = \bar{\varepsilon}_{rup.}$.

Step 3: For the next load step i+1, the $[K]^e$ matrix of the crack tip element is evaluated with a proportionately reduced volume. The original nodal points at the crack tip are shifted by the amount Δx to the positions of the pseudo nodal points, which specify the current location of the crack tip. This nodal point shift changes the [B] matrix, which in turn reduces the $[K]^e$ matrix in equation (3.4) as:

$$[K']^e = \int_{V'} [B']^T [C] [B'] \, dv' \qquad (4.2)$$

where $[K']^e$ is the reduced $[K]^e$ matrix,

$[B']$ is the $[B]$ matrix after the nodal point shift and

v' is the reduced volume of the crack tip element.

Obviously the nodal point shift in the $[B]$ matrix results in larger strain and stress increments in equations (3.2) and (3.3) respectively.

At this load step an additional portion, $\Delta x'$, may be found to exceed $\bar{\varepsilon}_{rup.}$. This is dealt with similarly as outlined in step 2.

Step 4: The shifting to the new pseudo nodal points at each load step continues so long as $\bar{\varepsilon}_{ext.}$ exceeds $\bar{\varepsilon}_{rup.}$. When the aspect ratio of the remaining ligament of the crack tip element reaches a critical value, the pseudo nodal points are considered to have reached the next nodal points, thereby maintaining numerical stability. In this manner, the whole element is gradually broken and simultaneously its stiffness progressively reduced to and then maintained as a zero stiffness element.

4.4 Nodal Force Relaxation

Once the crack front has passed through a crack tip element, a nodal force relaxation procedure is implemented

in order to redistribute the stress field previously supported by the crack tip element before the element breaks. The following algorithm was developed for this purpose.

Step 1: The nodal reaction force of the 'broken' crack tip element (say element No. 1 in Fig. 4.2) is calculated from the accumulated stress before the element breaks:

$$\{F\} = \int_V [B]^T \{\sigma\} \, dv \quad . \tag{4.3}$$

Step 2: Since relaxation occurs in the direction normal to the crack growth path, only the loading direction components of the reaction forces at nodes 18 and 19 as illustrated in Fig. 4.2 are applied over five[+] equal incremental loading steps. A stress analysis on the whole structure is performed with these nodal reaction forces, while the external load remains constant. The increments of displacements and stresses so derived are added to the accumulated displacements and stresses of the structure.

[+]It was found that increasing the number of loading steps beyond five provided only a minimal improvement in the results for a significant increase in the computational expense.

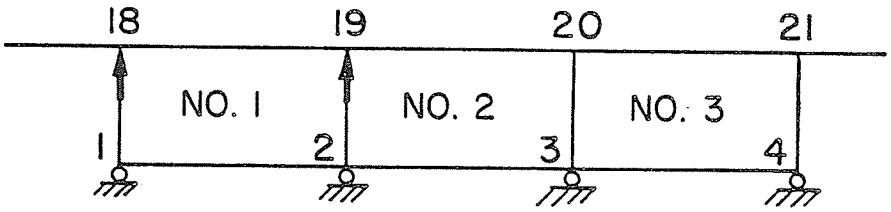

Fig. 4.2 Application of Nodal Reaction Force.

Step 3: The amount of crack extension due to the nodal force relaxation is determined after the fifth relaxation step using the extrapolation scheme outlined in the previous section. If the extended crack tip exceeds the next nodal point (i.e. node 3 in Fig. 4.2), continuous nodal force relaxation of the subsequent element (i.e. element No. 2 in Fig. 4.2) must also be carried out. Otherwise, a further load increment is necessary in order to increase the strain distribution ahead of the crack tip.

In step 2, the stress analysis for the entire structure requires routines which change the element stiffness according to the incremental theory of plasticity, since the relaxation technique results in simultaneously unloading of the newly created crack surface behind and loading of the region ahead of the crack tip. Thus the $[K]^e$ matrix is calculated using the $[C^e]$ and $[C^{ep}]$ matrices for the unloading and loading elements respectively.

The determination of element loading or unloading is done iteratively using a trial application of Step 2. Initially all elements are assumed to continue loading. Equation (3.6) is solved and the incremental stresses due to the trial load step are added in the usual manner. For each element the effective stress ($\bar{\sigma}_2$) for the trial load step is

compared with the effective stress ($\bar{\sigma}_1$) prior to the application of the trial step. The loading and unloading elements are determined for $\bar{\sigma}_2 \geq \bar{\sigma}_1$ and $\bar{\sigma}_2 < \bar{\sigma}_1$ respectively (Fig. 4.3). The stress state prior to the trial step is then re-established and the crack is extended as outlined above with the loading and unloading elements now identified.

4.5 Computer Code 'TEPSCA'

A finite element computer code TEPSA [71] (Thermal Elasto-Plastic Stress Analysis), has been employed in this investigation for the numerical modelling of stable crack growth. The TEPSA code was originally developed to model the thermomechanical behavior of CANDU nuclear fuel elements (axisymmetric analysis), and features linear displacement triangular and quadrilateral simplex elements. A plane stress version following the formulations in Chapter 3 was implemented and verified by the author with a number of case studies. In general the numerical results from the TEPSA plane stress version were in excellent agreement with both analytical solutions and results from other computer codes. The crack growth modelling scheme as described in this chapter was subsequently implemented to form a new version, TEPSCA.

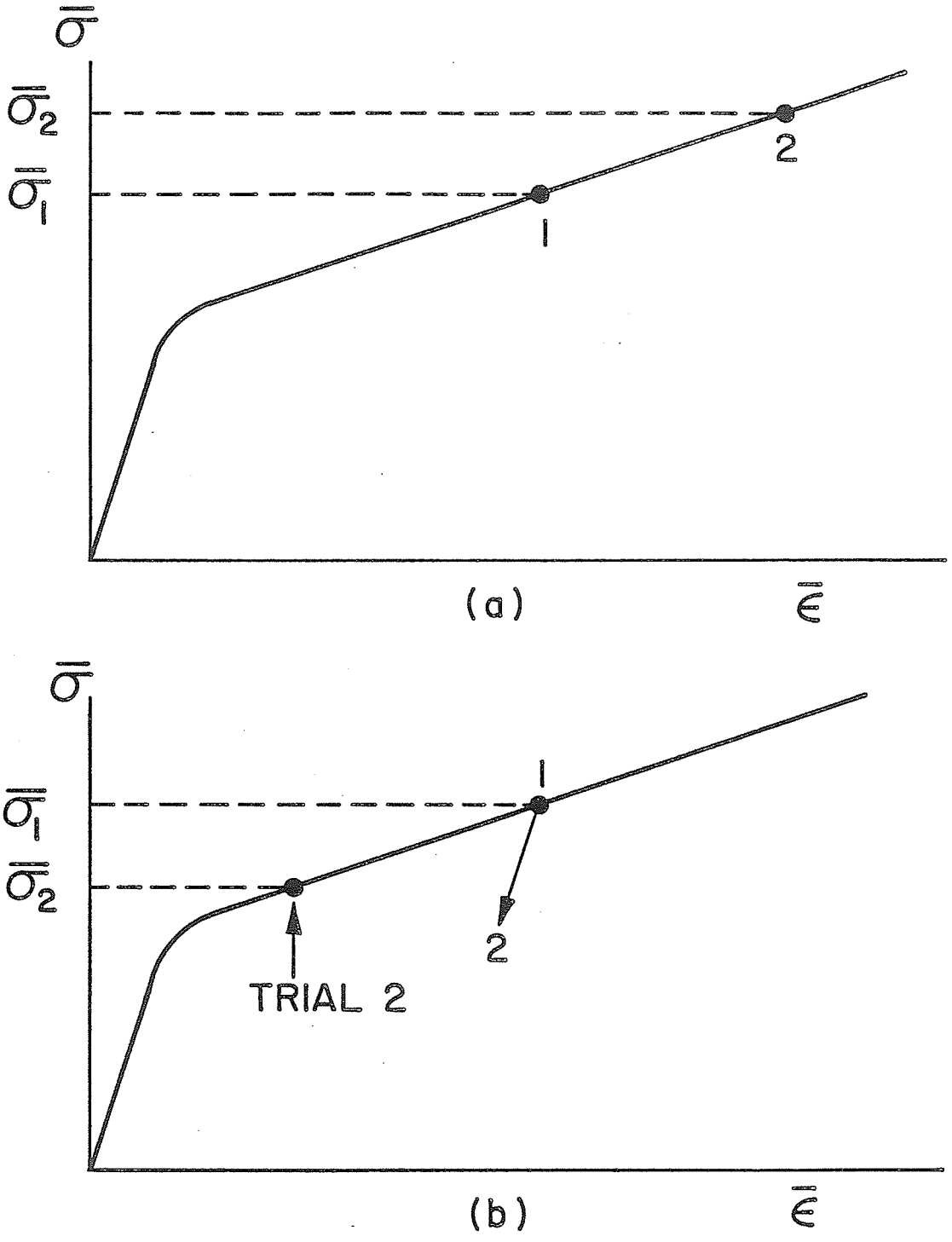

4.3 Determination of Loading or Unloading in an Element.
(a) Loading (b) Unloading

CHAPTER 5

EXPERIMENTAL TESTING PROGRAM

5.1 Introduction

This chapter describes the experimental testing program, the objective of which was to obtain the applied stress vs stable crack growth curves for center-cracked aluminum sheets subjected to a monotonically increasing load. The experiments were conducted under both mode I and mixed mode loading conditions. In addition to observing the crack growth behavior, strains were measured at various locations on the specimens over the course of the tests.

5.2 Experimental Program

5.2.1 Test Specimens

The specimens were machined from 0.064 in. (1.6 mm) thick 2024-T3 alclad aluminum sheet. This ductile alloy exhibits very little anisotropy in sheet form. The nominal chemical composition and mechanical properties are given respectively in Tables 5.1 and 5.2.

Two types of specimens were employed, namely those for the mode I and mixed mode (45° inclined crack)

Table 5.1

Chemical Composition of 2024-T3 Alclad Aluminum Alloy

Cu	4.5%
Mg	1.5%
Mn	0.6%

Table 5.2

Mechanical Properties of 2024-T3 Alclad Aluminum Alloy

Yield Strength	45 ksi (312 MPa)
Ultimate Tensile Strength	65 ksi (450 MPa)
% Elongation	18%
Modulus of Elasticity	10.6×10^6 psi (7.3×10^4 MPa)

specimens. Details of the shape and dimensions of each specimen are presented in Fig. 5.1. The specimens were oriented such that the rolling direction was aligned parallel to the loading direction. As well, they were prepared in batches to minimize the effects of the preparation procedure of individual specimens on the experimental results.

A 1/4 in. (6.35 mm) diameter hole was drilled through the center of each specimen. From the hole, two symmetric cuts, each 0.012 in. (0.305 mm) wide and up to 5.4 in. (13.72 cm) long were made. In an attempt to simulate more accurately a crack in the specimen, the end of each saw cut was then lengthened and tapered using a flat sharp jeweller's file, leaving the overall length of each cut at 6 in. (15.24 cm). It has been demonstrated that there is little difference in the fracture reistances of a fatigue crack tip and that of a 0.001 in. (0.0254mm) radius crack tip [14]. Accordingly, a razor blade was subsequently used to produce a 0.001 in. (0.0254 mm) radius at the tip of the simulated crack.

5.2.2 Test Equipment

All of the tests were carried out in the Metallurgical Science Laboratory of the Department of Mechanical Engineering,

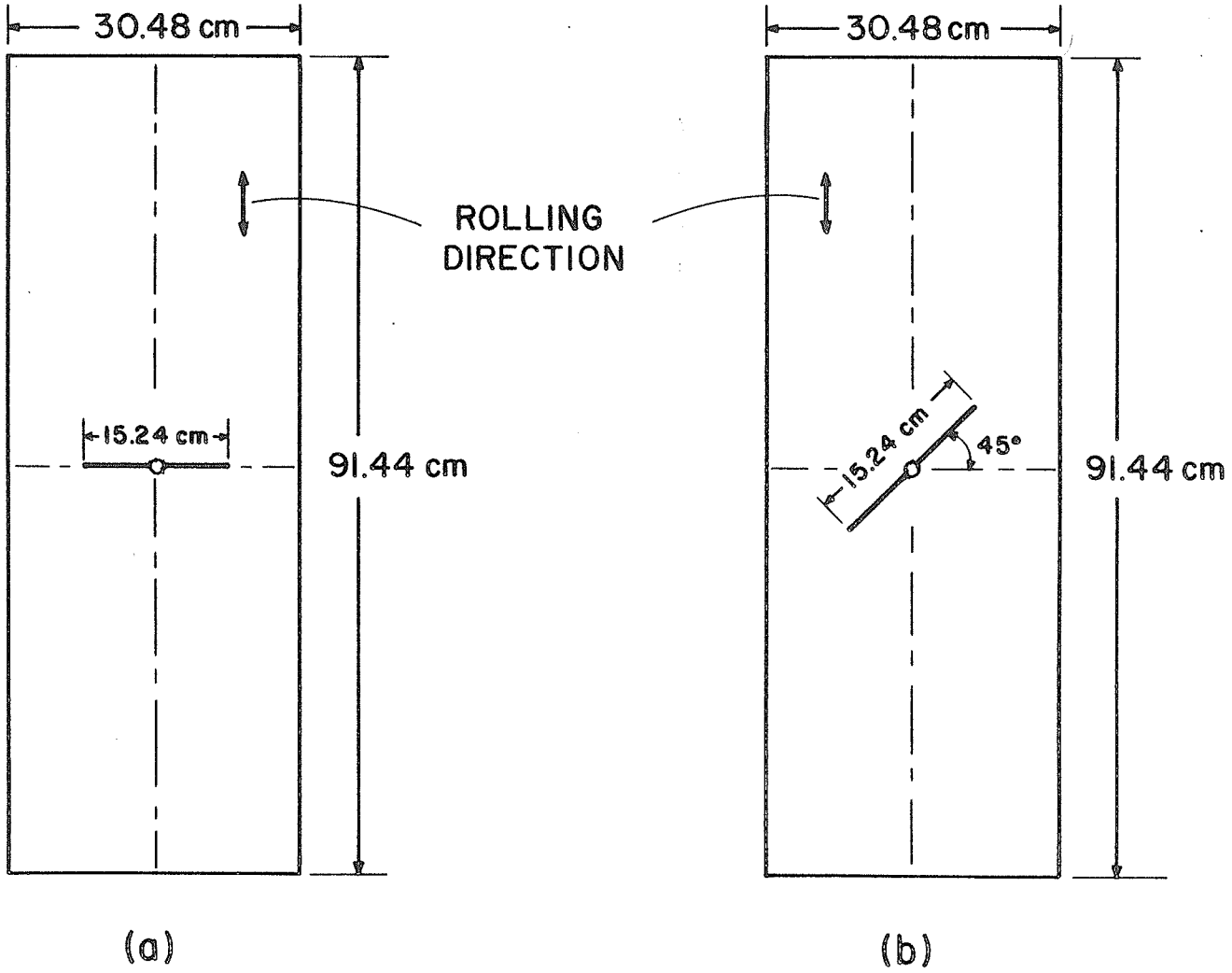

FIGURE 5.1

SHAPE AND DIMENSIONS OF SPECIMENS
(a) MODE I (b) MIXED MODE (45° INCLINED)

The University of Manitoba, using an Instron servohydraulic material testing system (Model 1332). This apparatus is capable of applying axial loads to a static rating of ± 55 kips (244.64 KN) and a fatigue rating of ± 27.5 kips (122.32 KN), under load control, strain control or stroke control, in a variety of waveforms at frequencies up to 1,000 Hz.

Each end of the specimen was clamped in a jointed grip, which was fabricated according to the ASTM R-curve recommendations [82] and reference [83]. In order to maintain loading symmetry, each grip consisted of two stiff jaws joined to a fork-like mounting bolt at the machine end. Each end of the specimen was fixed in the grips by using 24 bolts tightened to 100 ft-lbs of torque, ensuring adequate grip/specimen clamping.

Buckling of the central portion of the specimen had been observed during preliminary testing. To avoid this problem, rigid face plates were affixed adjacent to the central portion of the specimen. Lubrication was also provided between the face plates and the specimen. The initial clamping force between opposing face plates was only a few pounds, insufficient to alter the test results significantly.

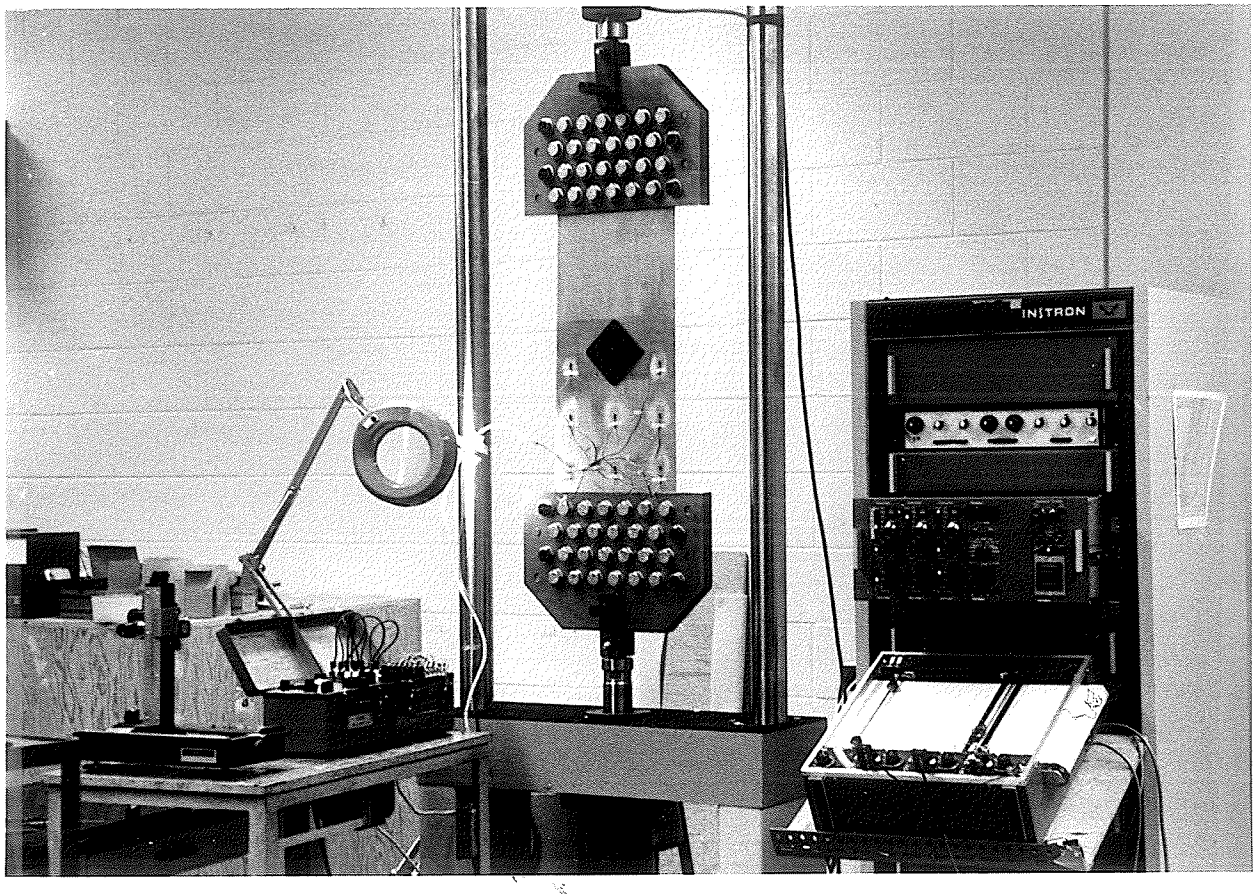

Fig. 5.2 Experimental System.
(a) Instron Fatigue Testing System.

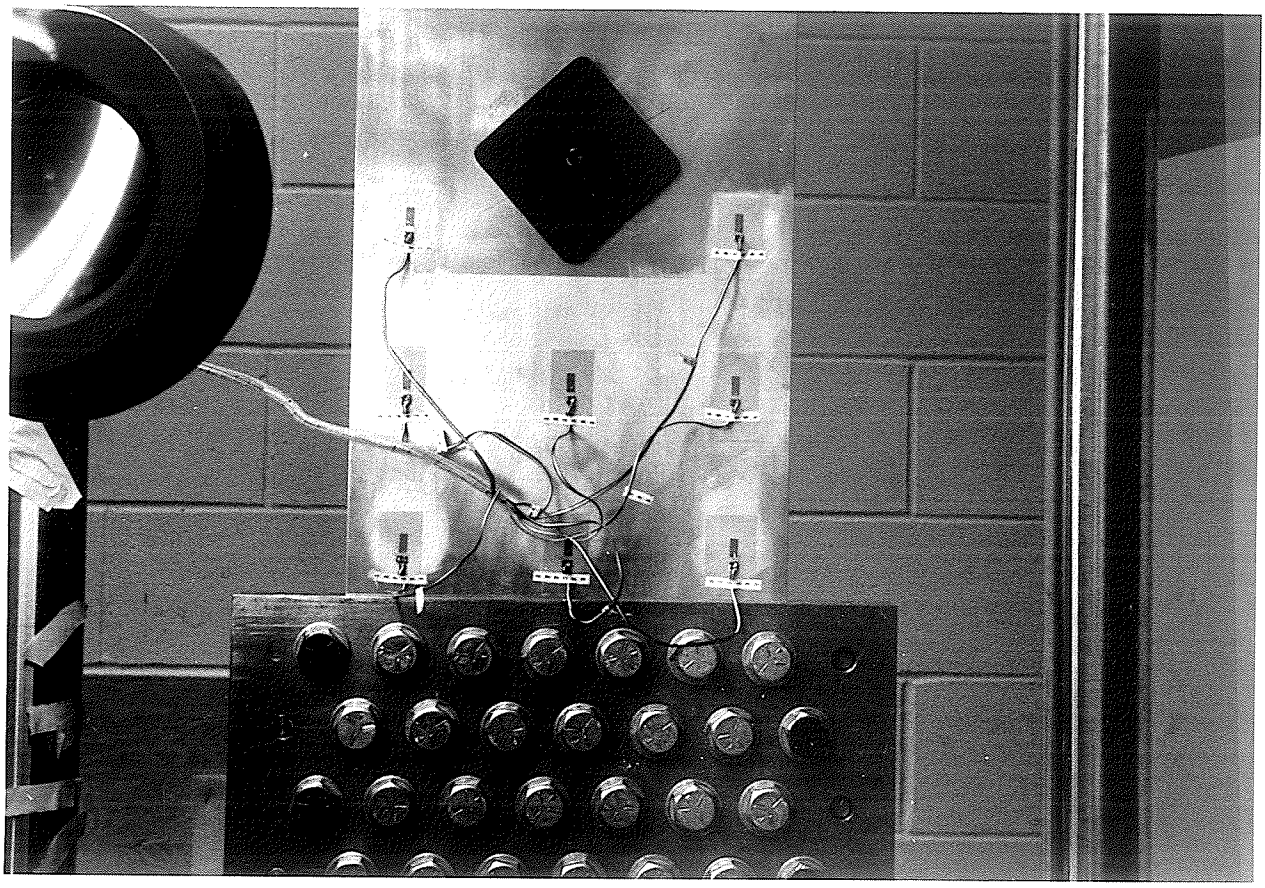

Fig. 5.2 Experimental System.
(b) Clamping System.

A set-up of the testing machine loaded with a specimen is presented in Fig. 5.2(a). A closer view of the clamping system is shown in Fig. 5.2(b).

5.2.3 Test Procedure

The tests were performed under load controlled conditions, with the load increasing monotonically from zero until the fracture of the specimen. A series of crack length measurements were taken over the course of each test. The machine was halted at various load levels and the crack length was measured using an X-Y vernier microscope with a magnification of 30x. Measurements were taken only after sufficient time had elapsed for the crack to stabilize. Although most cracks stabilized within seconds of halting at a particular load, near the instability condition several minutes were allowed for the position of the crack tip to stabilize.

A constant cross-head speed was maintained throughout all the tests, while the load-displacement curve was recorded on a Riken Denshi X-Y plotter (Model D-72 BP).

Strain values were obtained from electrical resistance strain gauges attached at eight locations to the specimen (Fig. 5.3) for both a mode I and a mixed mode test run. The strain gauges used were precision strain gauges of type

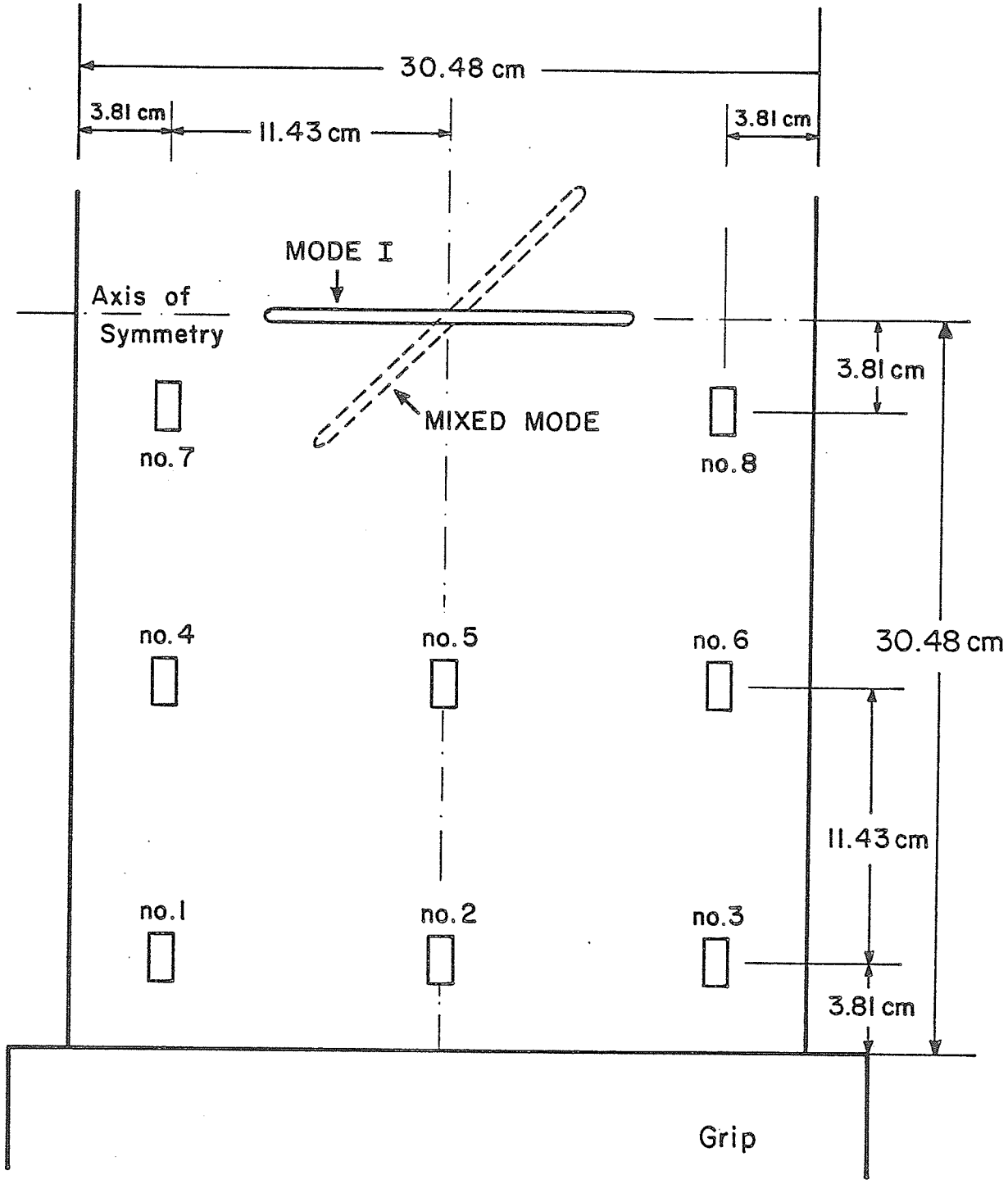

Fig. 5.3 Strain Gauge Locations.

CEA-13-250UW-350, manufactured by Micro-Measurements (M-M). They were 0.25 in. (6.35 mm) long, with a strain limit of 5%.

5.3 Experimental Results

5.3.1 Crack Developments

As it was difficult to photograph the crack profile through the microscope during the test, plastic tape was used to replicate the crack path using the following procedure.

A small amount of acetone was first used to soften the tape before it was attached to the specimen surface. The tape was removed when dry, carrying with it a replica of the crack path. To improve the reflection and contrast of the replica, powdered chromium was sprayed onto the tape surface. A photograph of this tape was then taken through a microscope.

Fig. 5.4(a) is a photograph showing a replica of the crack profile while Fig. 5.4(b) presents a closer view of the bent crack region for a mixed mode specimen.

Fig. 5.5 shows a photograph of a section from a fractured mode I specimen. As expected, the crack path was perpendicular to the loading plane. It was also

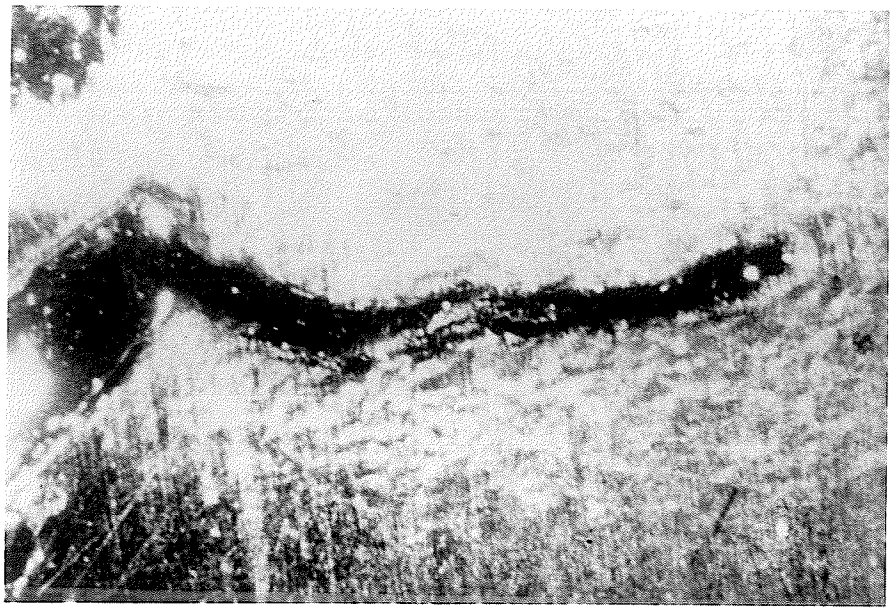

(a)

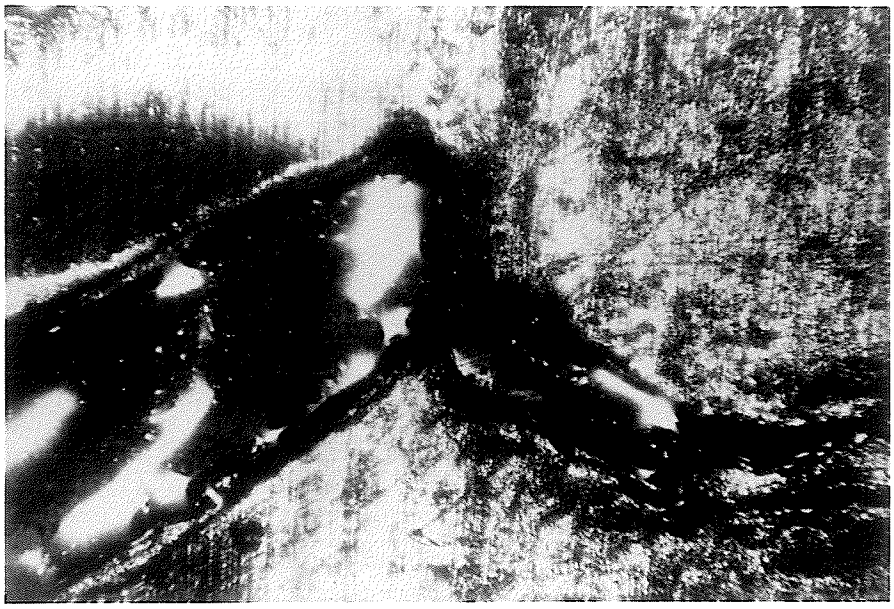

(b)

Fig. 5.4 Replica of the Crack Profile for the Mixed Mode Specimen.
(a) Overall view (b) Bent region

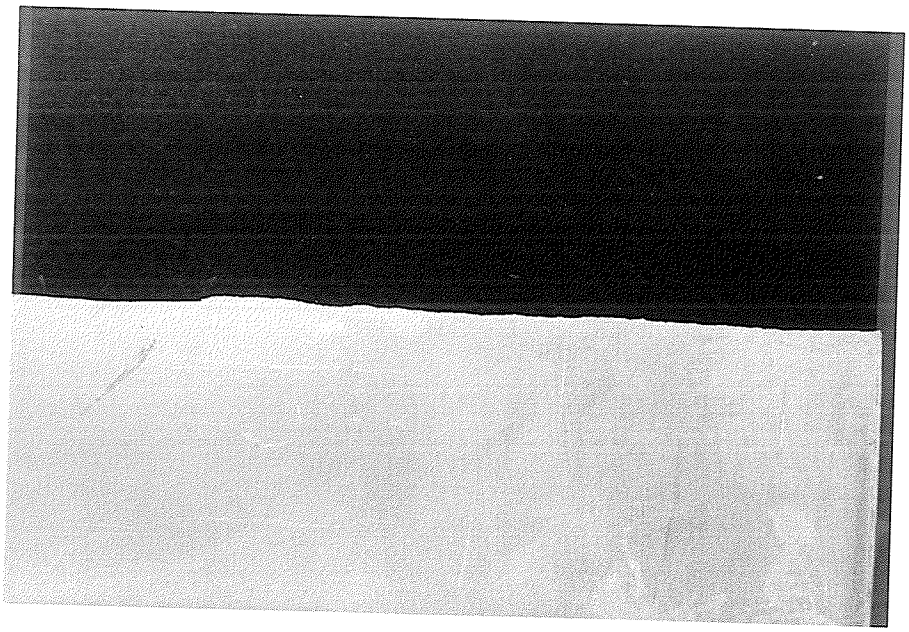

Fig. 5.5 Fractured Mode I Specimen After the Test.

observed that the crack surface through the thickness was at a 45° angle to the plane of the specimen, a typical fracture mode of thin sheet. A definite explanation for the 45° slant fracture has not been found, but it obviously is associated with the maximum shear stresses occurring at the 45° angle in the strip necking zone. This mechanism produces a three-dimensional plasticity effect ahead of the crack tip.

Fig. 5.6 is a photograph of a section from a fractured mixed mode specimen. In this specimen, the through-the-thickness slanted fracture surface produced different crack initiation angles for the front and back surfaces. However, after a short distance of oblique crack propagation, the crack path quickly changed to the crack path for a mode I specimen, i.e. perpendicular to the loading plane.

5.3.2 Applied Load vs Stable Crack Growth

A series of curves of the monotonically increasing load plotted against stable crack growth length are presented in Fig. 5.7. Crack length in this figure was measured in a direction perpendicular to the loading direction. For the mode I specimen, crack initiation occurred at a stress level of 13.8 ksi (95.2 MPa). After approximately 0.18 - 0.21 in. (4.57 - 5.33 mm) of stable crack growth had taken place,

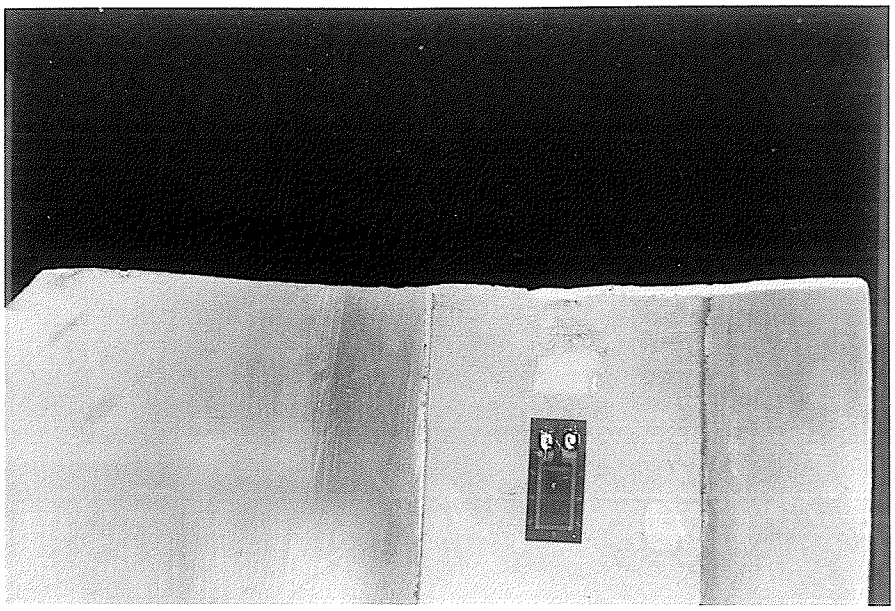

(a)

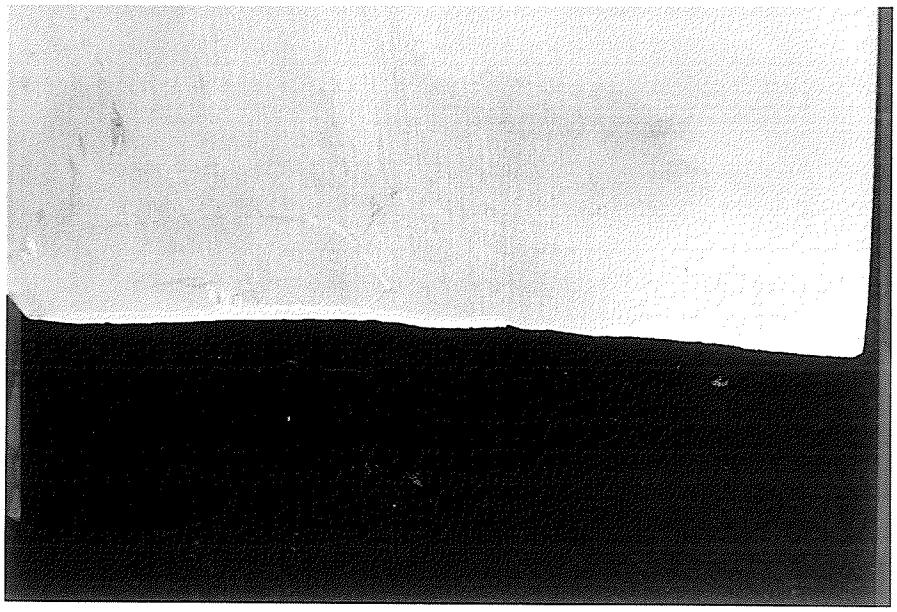

(b)

Fig. 5.6 Fractured Mixed Mode Specimen after the Test.
(a) Front Surface (b) Back Surface

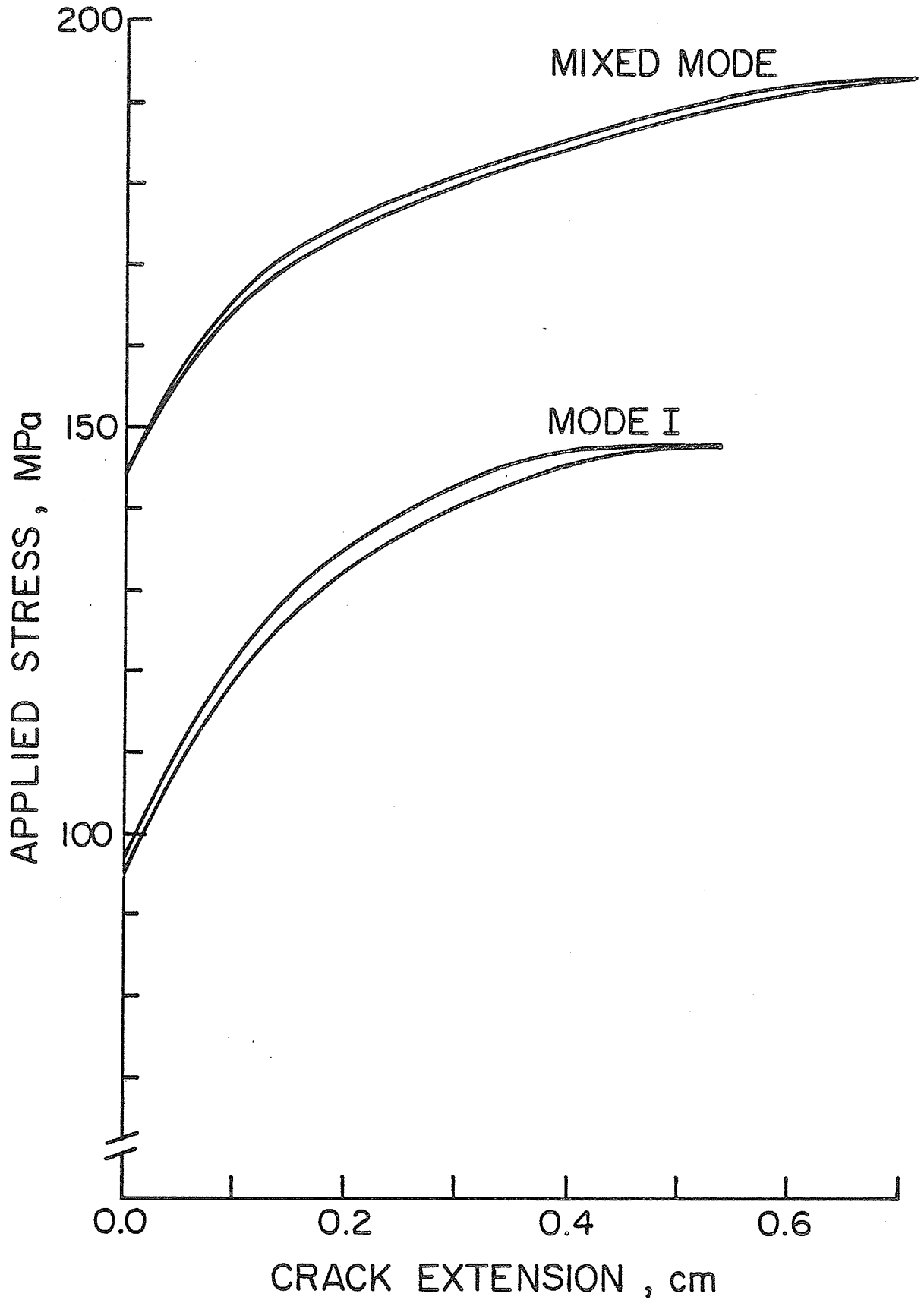

Fig. 5.7 Applied Stress vs Stable Crack Growth Curve.

unstable crack propagation began at a stress level of 21.5 ksi (148.2 MPa). In the mixed mode specimen, crack initiation was observed at a higher stress level of about 20.8 ksi (143.4 MPa). Prior to unstable crack propagation at 28.0 ksi (193.1 MPa), approximately 0.25 - 0.28 in. (6.35 - 7.11 mm) of stable crack growth had been observed.

These results show that ductile materials exhibit a significant amount of stable crack growth prior to unstable crack propagation. The amount of stable crack growth in the mixed mode case was far larger than that in the mode I case.

5.3.3 Variation of Strain Distribution

A plot of the normal strain, ε_{yy}, for the mode I specimen under an increasing stress is shown in Fig. 5.8 (for the locations of the strain gauges, refer to Fig. 5.3). Three pairs of strain gauges, No's 1 & 3, 4 & 6 and 7 & 8 were each mounted at the same vertical location on either side of the vertical centre line of the specimen to check the loading symmetry. The symmetric loading condition was well maintained as is evident from Fig. 5.8. In addition, the following items were observed for the mode I specimen.

(1) The normal strain increments from all of the strain gauges were linear with respect to the applied stress prior

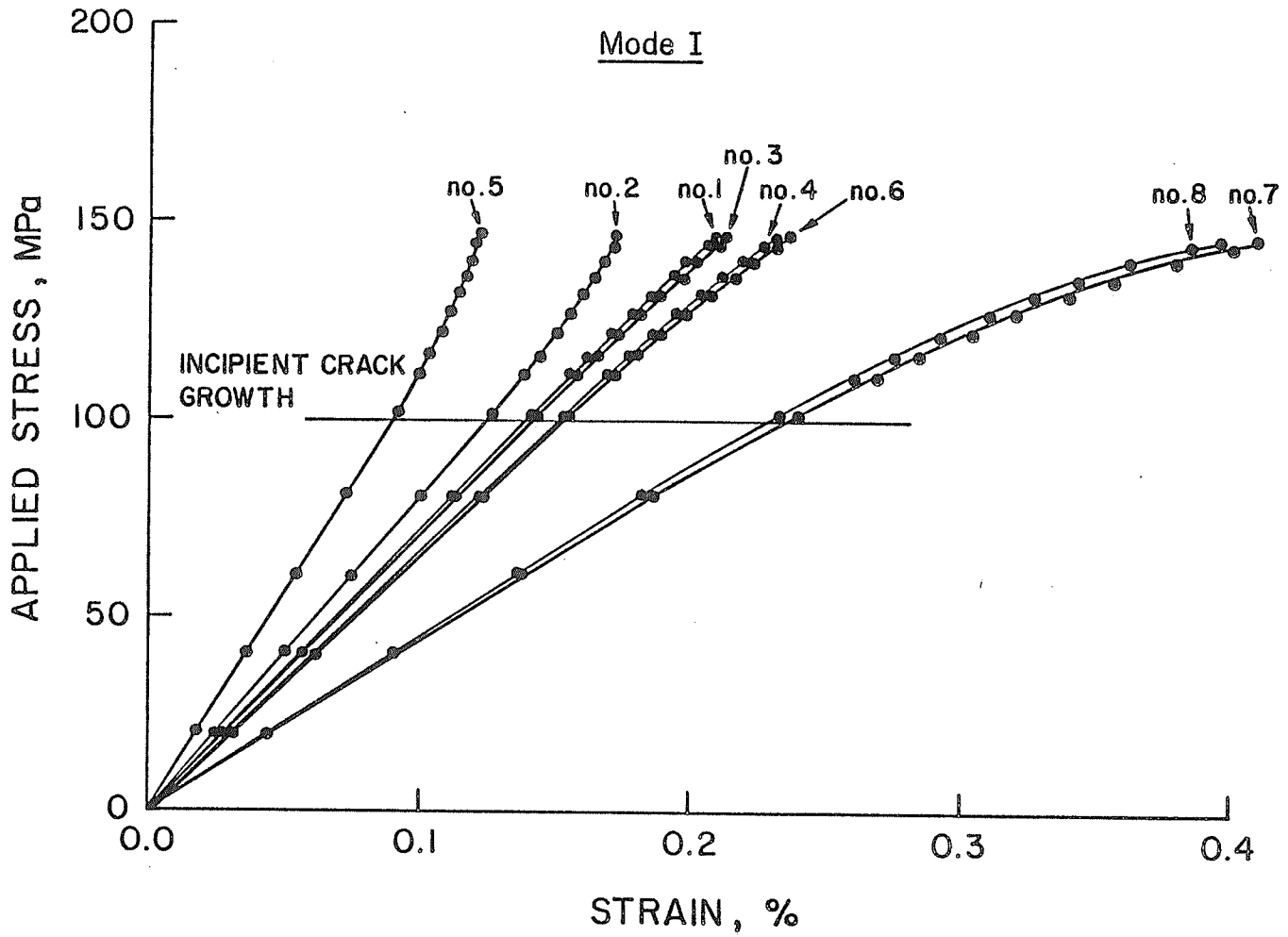

Fig. 5.8 Distribution of the ε_{yy} at the Eight Locations on the Mode I Specimen.

to crack initiation.

(2) Strain gauges No's 2 and 5, located along the vertical centre line of the specimen, displayed a decrease in the strain increments after crack initiation, while the remaining gauges showed an increase. This can be attributed to the fact that in the region near the growing crack the remaining specimen ligament carries more load, an effect that spreads to regions farther from the growth area. Thus the specimen carries more load near its edges than along the centre line, and consequently the strains at strain gauges No's 2 and 5 were always lower than those at the other gauges for any given load.

(3) Strain gauges No's 7 and 8 located closest to the crack tip on each side of the symmetry line, showed the greatest strain increments with the approach of the crack tip.

The variation of ε_{yy} for the mixed mode specimen is plotted in Fig. 5.9. Items (1) and (2) documented for the mode I specimen were also observed in this case. In addition, the followings were observed for the mixed mode specimen.
(1) Strain gauges No's 1, 4 and 7, located on the left side of the specimen, showed higher strains than their counterparts on the right. This was a consequence of the highly stressed crack tip being positioned much closer to the strain gauges

on the left side than those on the right side.

(2) As the crack propagated, the strain values at strain gauge No. 8 surpassed those at strain gauge No. 7, since the latter was within the region of load redistribution.

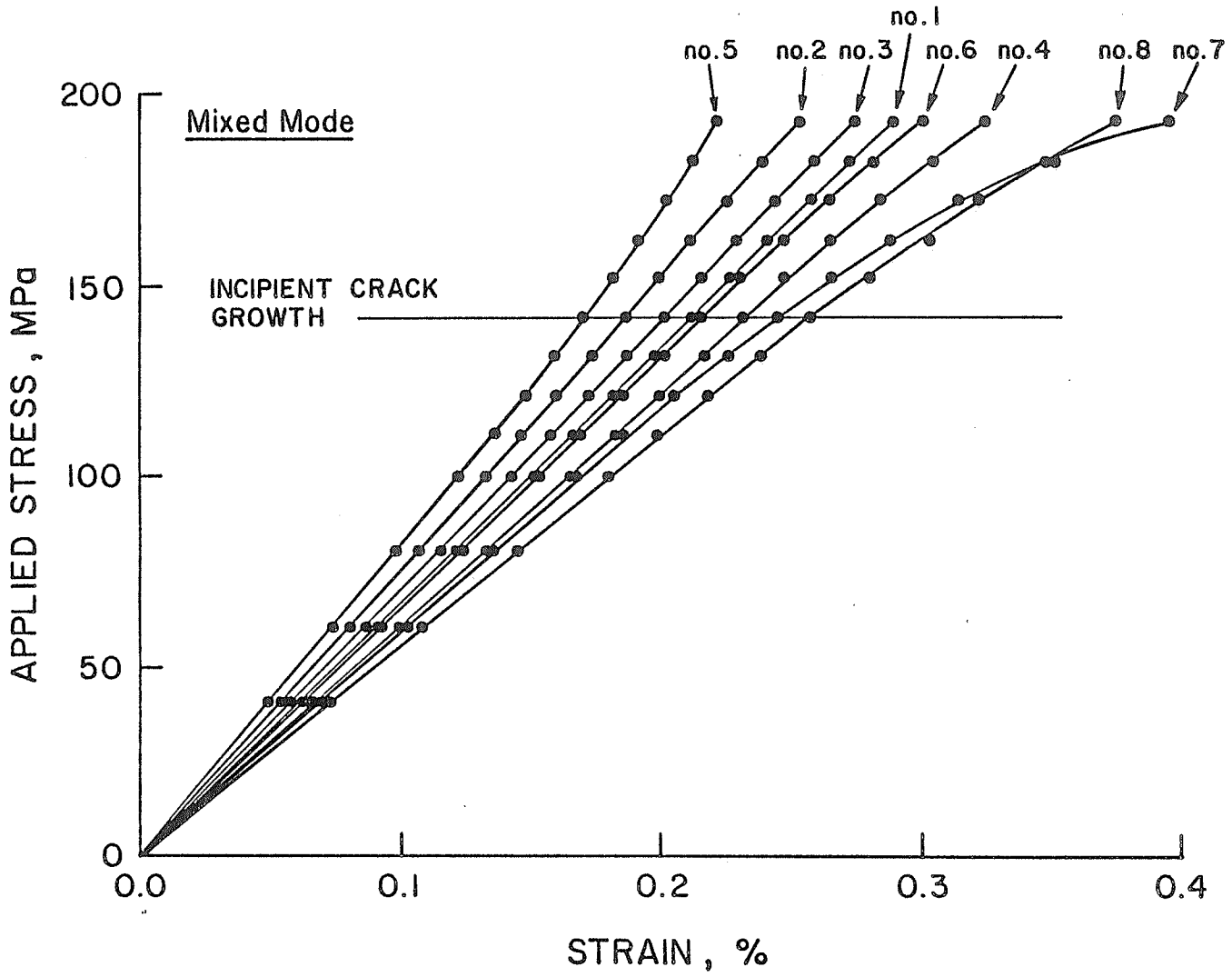

Fig. 5.9 Distribution of ε_{yy} at the Eight Locations on the Mixed Mode Specimen.

CHAPTER 6

FINITE ELEMENT ANALYSIS OF MODE I FRACTURE

6.1 Introduction

The TEPSCA finite element computer code with the numerical modelling technique described in Chapter 4 was used in a mode I type crack case study of 2024-T3 aluminum sheet. The numerical predictions of stable crack growth are compared with those previously obtained experimentally. Variations of the strains and stresses obtained during the numerical simulation of stable crack growth are presented, and crack tip parameters such as the crack opening displacement, crack opening angle, crack tip opening angle and nodal reaction force are discussed. The chapter ends with a discussion of the development of the plastic zone size.

6.2 Finite Element Modelling of the Mode I Specimen

As mentioned previously, there is a stress/strain singularity at the crack tip. However, in this analysis singular crack tip elements have not been used, since the finite element modelling of crack growth would require a complicated algorithm to migrate the singular element to the tip of the extended crack.

In modelling the crack tip using non-singular type elements, it is essential to incorporate a large number of degrees of freedom. With this in mind and in view of the computational costs involved, a mesh size varying gradually from very fine at the crack tip to coarse away from the crack tip was chosen for the finite element discretization.

A finite element model of the mode I specimen is shown in Fig. 6.1(a), with the details of the refined mesh surrounding the crack tip given in Fig. 6.1(b). Due to symmetric boundary conditions, only the first quadrant of the specimen was analyzed. A total of 358 elements were used together with 269 nodes representing 496 degrees of freedom. In order to minimize the possible discretization effects on crack growth, elements of relatively small size were distributed uniformly in the vicinity of the crack tip. A layer of identical quadrilateral elements representing the breakable elements was placed along the projected crack path. The length of each breakable element was 0.02 in. (0.508 mm), that is $\frac{1}{150}\, a_o$. This fine mesh was capable of producing an elastic stress concentration factor (the ratio of the normal stress, σ_{yy}, to the applied stress, σ) of 19.94 at the crack tip element, thus approaching the theoretical singularity.

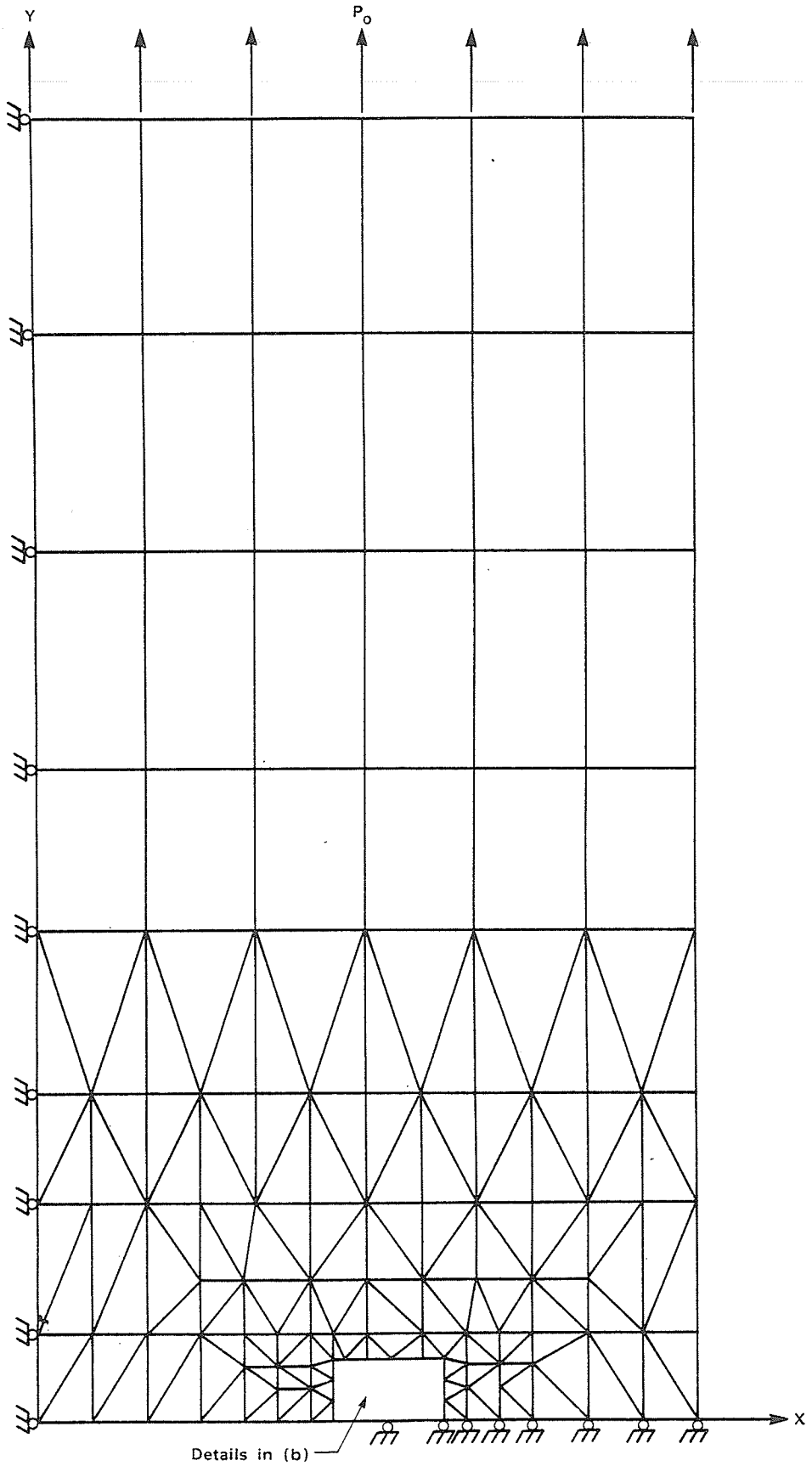

FIGURE 6.1

FINITE ELEMENT MODEL: MODE I
(a) OVERALL VIEW

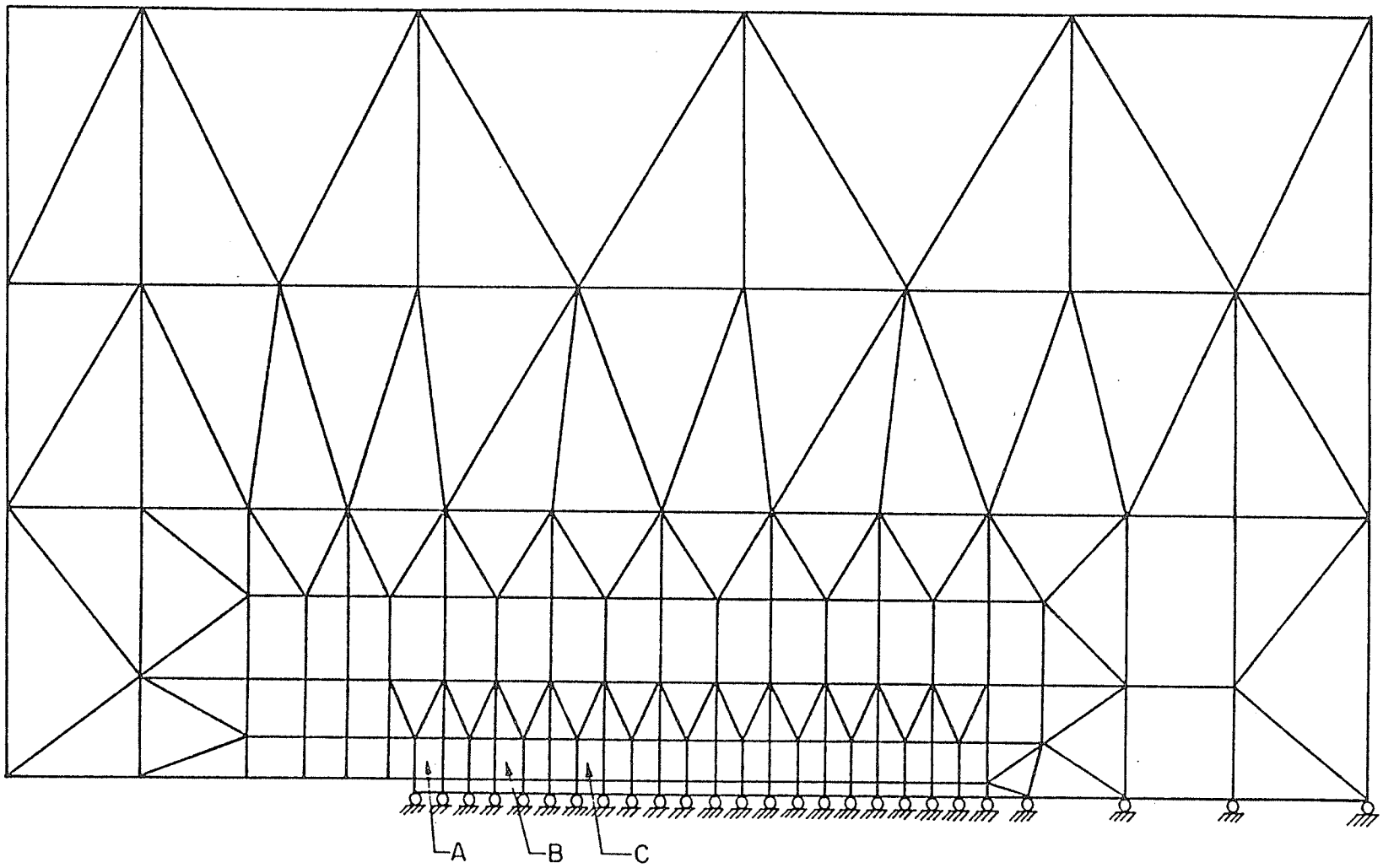

(b)

Fig. 6.1 Finite Element Model: Mode I.
(b) Crack Tip Region.

In addition to the material properties listed in Table 5.2, the following material properties were also used in the computations: σ_k = 45 ksi (310.3 MPa), E' = 206 ksi (3.55 GPa) and n = 10.

6.3 Computation of the Fracture Criterion

In order to investigate numerically stable crack growth in ductile materials under increasing loads, a fracture criterion must first be established. The effective rupture strain, $\bar{\varepsilon}_{rup.}$, was the fracture criterion used in this investigation, and was determined by the strain extrapolation technique previously described in section 4.3. The elastic-plastic stress analysis outlined in section 3.2 was performed until the onset of stable crack growth for the mode I specimen, occurring at the experimentally determined applied stress of 13.8 ksi.

Since the incremental stiffness theory was used throughout the elastic-plastic stress analysis, small load increments were required in order to follow sufficiently closely the stress-strain curve of the material. A total of 55 loading steps ranging from 0.1 - 0.3 ksi (0.69 - 2.07 MPa) were used to reach the point of crack initiation. An $\bar{\varepsilon}_{rup.}$ value of 11.5% was obtained from the cubic strain

extrapolation scheme using the first four breakable elements.

The effect of the finite element mesh size on $\bar{\varepsilon}_{rup.}$ value was further tested for two more breakable element sizes ($\frac{1}{100}\ a_o$ and $\frac{1}{300}\ a_o$). As shown in Fig. 6.2, the numerical study with $\frac{1}{100}\ a_o$ resulted in $\bar{\varepsilon}_{rup.} \doteq 11.3\%$ while the case with $\frac{1}{300}\ a_o$ produced $\bar{\varepsilon}_{rup.} = 11.5\%$. These results indicate that $\bar{\varepsilon}_{rup.}$ based on the strain extrapolation scheme is relatively insensitive to a range of crack tip element sizes, provided that the mesh is reasonably fine to accommodate the strain concentration at the crack tip.

6.4 Prediction of Stable Crack Growth

A simulation of stable crack growth was performed by using a value of 11.5% for $\bar{\varepsilon}_{rup.}$ in the previously described breakable element concept and nodal force relaxation algorithm. Again, small load increments were utilized in order to follow the stress-strain curve, a total of 70 loading steps being used from the point of crack initiation until unstable crack growth.

Fig. 6.3 shows the close agreement between the numerical and experimental results. The sloped part of the dotted line indicates crack growth due only to load increments. The slope decreasing (with increasing crack growth) is explicable

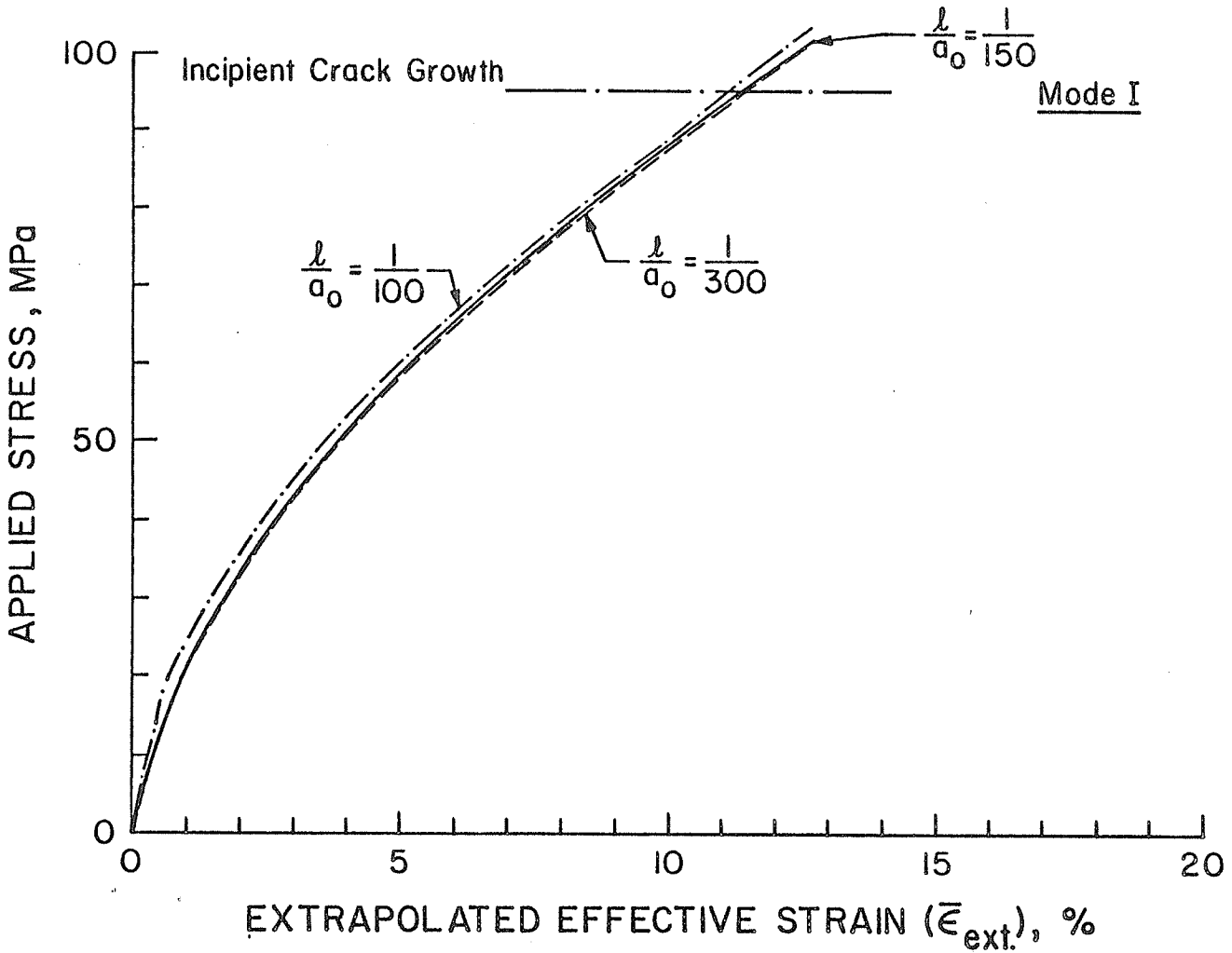

Fig. 6.2 Computation of $\bar{\epsilon}_{rup.}$ for Different Mesh Sizes: Mode I.

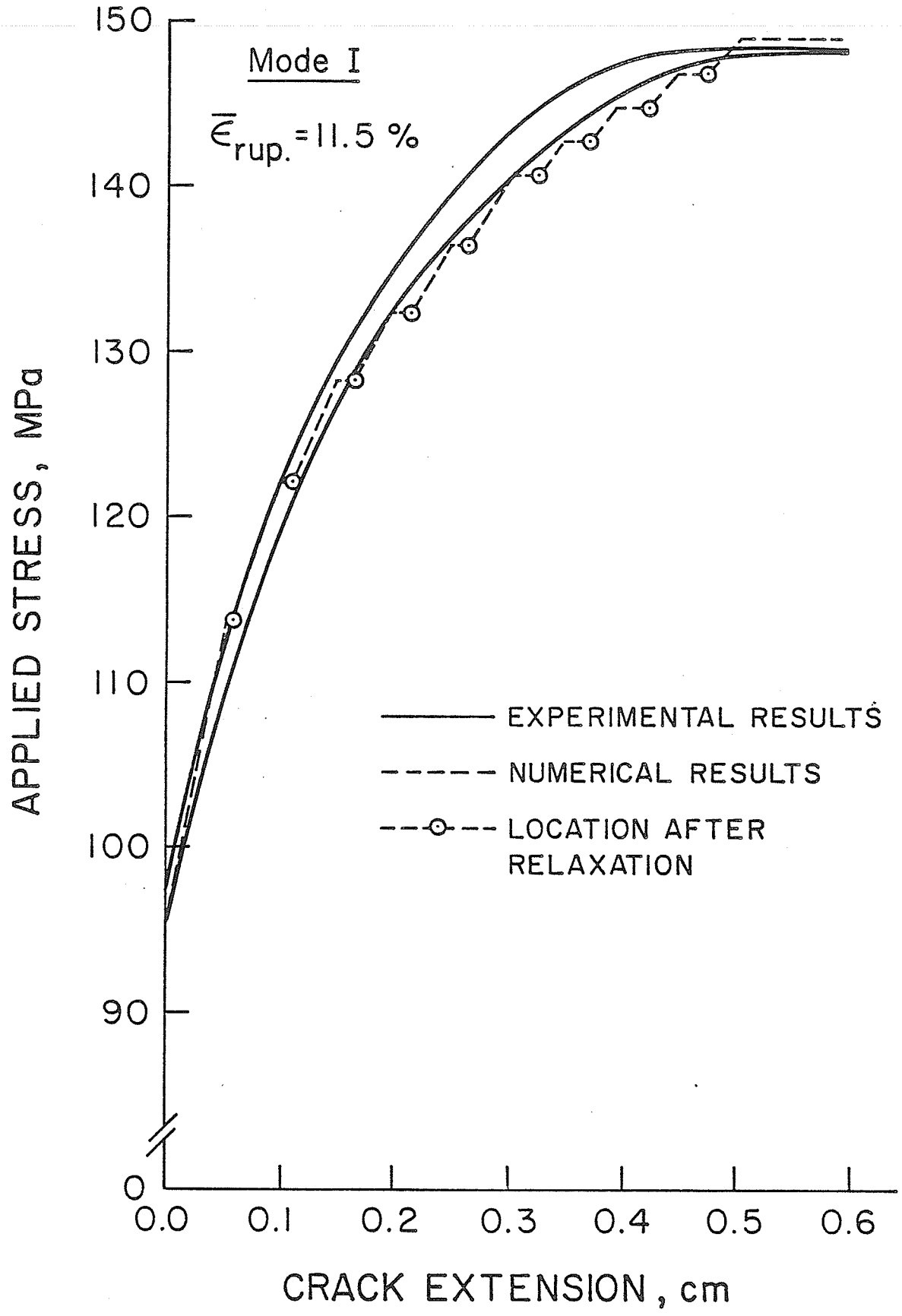

Fig. 6.3 Applied Stress vs Stable Crack Growth Curve: Mode I.

from a physical point of view, since the same load increment should cause a larger crack extension as the width of the remaining ligament decreases. The length of the horizontal portion of the dotted line, indicating the amount of crack growth due to the nodal force relaxation, also increased consistently. As can be seen from this figure, the first nine elements were broken through stable crack growth. Numerical instability was observed at the next load increment of 21.6 ksi (148.9 MPa) at which point unstable crack growth occurred.

It was observed that the applied stress at the onset of unstable fracture was about 56.5% higher than the applied stress at crack initiation. In addition, the total amount of stable crack growth prior to unstable fracture was about 7% of the original crack length. These factors indicate the margin of safety for ductile fracture after crack initiation.

The numerical sensitivity of crack growth to a change in the rupture strain was tested. The applied stress vs stable crack growth curves for two $\bar{\varepsilon}_{rup.}$ values (11% and 12%) are shown in Fig. 6.4. Crack initiation occurred at 13.5 ksi (93.1 MPa) and instability was observed at 21.0 ksi (144.8 MPa) for 11% rupture strain, with corresponding

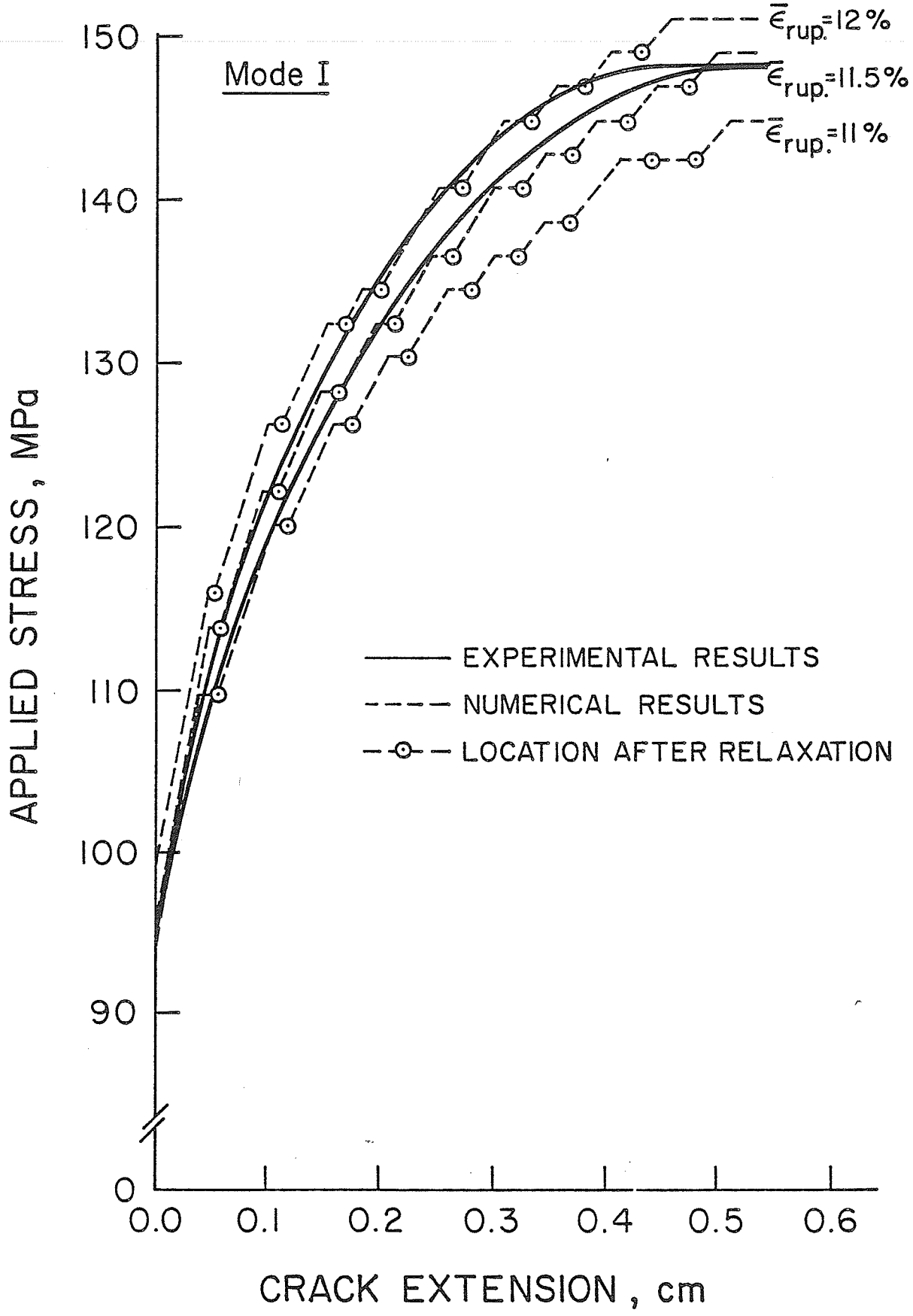

Fig. 6.4 Sensitivity of $\bar{\varepsilon}_{rup.}$ on Applied Stress vs Stable Crack Growth Curve: Mode I.

values of 14.4 ksi (99.3 MPa) and 21.9 ksi (151.0 MPa) for 12% rupture strain. Thus, these two case studies predicted stress levels for crack initiation and instability within $\pm$ 3% of those predicted using 11.5% as the rupture strain.

As described in the experimental results, the fracture mode for the so-called 'plane stress' structure is in fact a 45° through the thickness slant-type fracture, and is thus a complicated three-dimensional problem. However, as demonstrated above, the current algorithm with the simplying two-dimensional assumption can simulate stable crack growth and closely reproduce the applied stress vs stable crack growth curve. The generally good agreement obtained between the numerical and experimental results provides confirmation that the numerical techniques used in this analysis give realistic estimates of the elastic-plastic stress-strain fields occurring in the test specimens. These reasonable results were generated despite the fact that the stress-strain fields in the immediate vicinity of the crack tip were not very accurate, since the small strain assumptions meant that the large deformation producing crack tip blunting could not be modelled exactly.

6.5 Variation of the Strain and Stress Distributions

6.5.1 Strain Distribution

Fig. 6.5 illustrates the variation of the loading direction strain component, ε_{yy}, at the eight locations where strain gauges were mounted on the mode I specimen. The figure shows that the numerical results are in general well correlated with the experimental measurements. Some discrepancies are to be noted with increased crack growth, especially at strain gauge No's 7 and 8. This is attributed to the fact that experimentally the crack path was not exactly perpendicular to the loading plane, which was assumed in the finite element analysis. In addition, there was a slight difference between the numerically and experimentally obtained crack lengths. The maximum difference between the experimental and numerical results is $\pm$ 0.5% before crack initiation and $\pm$ 2% after crack initiation.

In this analysis the amount of crack growth is determined by the distribution of the effective strain, $\bar{\varepsilon}$, ahead of the crack tip. Fig. 6.6 shows the $\bar{\varepsilon}$ distribution in the breakable elements ahead of the crack tip for the mode I specimen immediately before and after the nodal force relaxation of each breakable element. The crack tip element attained an

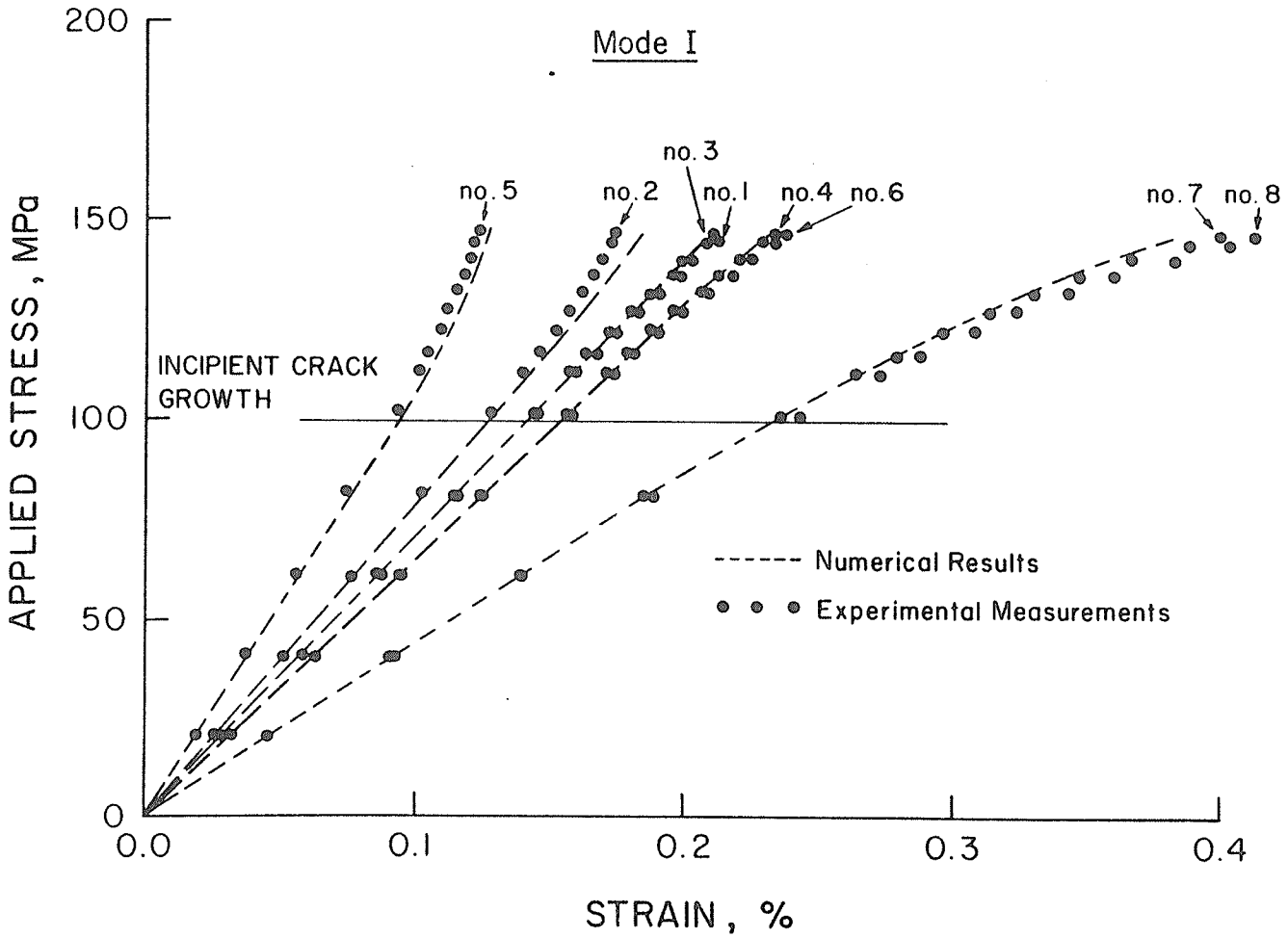

FIGURE 6.5

STRAIN DISTRIBUTION AT THE EIGHT LOCATIONS: MODE I

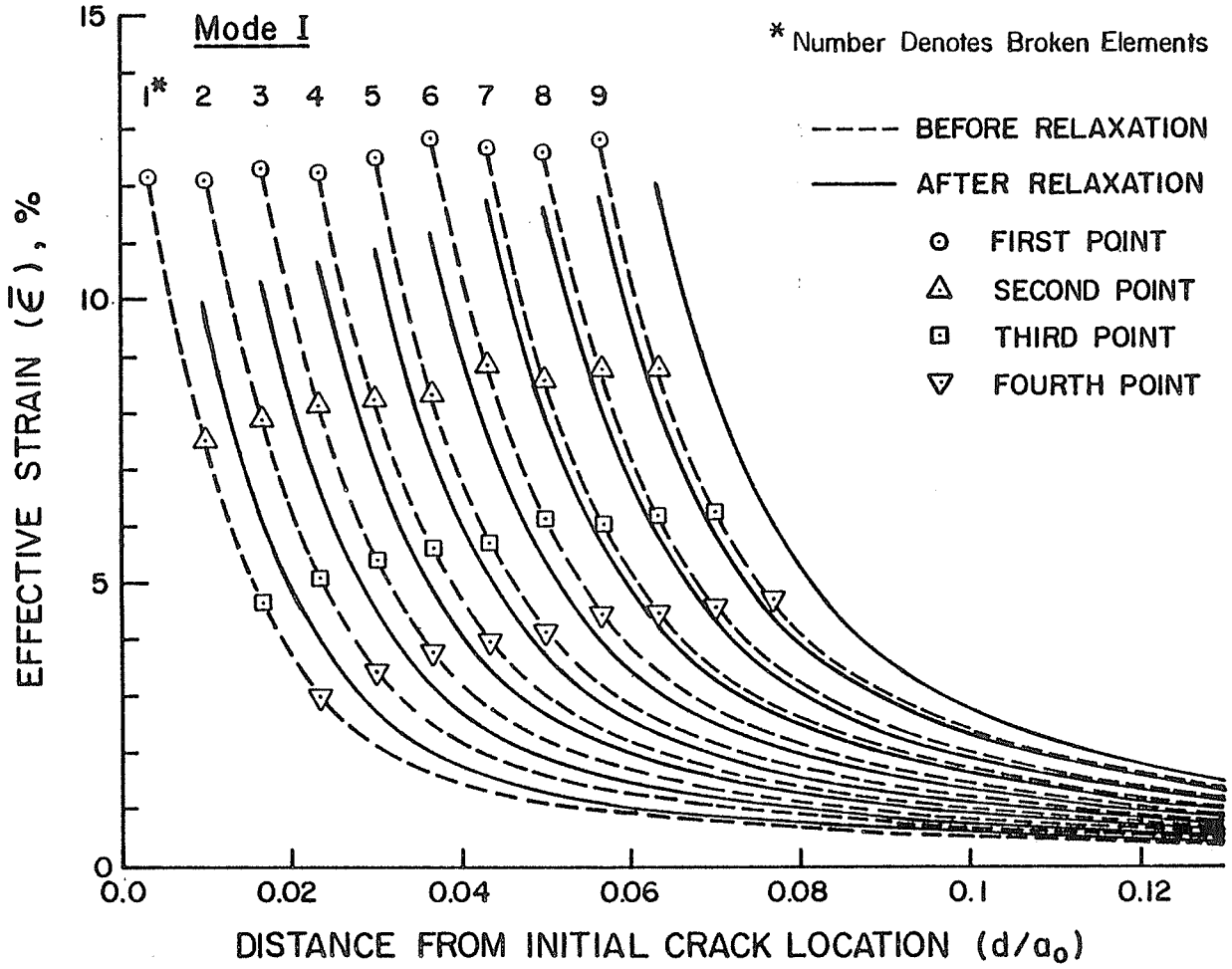

Fig. 6.6 Effective Strain Distribution Ahead of the Crack Tip: Mode I.

$\bar{\varepsilon}$ value of approximately 12.5% before the nodal force relaxation. The marked points in this figure were used for the strain extrapolation. Looking at fixed points, the redistribution of the accumulated stress from the broken element increases the strain distribution at each position ahead of the crack tip. However, using the moving crack tip as the reference position after each nodal force relaxation, there is a reduced strain value at locations measured relative to the crack tip. This is a characteristic of stable crack growth [18]. Thus, in order to reach the fracture criterion, $\bar{\varepsilon}_{rup.}$, additional load increments are required to increase the $\bar{\varepsilon}$ distribution ahead of the crack tip.

Since the $\bar{\varepsilon}$ value at the crack tip element continuously increases immediately following each nodal force relaxation, it is evident that a progressively smaller load increment is required for subsequent crack growth. Eventually, after the nodal force relaxation of the ninth element, the strain distribution ahead of the crack tip is sufficient to promote further crack propagation without any further load increment. This implies that the instability condition has been reached.

From the numerical results, it was also noticed that the element strain value in the crack line direction, ε_{xx},

was much smaller than that in the thickness direction, ε_{zz}. The ε_{zz} value results in necking and may be the main source for the 45° slant-type fracture.

6.5.2 Stress Distribution

Fig. 6.7 shows the distribution of the effective stress, $\bar{\sigma}$, in the breakable elements ahead of the crack tip for the mode I specimen immediately before and after the nodal force relaxation of each breakable element. This figure illustrates that the $\bar{\sigma}$ distribution ahead of the growing crack tip is invariant with the position of the crack. As might be inferred from the $\bar{\varepsilon}$ distribution, the $\bar{\sigma}$ distribution at locations measured relative to the moving crack tip drops immediately after the nodal force relaxation. However, comparing the $\bar{\varepsilon}$ distributions immediately after each nodal force relaxation, they increased consistenly as succeeding elements were broken. Finally the state was reached where the $\bar{\sigma}$ distribution immediately following the ninth nodal force relaxation was in fact greater than just before the first nodal force relaxation. This again corresponded to the instability condition.

The stress histories for the three selected elements A, B and C shown in Fig. 6.1 are presented in Fig's 6.8

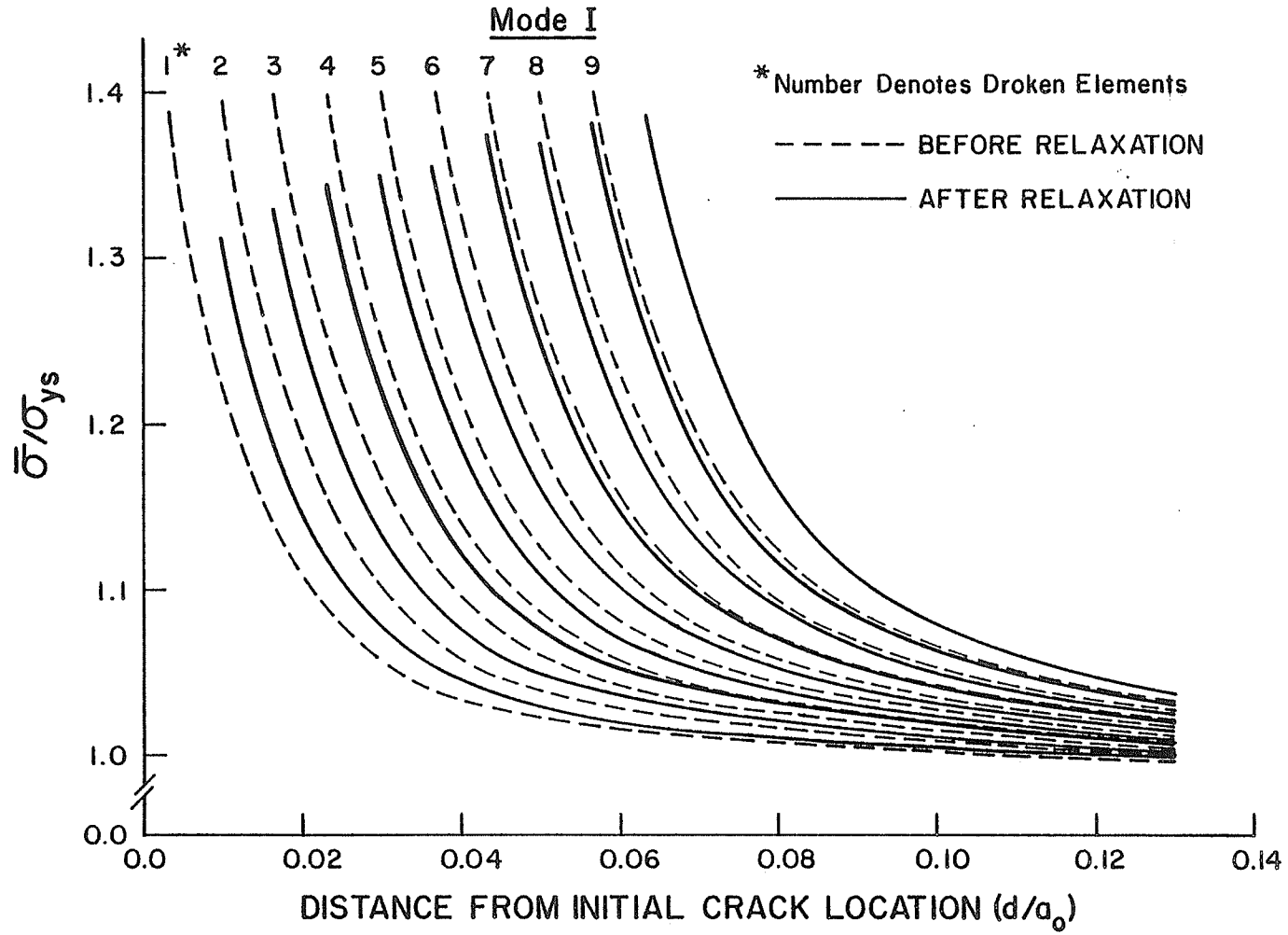

Fig. 6.7 Effective Stress Distribution Ahead of the Crack Tip: Mode I.

through 6.10. As can be seen in these figures, the loading direction stress component, σ_{yy}, increases and becomes the dominating component for all three elements as the crack tip approaches. This stress value is reduced drastically during the nodal force relaxation, and approaches zero some time after the crack tip has passed. This certainly indicates a correct simulation of the crack growth process, since the traction-free boundary condition imposed on the open crack face requires that the σ_{yy} value be zero (assuming negligible deviation of the stress calculation points from the crack surface).

The specimen width direction stress component, σ_{xx}, for an element ahead of the crack tip is initially tensile and approximately one-half of the σ_{yy} value, becomes compressive during nodal force relaxations. This indicates that for stable crack growth there are high compressive stresses along the newly created crack surface in the crack line direction, representing a residual compressive stress in a plastically deformed wake region.

The shear stress component, σ_{xy}, initially a small positive value, becomes slightly negative as the crack tip approaches, and vanishes after the crack tip has passed.

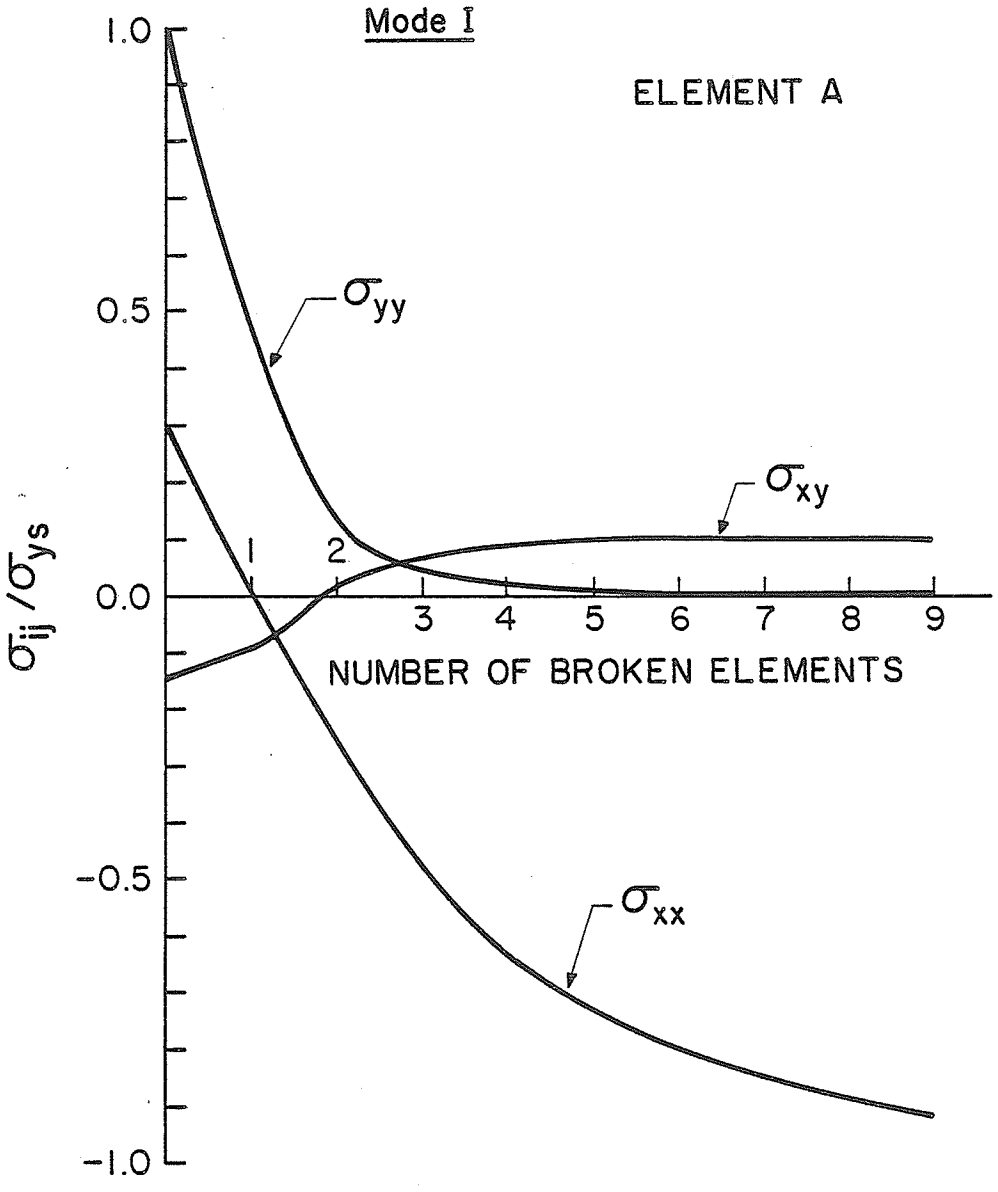

Fig. 6.8 Stress History of Element A: Mode I.

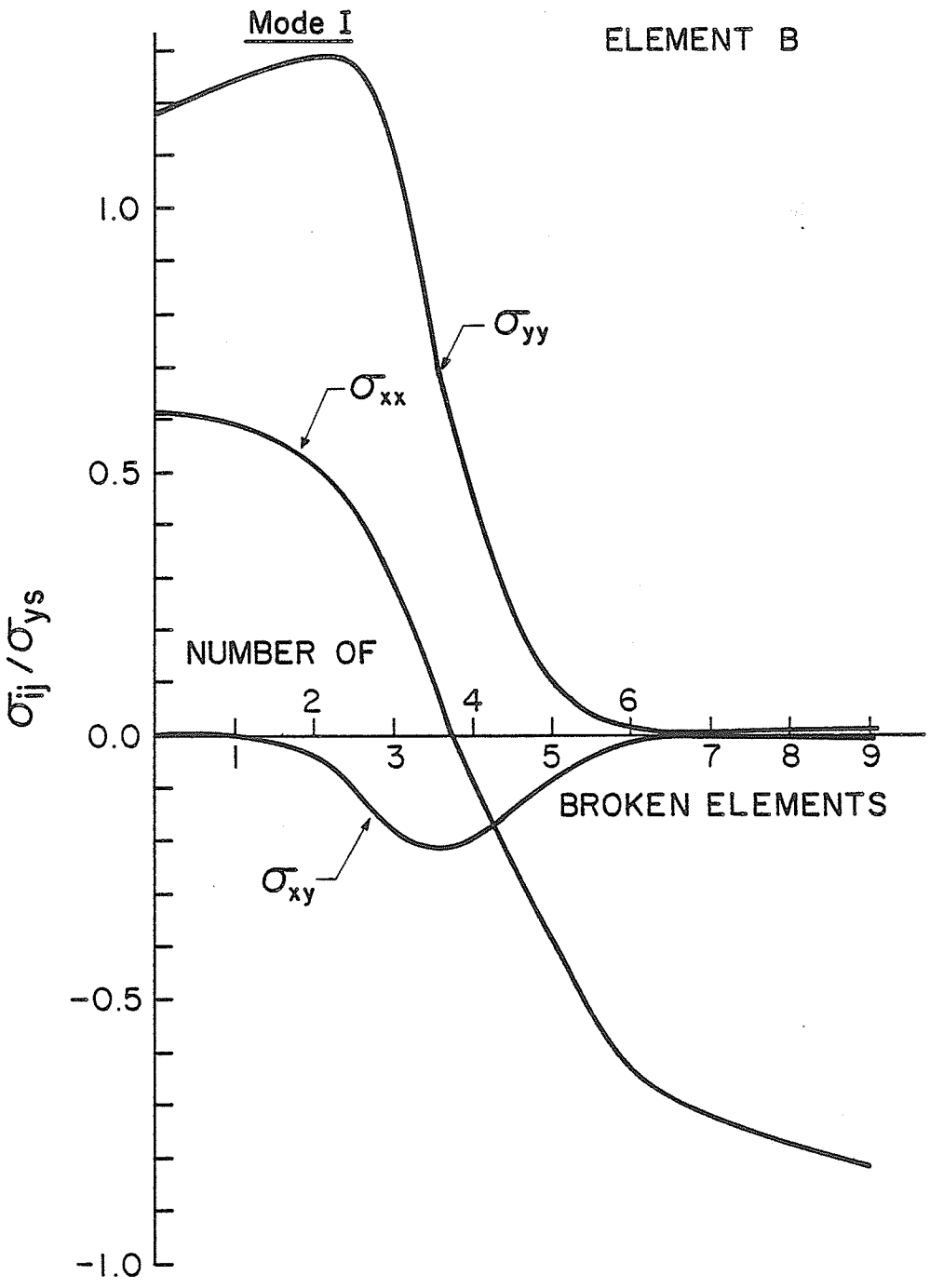

Fig. 6.9 Stress History of Element B: Mode I.

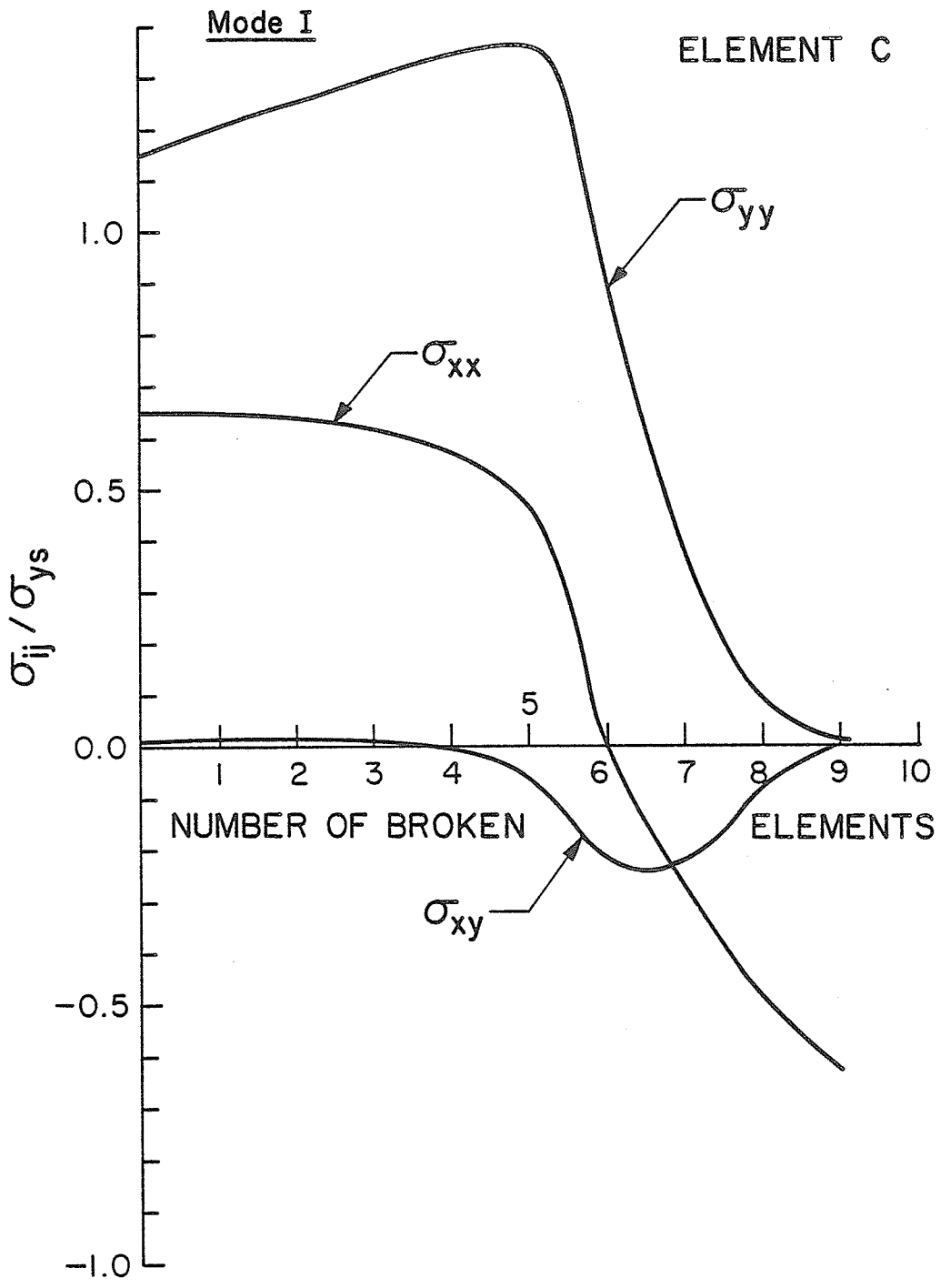

Fig. 6.10 Stress History of Element C: Mode I.

A similar variation in the σ_{xx}, σ_{yy} and σ_{xy} distributions has been reported by de Koning et al [50] for the plane stress case. This description of the stress history at particular locations on the specimen reinforces the previously made point that the elements surrounding the growing crack tip experience essentially the same stress field as those surrounding the stationary crack.

6.6 Variation of Crack Tip Parameters

Fig. 6.11 shows four stages of the crack face profile of the mode I specimen: in the elastic regime, at the onset of crack growth, and before and after the nodal force relaxation of the first breakable element. This figure illustrates the consequences of the strain singularities associated with the crack face profiles under monotonically increasing loads. The elastic crack face has a sharp profile, indicating the $r^{-1/2}$ strain singularity which dominates at the crack tip, while the plastic strain singularity during crack growth results in a more blunted profile.

The crack face profiles of the mode I specimen at various stages of crack growth are presented in Fig. 6.12. As shown in this figure, the crack face profile becomes

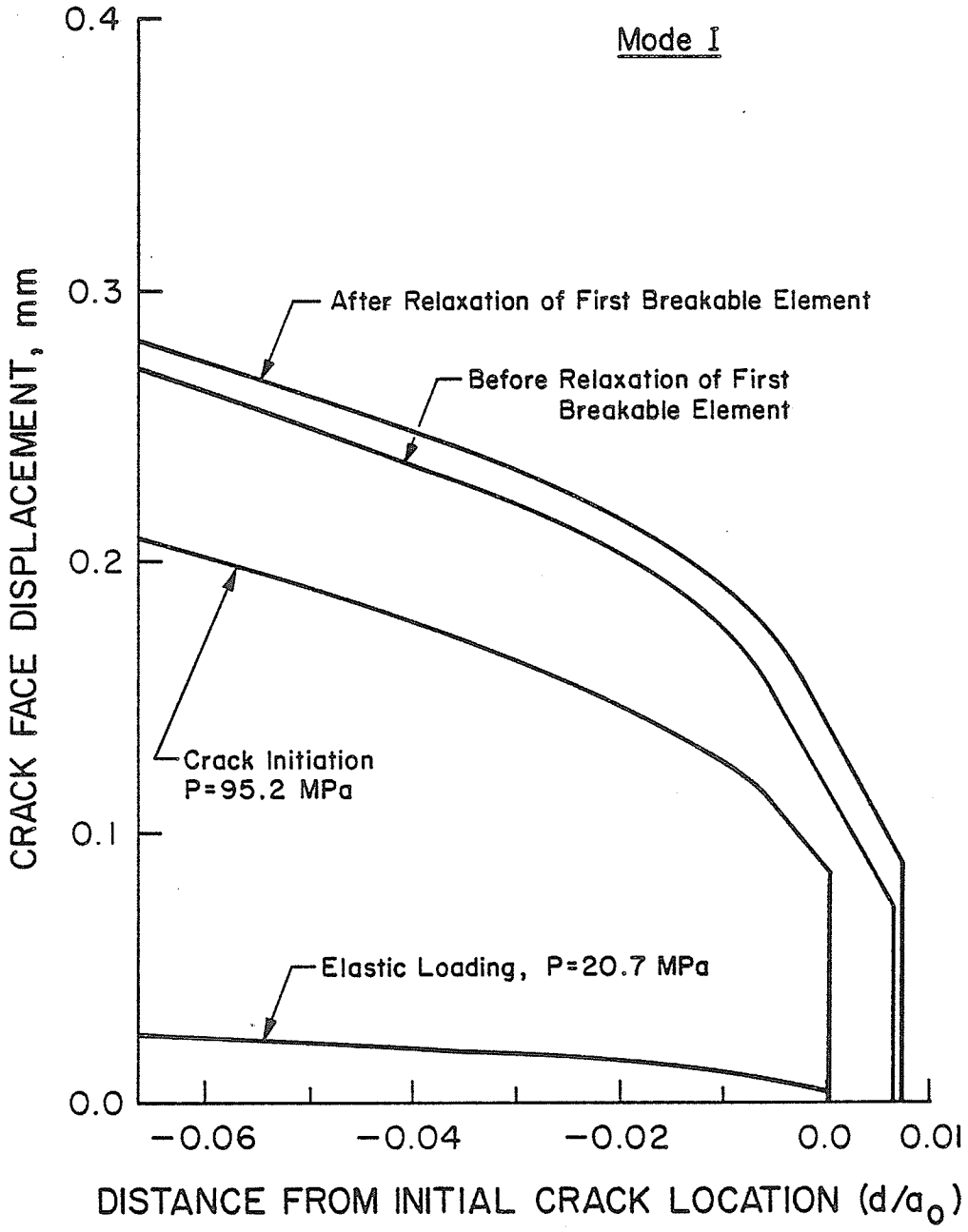

Fig. 6.11 Crack Face Profile (Stationary): Mode I.

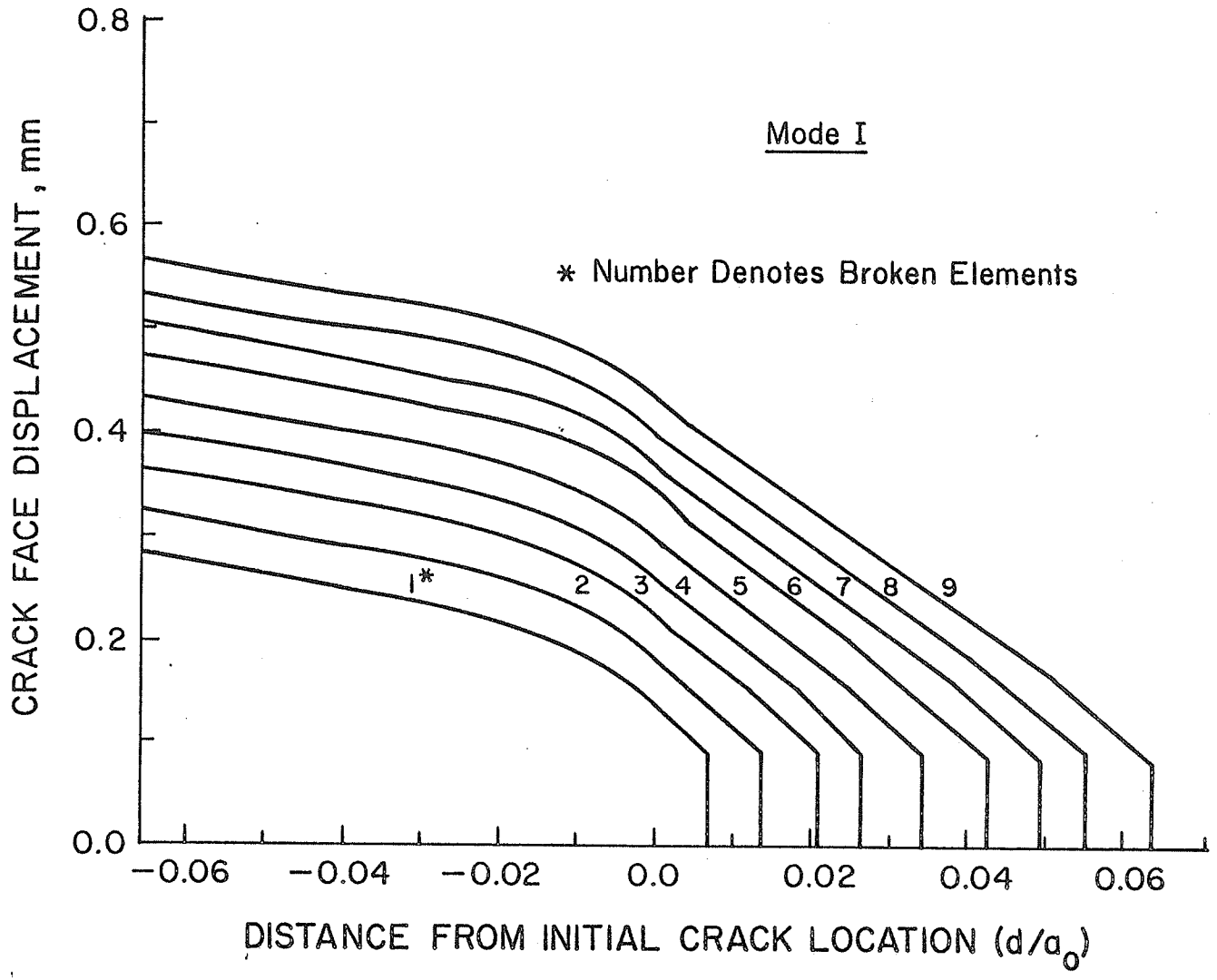

Fig. 6.12 Crack Face Profile (Growing Crack): Mode I.

sharper after crack initiation, suggesting the possibility of a change in the order and nature of the strain singularities at the tip of an extending crack. During stable crack growth, the crack face maintains the same profile.

Several crack tip parameters such as the crack opening displacement (COD), crack opening angle (COA) and crack tip opening angle (CTOA) have been evaluated from the numerical results.

Fig. 6.13 shows the variation of the COD, δ_o, which is defined as an opening displacement at the location of the original crack tip. As shown in this figure, the COD value increases linearly as the crack extends.

Fig. 6.14 presents the variations of the COA and the CTOA at various stages of crack growth. The value of the COA, α_o, is defined as

$$\alpha_o = \frac{\delta_o - \delta_{oi}}{\Delta a}$$

where δ_{oi} denotes the opening displacement at crack initiation and

Δa is the amount of crack extension.

The value of the CTOA, α_ℓ, is defined as the angle formed between the opposing crack faces at the extending crack tip.

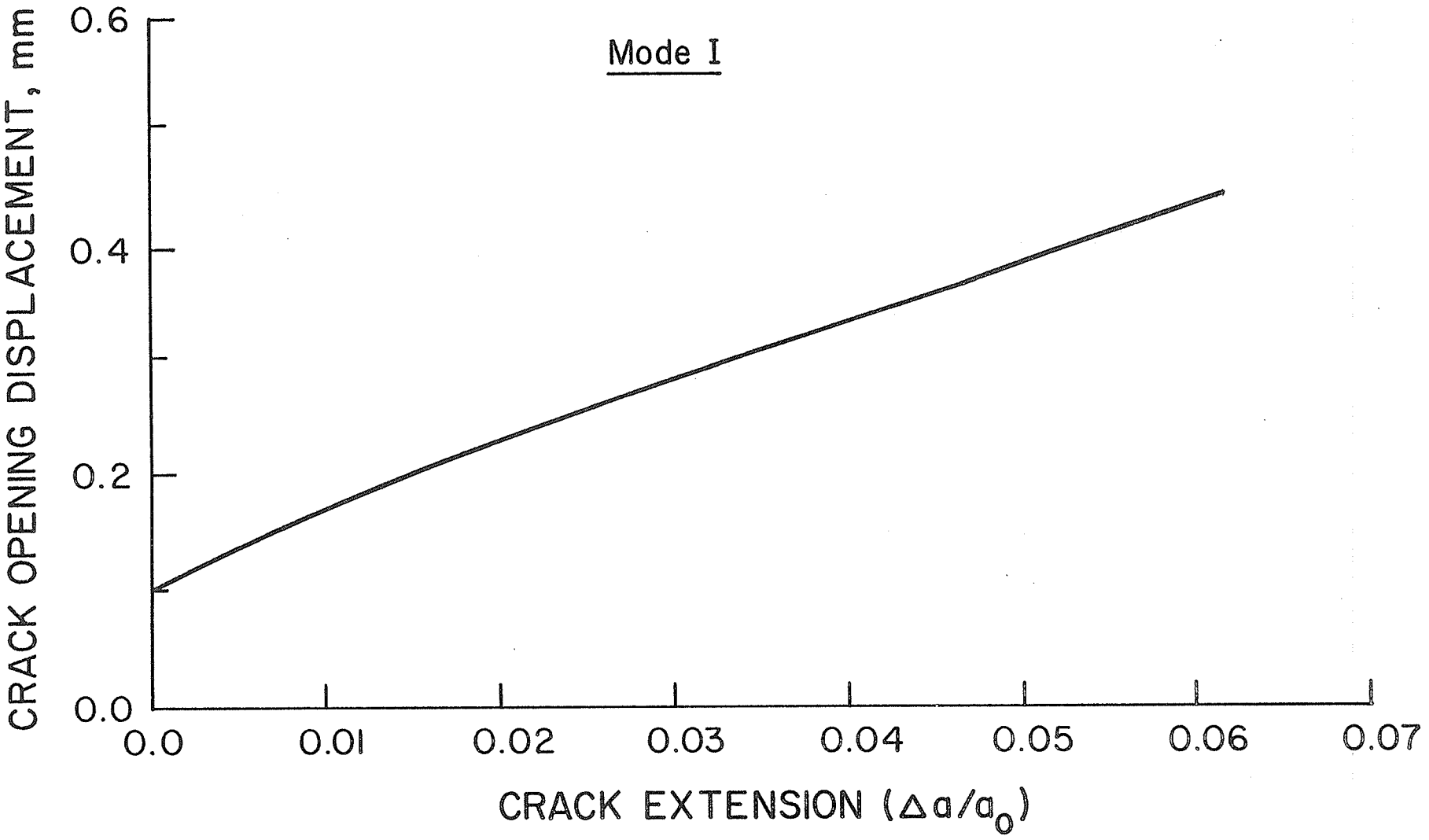

Fig. 6.13 COD vs Crack Extension: Mode I.

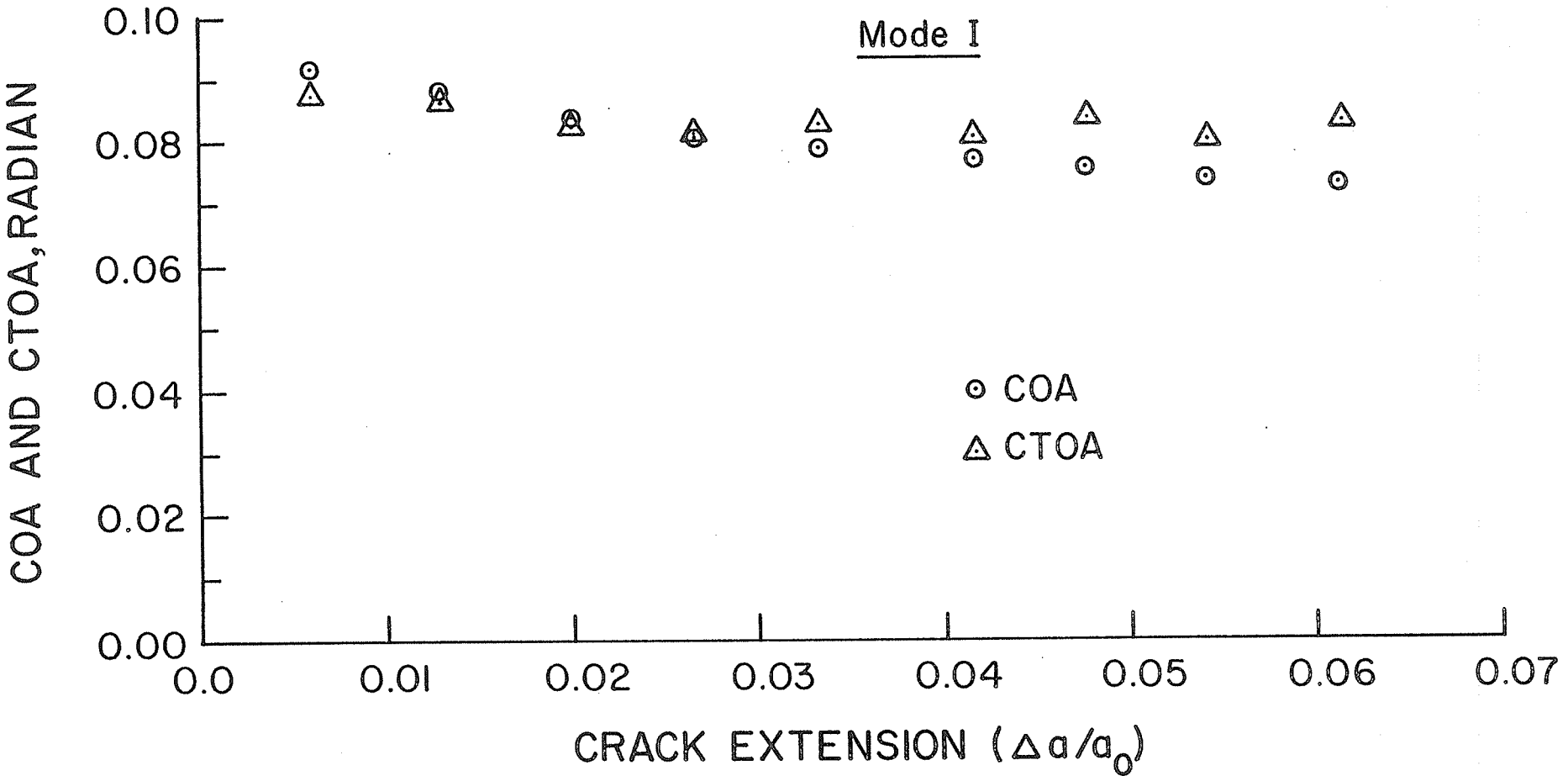

Fig. 6.14 COA, CTOA vs Crack Extension: Mode I.

Fig. 6.14 shows that the CTOA becomes constant after a certain amount of crack growth, while the COA decreases consistently. The high CTOA value at crack initiation may be attributed to the crack blunting phenomenon of ductile materials. As pointed out by Andersson [46], crack initiation may be governed by the COA value, and the subsequent crack growth controlled by the constancy of the CTOA. This constancy of the CTOA has been observed previously in plane stress analysis by de Koning [50]. Sorensen's study [59] of a plane strain analysis, however, indicated that the CTOA is strain-hardening dependent.

Fig. 6.15 presents the variation of the nodal reaction force, F, which was used to redistribute the accumulated stress of a broken element to the surrounding elements during the relaxation steps. The F values are constant within a few percent, similar to the results produced by Kanninen et al [58].

6.7 Development of the Plastic Zone

In finite element computations, plasticity is defined by the ratio of the effective stress to the yield strength of the material. Areas in which this value exeeds unity are denoted in Fig. 6.16 as the plastic zone for various stages

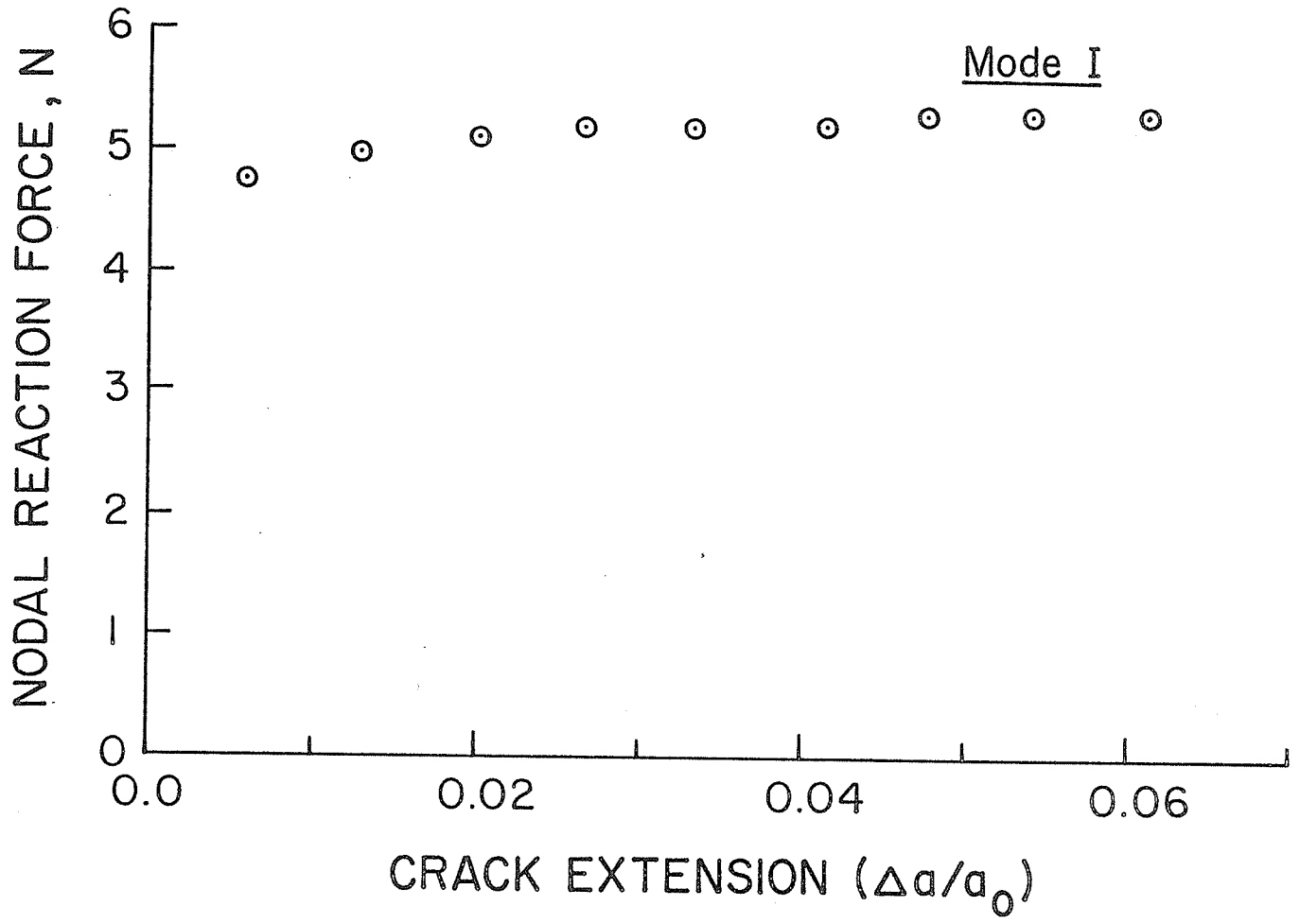

Fig. 6.15 Nodal Reaction Force vs Crack Extension: Mode I.

of crack growth of the mode I specimen. This plastic zone initially expands more rapidly in the crack line direction. However, the maximum zone eventually is positioned at approximately 45° to the crack line direction as the crack extends.

As the crack extends under monotonically increasing loads, the region of the plastic zone behind the crack tip unloads to an elastic state, while that portion of the zone ahead of the crack tip expands. This phenomenon results in the translation of the plastic zone ahead of the crack tip while leaving a wake of permanently strained material (that is, residual plastic deformation) behind the moving crack tip. As the crack grows, the plastic zone spreads over a continually larger area, finally reaching a state of gross plasticity.

The wake of residual plasticity behind an extending crack is directly related to the stress history, ductility and strain hardening characteristics of the material. For more ductile materials, it is likely that this wake zone will be larger and the difference in applied load level between crack initiation and instability greater. Thus it may be pointed out that the stable crack growth behavior of a material can be attributed directly to its ability to form a permanently strained zone behind an extending crack.

Mode I

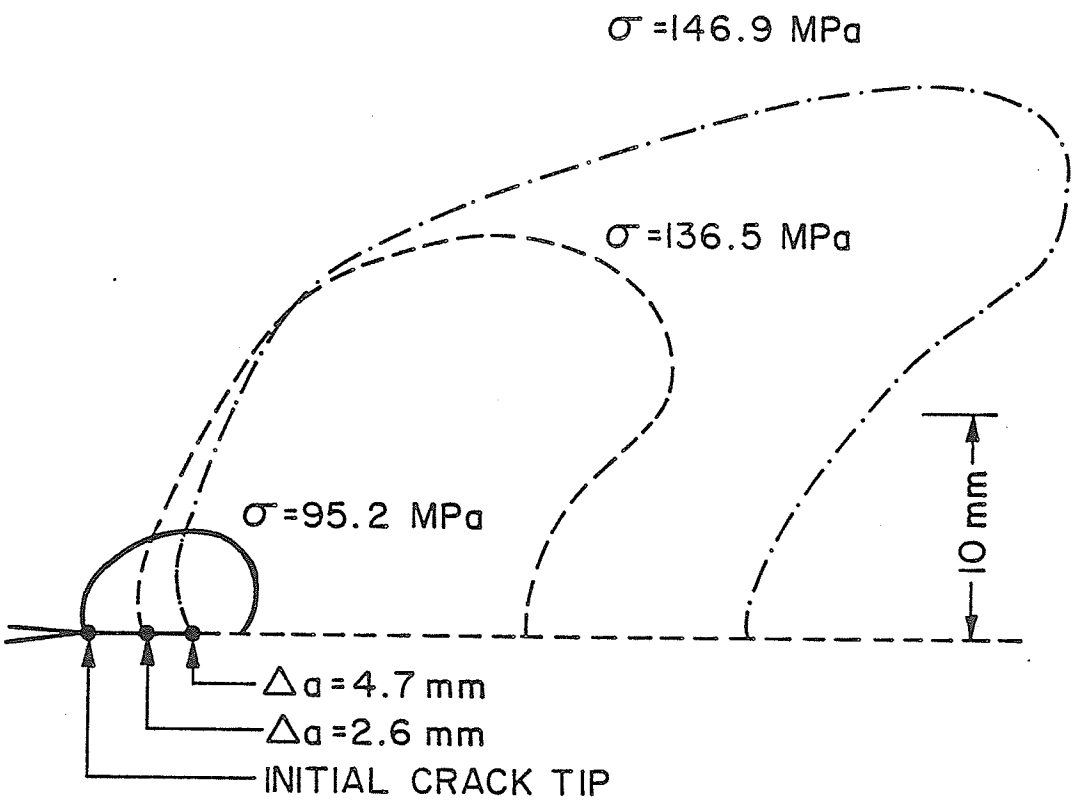

Fig. 6.16 Development of the Plastic Zone: Mode I.

CHAPTER 7

FINITE ELEMENT ANALYSIS OF MIXED MODE FRACTURE

7.1 Introduction

The Griffith-Irwin theory described in Chapter 2 was developed primarily for mode I fracture problems. However, for engineering fracture problems of a practical nature, the existing cracks quite often are situated at an angle to the applied load, resulting in mixed mode[+] fracture conditions. As a consequence of this, mixed mode fracture has recently received considerable attention from investigators in the field of fracture mechanics.

To predict mixed mode crack growth it is necessary to determine both a fracture criterion and the crack path. Various methods may be used in an attempt to determine the crack path. The crack path can be predicted by analyzing local field quantities in the crack tip region such as stress, strain and strain energy density. Alternatively the crack path may be predicted by analyzing the variation of the total

---

[+]Defined in this thesis as a combined effect of mode I and mode II fracture

elastic energy of the structure with respect to a small extension of the crack. Originally these criteria were proposed primarily to predict only the crack initiation angle in the fracture of brittle materials. However, with the aid of the finite element method, these techniques have been extended beyond the initial crack tip region to predict the total crack path.

This chapter begins by reviewing the various criteria used for predicting the crack path in the fracture of brittle materials. The feasibility of extending these criteria to the fracture of ductile materials is discussed. In addition, a new criterion, which is based on the effective strain at the crack tip, is proposed. Stable crack growth in a mixed mode fracture problem is subsequently analyzed following the same procedure used in the previous mode I case study.

7.2 Review of the Prediction of Crack Path in Brittle Material

7.2.1 Maximum Tangential Stress Criterion

Erdogan and Sih [84] have analyzed the crack extension in a plate with a central crack of length 2a, inclined at an angle β to the direction of the axially applied uniform stress σ (Fig. 7.1). The stress intensity factors K_I and K_{II} for

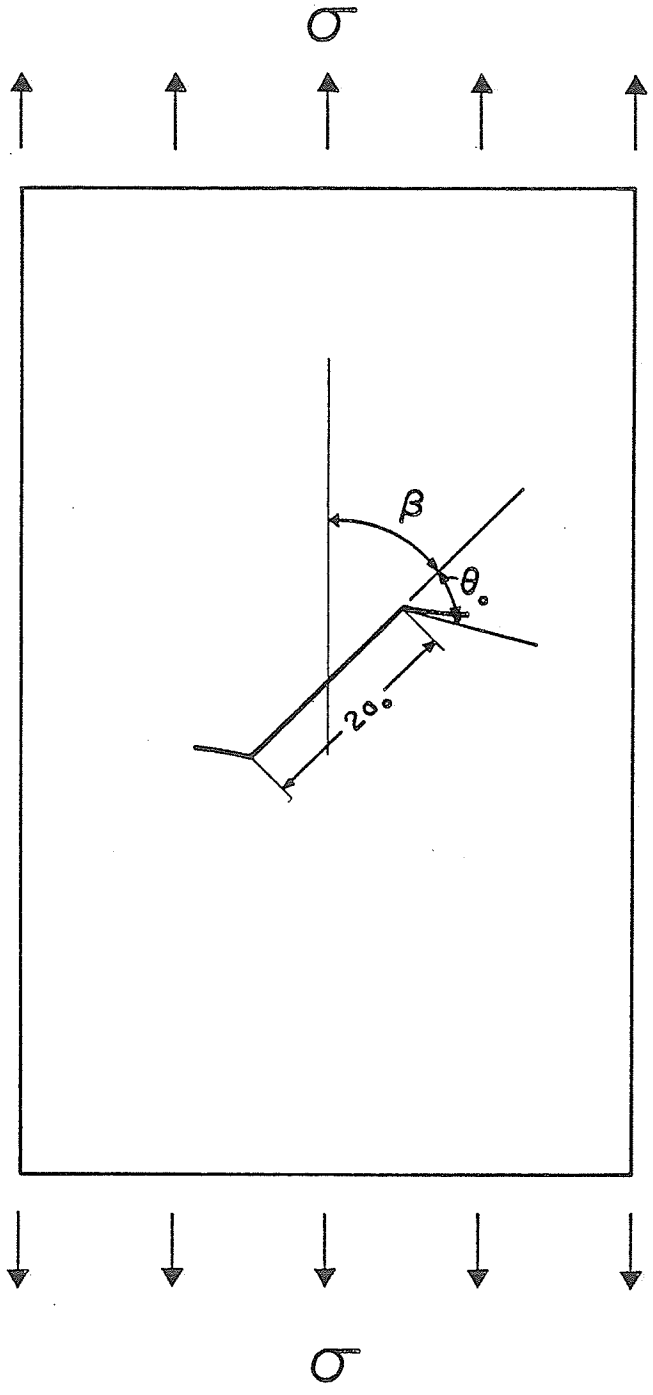

Fig. 7.1 The Configuration of the Mixed Mode Crack Problem.

this mixed mode fracture problem are:

$$K_I = \sigma\sqrt{\pi a}\,\sin^2\beta$$
$$K_{II} = \sigma\sqrt{\pi a}\,\sin\beta\cos\beta \quad . \tag{7.1}$$

They had assumed that the crack would propagate in the radial direction at which the tangential stress at the crack tip (distributed with respect to local coordinate θ) is maximum. That is the crack propagates in the direction at which the stress component tending to open the crack tip is a maximum. The angle of this direction, measured relative to the initial crack line direction, is designated as θ_o (see Fig. 7.1), where:

$$K_I \sin\theta_o + K_{II} \,(3\cos\theta_o - 1) = 0 \quad . \tag{7.2}$$

By using equation (7.1), K_I and K_{II} can be eliminated from equation (7.2) to give:

$$\sin\theta_o + (3\cos\theta_o - 1)\cot\beta = 0 \quad . \tag{7.3}$$

Equation (7.3) is valid provided β is non-zero ($\beta = 0$ gives a trivial solution for equation (7.2)). There are two solutions of θ_o for each given value of β ($0 < \beta < \pi/2$);

one is a positive value which is valid when the applied stress is compressive, and the other is negative, valid when the applied stress is tensile. Since equation (7.3) does not contain any elastic constants, this implies that the initial angle of crack growth is independent of material properties. It should be noted that equation (7.3) may also be obtained by equating the shear stress to be zero, since zero shear stress and maximum tangential stress necessarily occur at the same angle.

The maximum tangential stress criterion was verified experimentally by Williams and Ewing [85]. Maiti and Prasad [86, 87] used the finite element method to determine the crack path in a perspex sheet having either a central crack or an edge crack. In Fig. 7.2(a) Q_1 is the point within the crack tip zone at which the tangential stress is a maximum. QQ_1 therefore represents the direction of crack extension, and this extension occurs when the maximum tangential stress at Q_1 reaches a critical value. They predicted the crack path $QQ_1Q_2Q_3Q_4$ by tracing the locus of the point of maximum tangential stress for the stress field that was present just prior to the onset of crack growth. Excellent agreement with an experimentally determined crack path was observed.

This criterion is based on two basic hypotheses [88]:

1) the crack will spread in the radial direction along which the strain energy density is a minimum, and

2) the onset of fracture is determined when a critical value of the minimum strain energy density is reached.

Kipp and Sih [90] numerically employed the minimum strain energy density criterion to determine the crack path in a brittle material. In this case $QQ_1Q_2Q_3Q_4..$ in Fig. 7.2(a) is the locus of the minimum strain energy density predetermined by the entire stress field existing just prior to the onset of crack growth. Mau and Yang [91] determined the crack path by using a similar procedure to that of Kipp and Sih. In addition, they applied a step-by-step analysis to redistribute the stress field due to an infinitesimal crack extension. At each step, the crack was considered to extend in the direction of minimum strain energy density ($QQ_1Q_2Q_3Q_4..$ in Fig. 7.2(b)). There was negligible difference between these two procedures, with both showing good agreement with the experimentally determined crack path. Maiti and Prasad [86] have reported that although the minimum strain energy density criterion is useful for predicting the crack path for an internal crack, it is unsuitable for an edge crack problem.

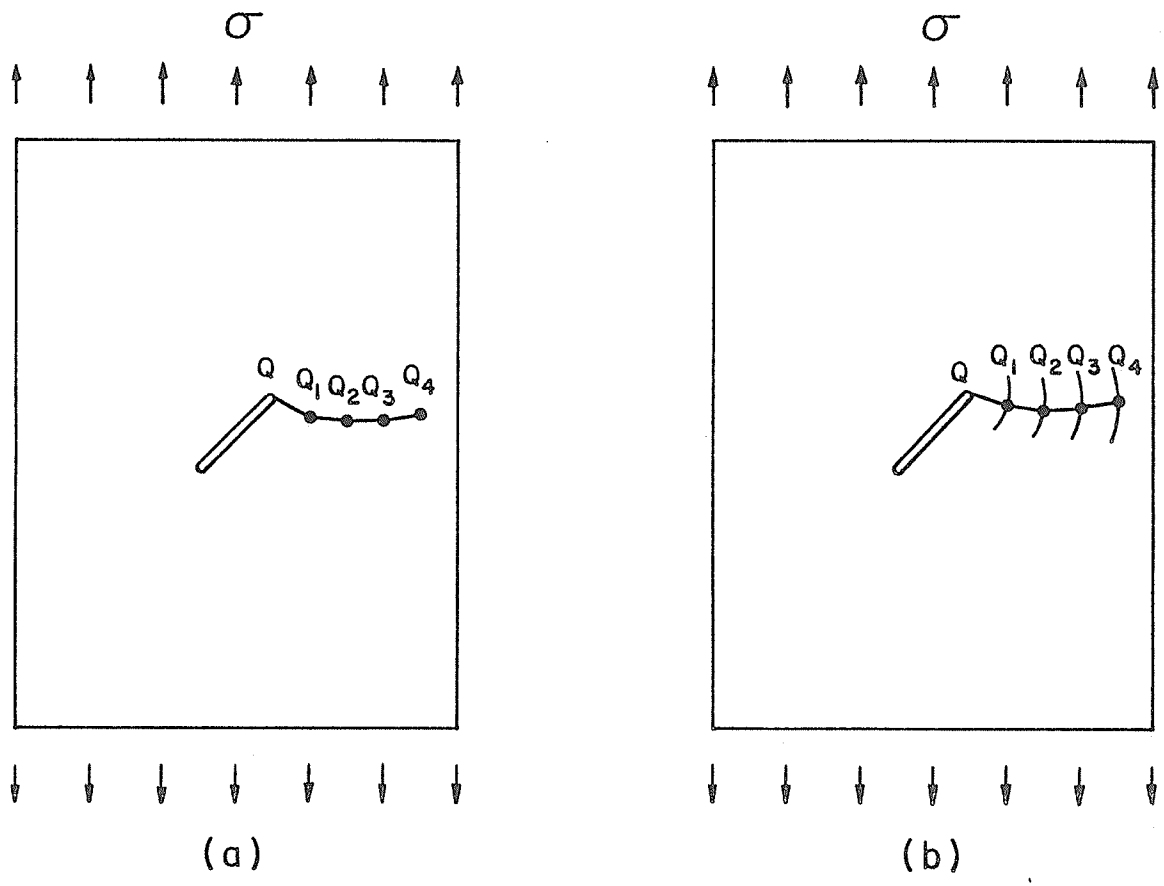

Fig. 7.2 Determination of the Crack Path.
(a) Analysis Based on Entire Field
(b) Step-by-Step Analysis

7.2.2 Minimum Strain Energy Density Criterion

In numerous publications [88 - 90] Sih has advocated the idea that the local strain energy density factor near the crack tip, S, should be the governing quantity for the fracture process. The strain energy density factor at the crack tip can be calculated by substituting the Williams-Irwin asymptotic stress field [2] into the standard formula for the strain energy density of an elastic solid, giving:

$$S = a_{11}K_I^2 + 2a_{12}K_IK_{II} + a_{22}K_{II}^2 \tag{7.4}$$

where

$$a_{11} = \frac{1}{16\mu}(1 + \cos\theta)(\kappa - \cos\theta)$$

$$a_{12} = \frac{\sin\theta}{16\mu}(2\cos\theta - (\kappa - 1)] \tag{7.5}$$

$$a_{22} = \frac{1}{16\mu}[(\kappa + 1)(1 - \cos\theta) + (1 + \cos\theta)(3\cos\theta - 1)]$$

μ = shear modulus

$\kappa = 3 - 4\nu$ (plane strain)

$= \frac{3 - \nu}{1 + \nu}$ (plane stress) .

Thus, S is a function of the angle θ through the coefficients a_{ij} and therefore gives a description of the local strain energy density for any radial ray intersecting the crack tip.

7.2.3 Maximum Energy Release Rate Criterion

Hussain et al [92], and Palaniswamy and Knauss [93] calculated the released strain energy assuming a small extension of the crack at various angles to the initial crack. In order to predict the direction of the crack propagation, it is then hypothesized that:

1) the crack will propagate in the radial direction along which the elastic energy release per unit crack extension is a maximum, and
2) the onset of fracture is determined by some critical value of the energy release rate.

This criterion leads to results identical with those obtained by using the maximum tangential stress criterion, since the direction in which the maximum tangential stress occurs is also the direction causing the maximum energy release rate. As well, the criterion depends on a global energy change rather than the near-tip field values required for the two previous criteria.

Hellen [94] applied this criterion in a step-by-step procedure to study the problem of fatigue crack growth with the aid of the finite element method. In this case $QQ_1Q_2Q_3Q_4..$ in Fig. 7.2(b) is the locus of the maximum energy release rate, computed by assuming small extensions of the crack. The numerically predicted crack path shows good

agreement with the experimental one.

7.3 Prediction of The Crack Path in Ductile Materials

As described in the previous section, various methods for predicting the crack path in brittle materials under mixed mode loading conditions have been proposed. In order to predict the crack path in ductile materials, a minimum effective strain criterion is proposed. This criterion is based on two hypotheses, which are consistent with those of the previously mentioned criteria:

(1) the crack will propagate in the radial direction along which the effective strain obtains a minimum value, and

(2) the onset of fracture is determined when a critical value of the minimum effective strain is reached.

Hypothesis (1) is justified by considering that the crack will propagate in the direction of least distortion energy (plastic work) [89], and that $\bar{\varepsilon}$ is proportional to this distortion energy. Hypothesis (2) is equivalent to the rupture strain concept used in the mode I fracture analysis in Chapter 6. With these two hypotheses, $\bar{\varepsilon}$ can be used to predict not only the load at which crack growth occurs, but also the direction of crack growth.

The minimum strain energy density and maximum tangential stress criteria were also considered for predicting the crack path in ductile material. The strain energy density in the elastic-plastic range was calculated as:

$$w = \int_{o}^{\varepsilon} \sigma_{ij} \, d\varepsilon_{ij} \quad . \tag{7.7}$$

although included elastic-plastic work, elastic strain energy was a univalued function of the total work. The maximum energy release rate criterion has, however, not been implemented since it requires excessive computational costs to calculate the released strain energy for every angle of a given small crack extension.

Finite element investigations were performed to test the various proposed theories. The mixed mode experimental specimen, with a 45° inclined crack as described in Chapter 5, was modelled using the finite element mesh illustrated in Fig. 7.3(a). The details of the refined mesh surrounding the crack tip are given in Fig. 7.3(b). The radial lines emanating from the crack tip are uniformly spaced at 10 degree intervals in the θ-coordinate. Since the methods for determining the crack path require the distribution of field values at equal distances from the crack tip, the finite element mesh was completed by imposing concentric circular lines around the crack tip. Conditions of line symmetry

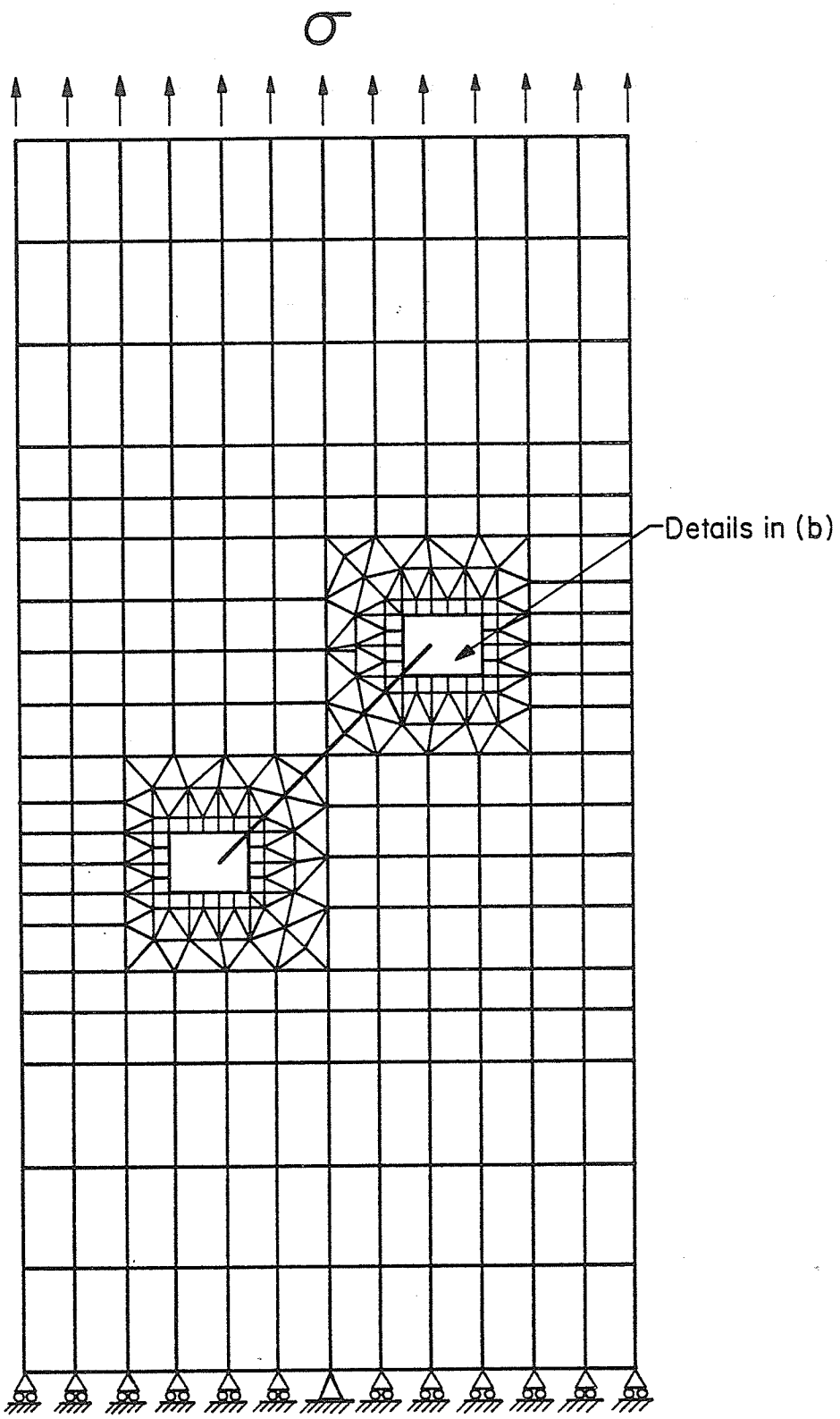

Fig. 7.3 Finite Element Model: Mixed Mode
(a) Overall View

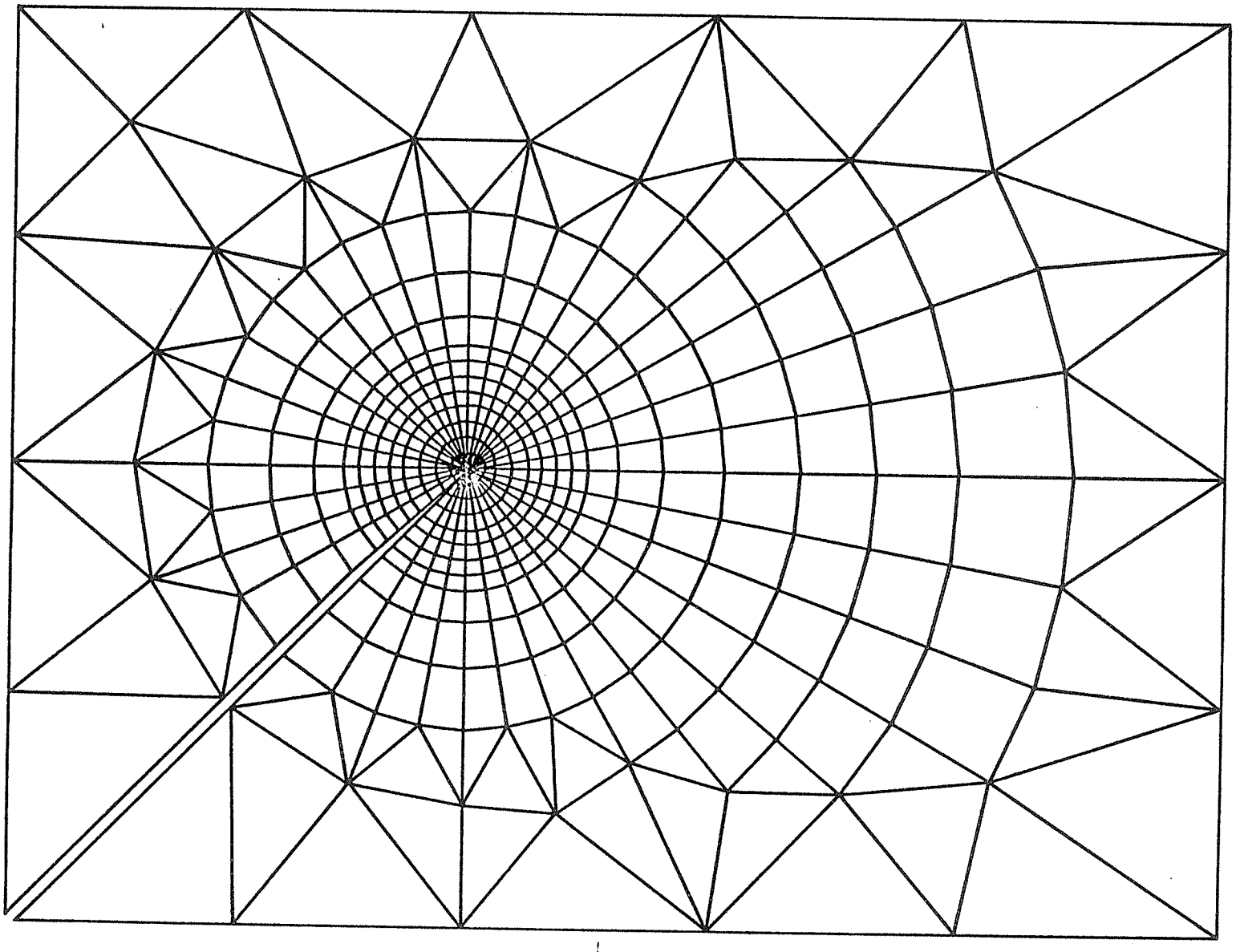

Fig. 7.3 Finite Element Model: Mixed Mode.
(b) Crack Tip Region

are non-existent in the mixed mode case, and accordingly it was necessary to model the entire specimen.

Since the effect on the crack path of the stress redistribution due to crack growth has been found to be insignificant [92], this uneconomical step-by-step procedure to readjust the crack path was not adopted in this analysis. That is, it was assumed the field conditions at the onset of crack growth pre-determined the entire crack path through the specimen.

Fig. 7.4 shows the variation of the effective strain with respect to the angle θ at a few selected radii from the crack tip at the onset of crack growth. The crack path was subsequently determined by tracing the locus of the minimum value of each curve.

A similar procedure was performed using the previously mentioned criteria. Crack paths were determined by tracing the loci of the maximum values of the tangential stress distribution curves (Fig. 7.5); the zero values of the shear stress distribution curves (Fig. 7.6); and the maximum values of the work (performed on an element per unit volume) distribution curves (Fig. 7.7).

Fig. 7.8 illustrates the numerically predicted crack paths together with the experimentally determined paths

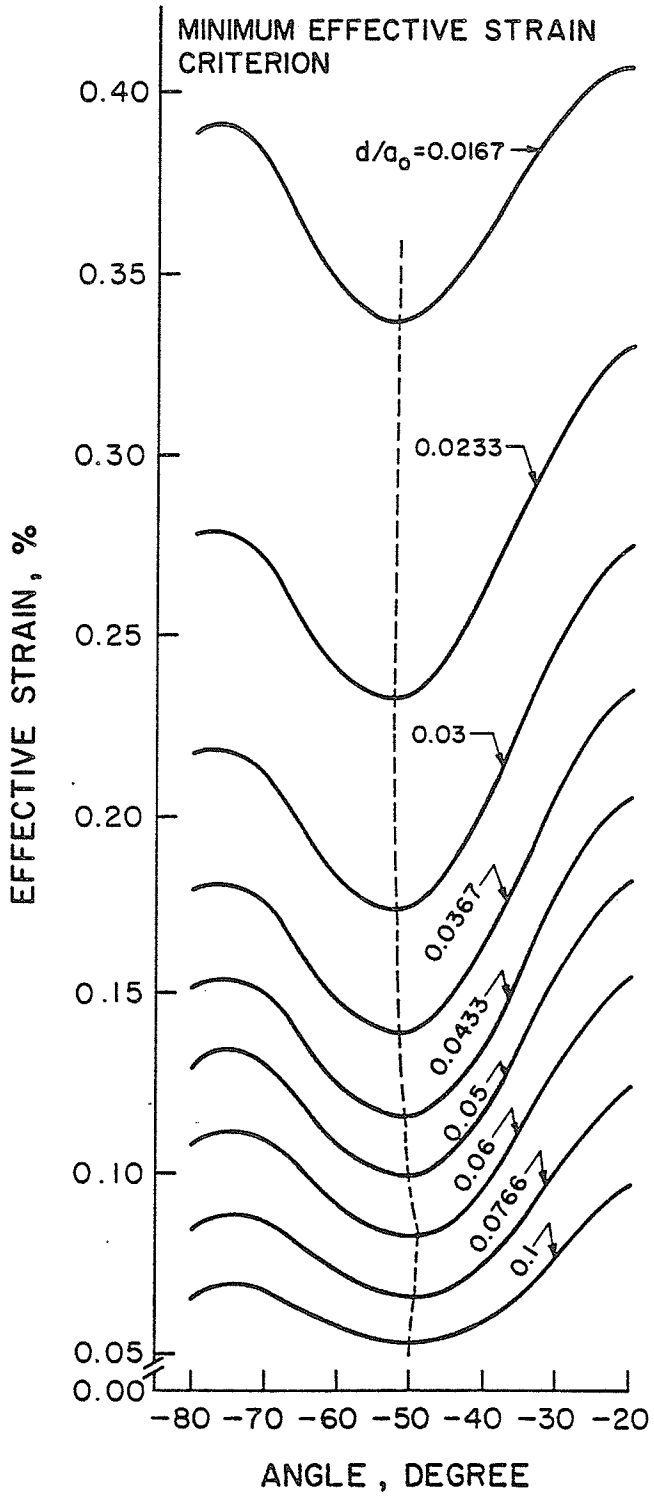

Fig. 7.4 Angular Variation of Effective Strain

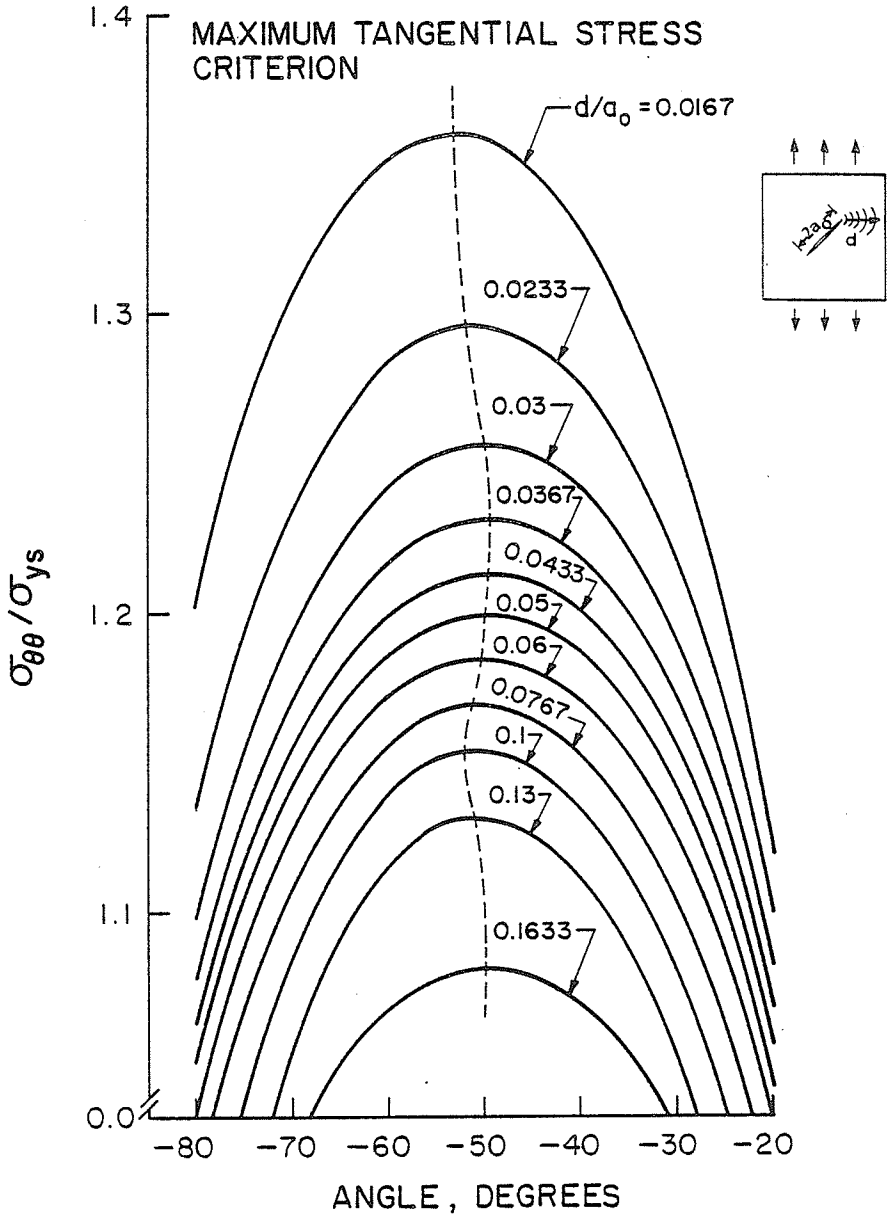

FIGURE 7.5

ANGULAR VARIATION OF TANGENTIAL STRESS

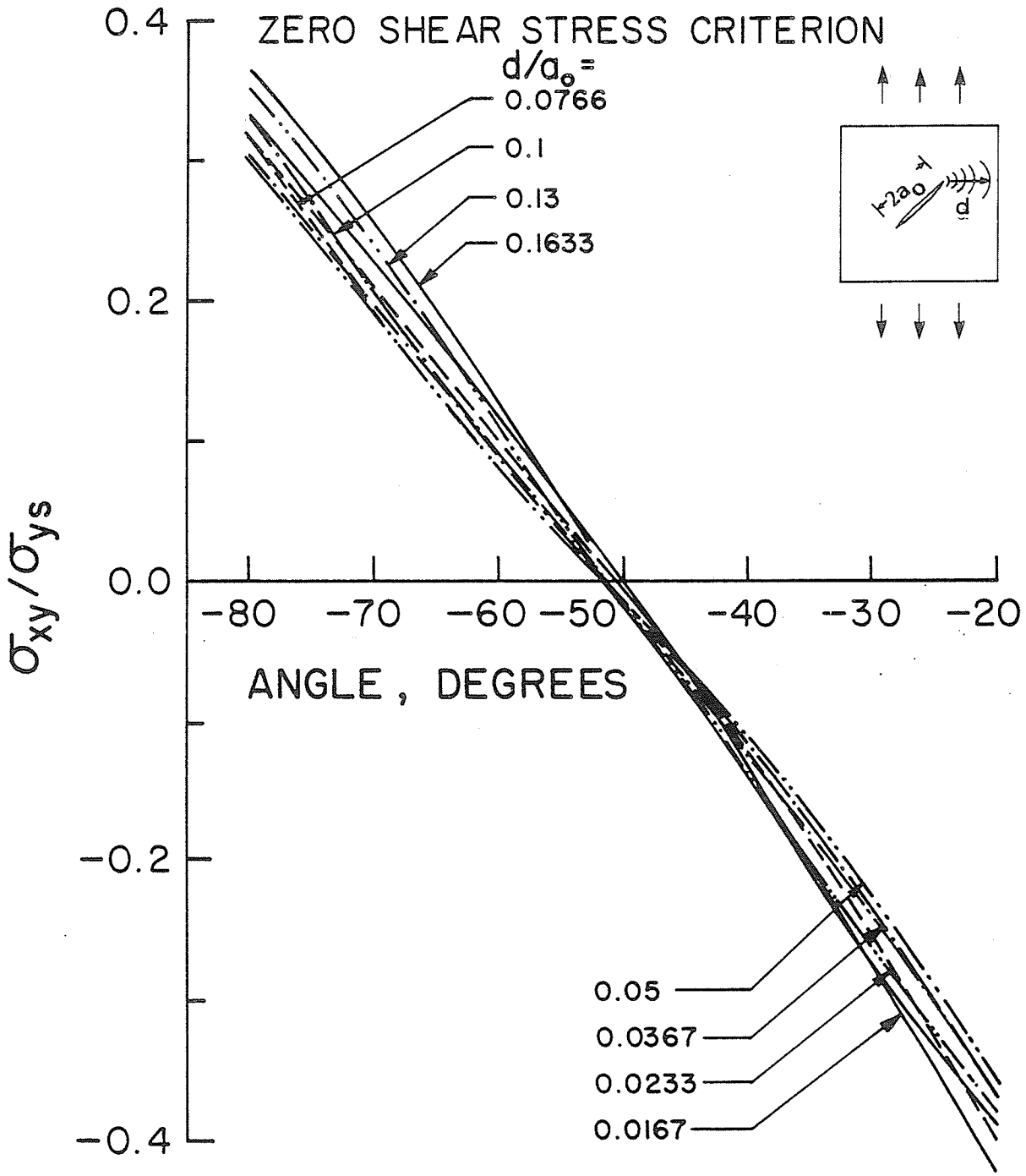

FIGURE 7.6

ANGULAR VARIATION OF SHEAR STRESS

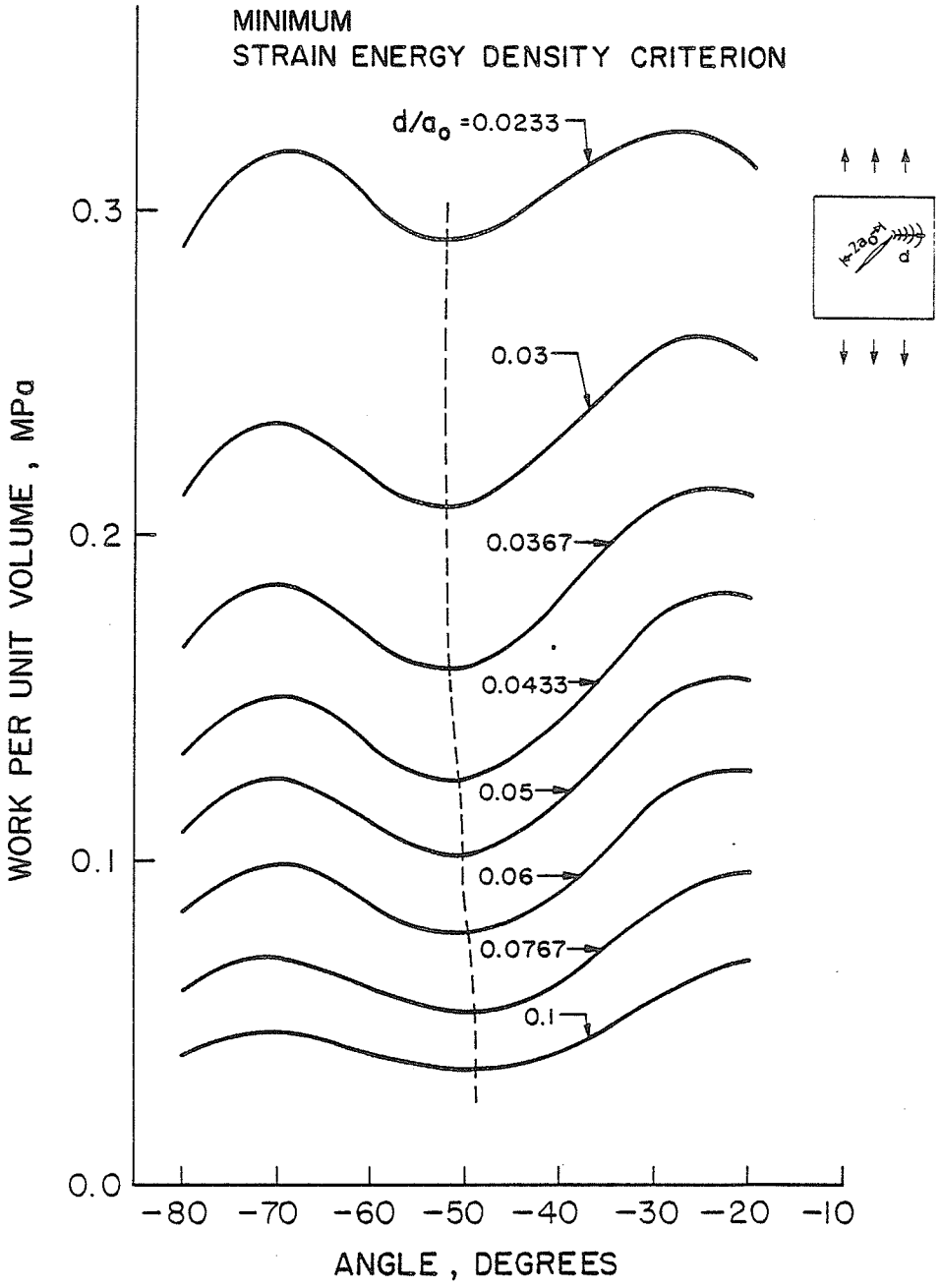

FIGURE 7.7

ANGULAR VARIATION OF STRAIN ENERGY DENSITY

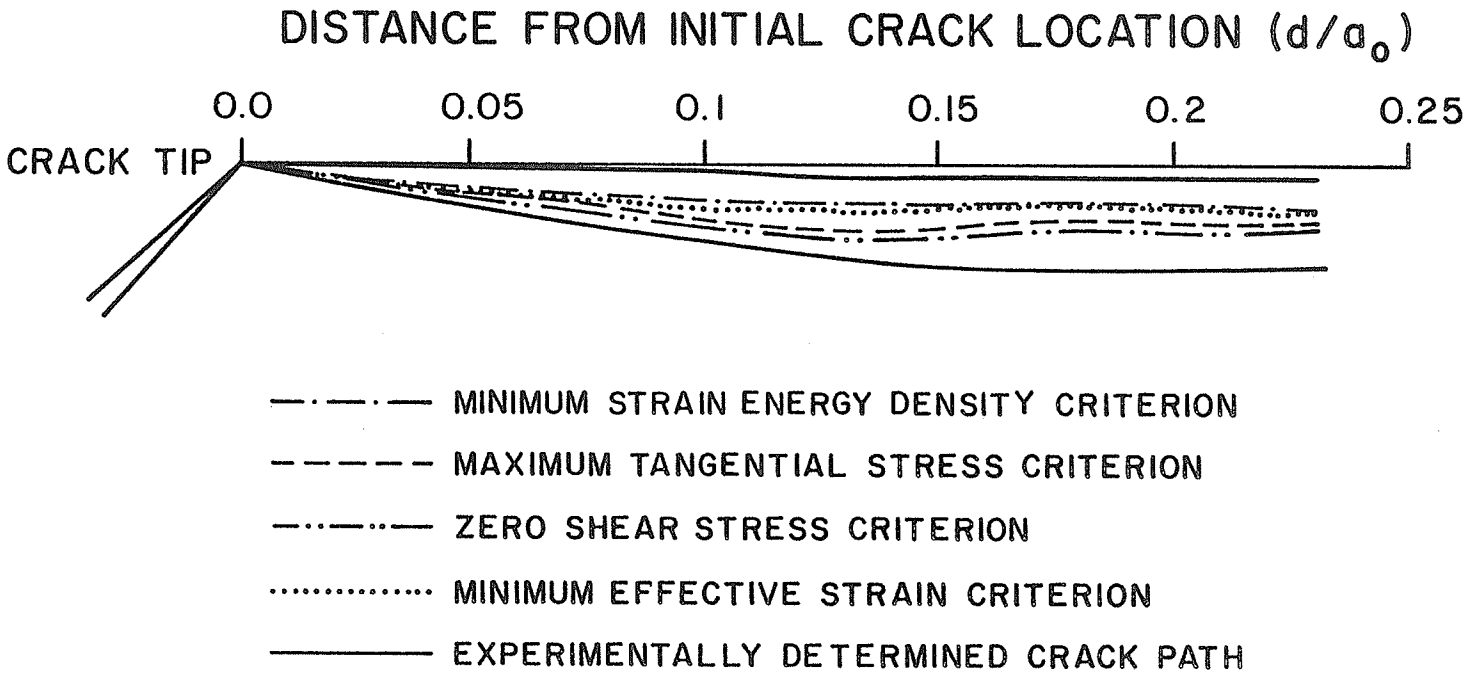

Fig. 7.8 Numerically Determined Crack Path.

(see Fig. 5.6). Two experimental curves appear since the crack paths on the front and back faces of the specimen were different due to the fracture surface angling through the specimen thickness. The numerically predicted crack paths lie between the upper and lower bounds of the experimental crack paths.

The maximum tangential stress criterion, equation (7.2), yields a crack initiation angle of $\theta_o = -53°$, while the minimum strain energy density criterion, equation (7.4), predicts $\theta_o = -51°$. Note that the negative sign implies that the crack propagation is in a direction which is clockwise, measured relative to the initial crack line direction (Fig. 7.1). These equations are strictly valid only for the initiation angle of brittle fracture. However, the trend that θ_o from the maximum tangential stress criterion is greater than θ_o from the minimum strain energy density criterion is evident throughout the predicted crack path even for this ductile fracture. The crack path determined by the minimum effective strain criterion also provides an accurate prediction of the crack path.

In summary, all of the above mentioned numerical methods for predicting the crack path produced similar results. However, the zero shear stress criterion is the simplest to

employ. This method requires only the determination of the angle of zero shear stress, which is a more accurate interpolation procedure than that required to estimate the peak positions of the other curves.

7.4 Prediction of Stable Crack Growth

Once the crack path was pre-determined, a finite element analysis was performed to predict the stable crack growth behavior of the mixed mode specimen. Breakable elements were arranged along the pre-determined crack path, as shown in Fig. 7.9. A rupture strain of 11.5%, which was obtained from the mode I analysis, was adopted here as the fracture criterion.

Fig. 7.10 presents the numerically computed applied stress vs stable crack growth curve for the mixed mode specimen, along with the experimentally obtained curve. This figure shows that crack initiation occurred at an applied stress of 20.6 ksi (142.0 MPa), far higher than the stress of 13.8 ksi (95.2 MPa) observed from the mode I analysis. This expected result is due to the fact that the component of the applied stress acting to open the crack faces is only a fraction of the total applied stress. Once the crack growth had initiated, the mixed mode specimen displayed a higher rate of crack growth with respect to the

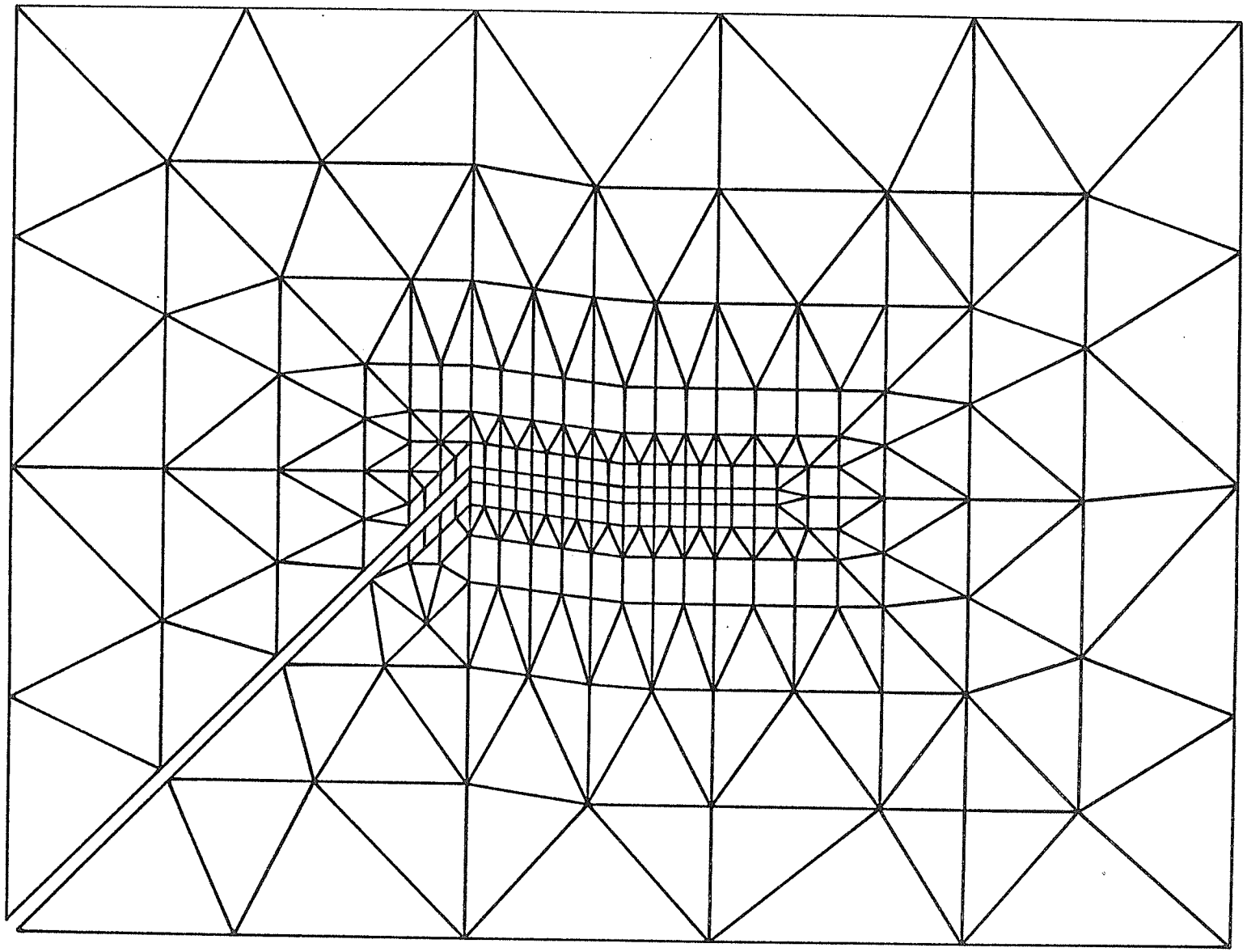

Fig. 7.9 Finite Element Model at the Mixed Mode Crack Tip.

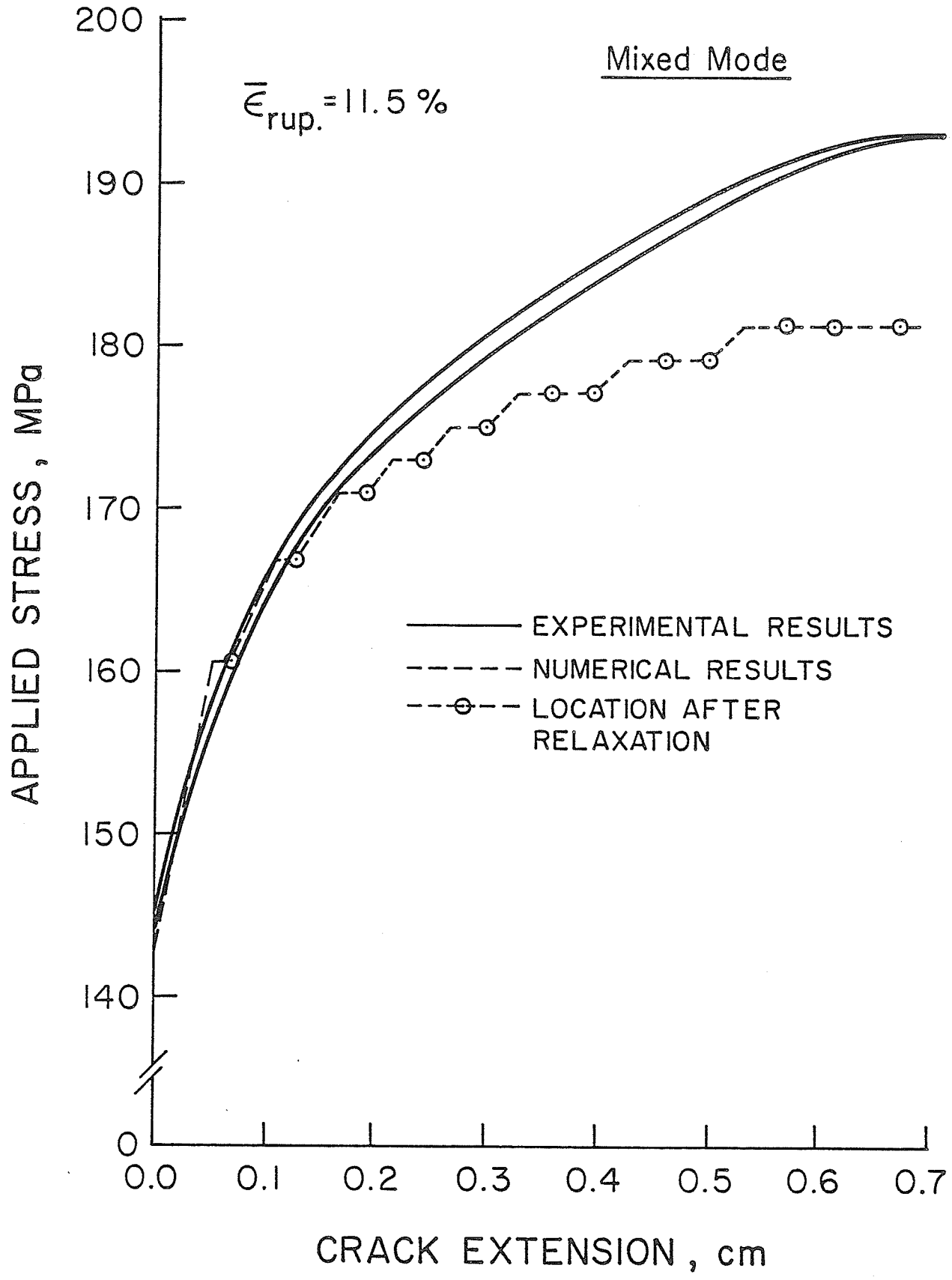

Fig. 7.10 Applied Stress vs Stable Crack Growth Curve: Mixed Mode.

applied stress than did the mode I specimen. The reason for this higher crack growth rate will be discussed in the next section.

The first six breakable elements were broken by load increments in conjunction with the nodal force relaxation. However, the seventh element was broken solely as a consequence of the nodal force relaxation of the sixth element, that is without any further applied load increment. Additional load increments subsequently broke the eighth element, while the ninth element again was broken solely as a consequence of the nodal force relaxation of the eighth element. A chain reaction of crack extensions was then initiated when the crack growth due to the nodal force relaxation exceeded the right-edge nodal point of each subsequent breakable element, resulting in unstable crack growth. Thus, at the instability load of 26.3 ksi (181.3 MPa) $\bar{\varepsilon}_{ext.}$ was always greater than $\bar{\varepsilon}_{rup.}$.

Using $\bar{\varepsilon}_{rup.}$ value from the mode I analysis, the finite element analysis for the mixed mode specimen predicted the applied stress at crack initiation within 1% of the experimental results and the applied stress at instability within 6%. The applied stress at the onset of unstable fracture was about 23% higher than that at the onset of stable crack

growth, with the total amount of stable crack growth being roughly 10% of the initial crack length. These results imply that the mixed mode specimen has a slightly smaller safety margin than the mode I specimen in terms of the 'leak before break' concept. However, the mixed mode specimen sustained much higher applied stress values and exhibited longer stable crack growth.

7.5 Variation of Strain and Stress Distributions

7.5.1 Strain Distribution

Fig. 7.11 shows both the experimentally and numerically obtained variations of strain at the eight strain gauge locations on the mixed mode specimen (see Fig. 5.3). As was observed with the mode I specimen, the two sets of results correlate quite well. Strain gauges nos. 7 and 8 exhibited some discrepancies (less than 5%) mainly due to the slight difference in the crack lengths used in the numerical analysis and the experimental measurement.

Fig. 7.12 shows the effective strain distribution ahead of the growing crack tip in the mixed mode specimen, before and after the nodal force relaxation of each breakable element. Because of the less severe strain concentration at the crack tip, the mixed mode specimen displays a flatter strain profile than the mode I specimen and also requires a

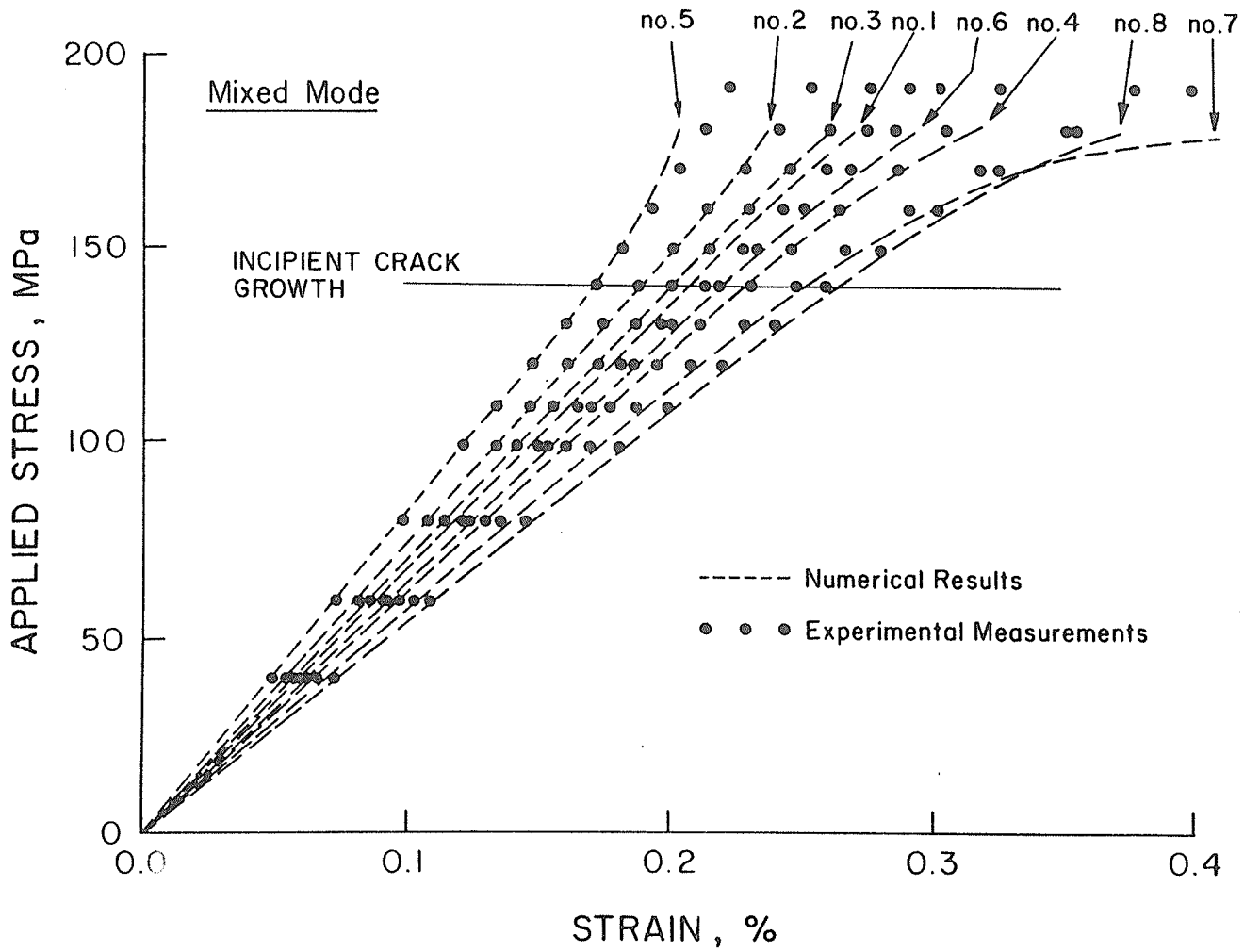

FIGURE 7.11

STRAIN DISTRIBUTION AT THE EIGHT LOCATIONS: MIXED MODE.

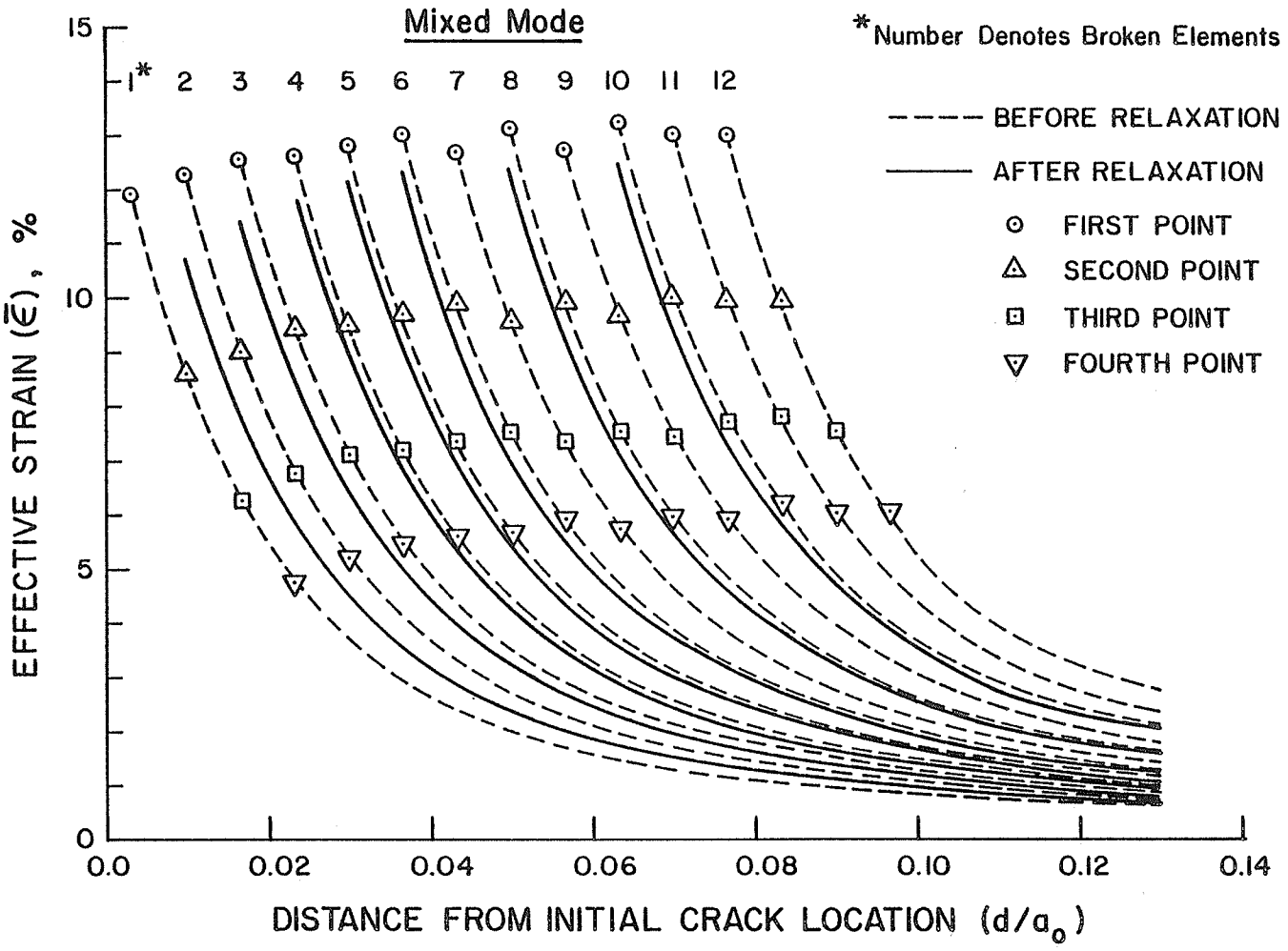

Fig. 7.12 Effective Strain Distribution Ahead of the Crack Tip: Mixed Mode.

higher applied stress level to reach the fracture criterion, $\bar{\varepsilon}_{rup.}$ than does the mode I specimen. Because of these two effects the second breakable element of the mixed mode specimen attained a higher strain value prior to the fracture of the first element than did the second breakable element of the mode I specimen. Thus, a smaller load increment than was necessary for the mode I specimen was required for the second breakable element of the mixed mode specimen to reach the fracture criterion. This would account for the higher crack growth rate with respect to applied stress for the mixed mode specimen following crack initiation than that observed for the mode I specimen.

7.5.2 Stress Distribution

The effective stress distribution ahead of the growing crack tip for the mixed mode case at various stages of crack growth is presented in Fig. 7.13. As observed in the mode I case, the effective stress distribution ahead of the crack tip drops after application of the nodal force relaxation. However, the magnitude of this drop is less than that for the mode I case. This may be a further explanation of the smaller margin of safety for the mixed mode case following crack initiation.

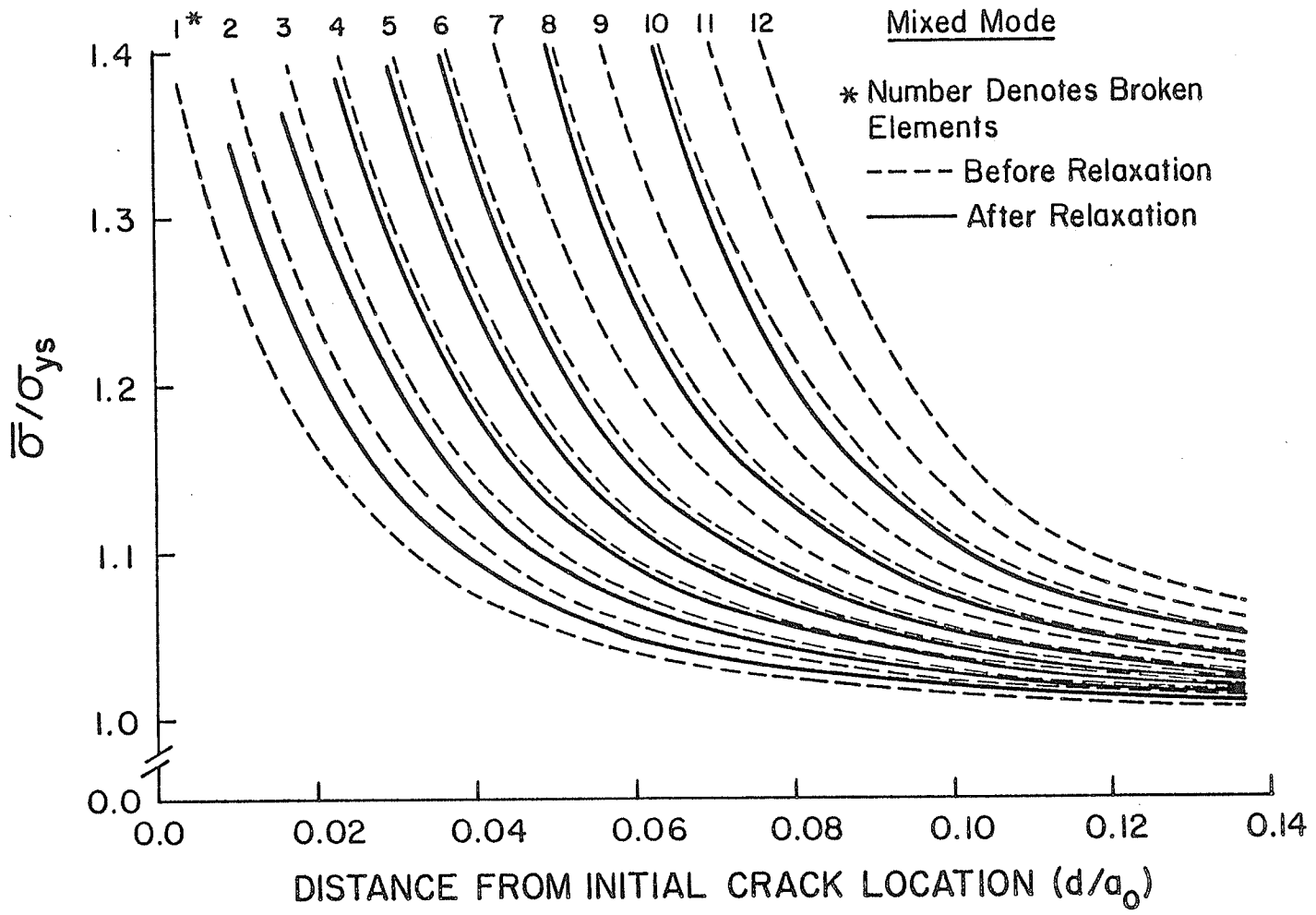

Fig. 7.13 Effective Stress Distribution Ahead of the Crack Tip: Mixed Mode.

Figs. 7.14 through 7.16 present the stress histories for the three selected elements A, B and C located at the same positions on the specimen (relative to the crack tip) as in the mode I case (Fig. 6.1(b)). These figures show that the material adjacent to the crack path experiences a similar stress history as that for the mode I case. The σ_{yy} stress component is the dominating stress component ahead of the crack tip, and diminishes rapidly after the crack tip has passed. This behavior indicates that the crack growth simulation was executed properly for the mixed mode analysis.

The σ_{xx} stress component is roughly one-half of σ_{yy} ahead of the crack tip, and becomes negative once the crack tip passes.

The σ_{xy} stress component also displays similar behaviour to that observed for the mode I analysis. However, element A displayed high shear stress after the crack tip had passed, likely due to the geometrical influence of the dog-leg.

7.6 Variation of Crack Tip Parameters

The profiles of the crack face in the elastic regime, at the onset of crack growth, and immediately before and after the nodal force relaxation of the first breakable

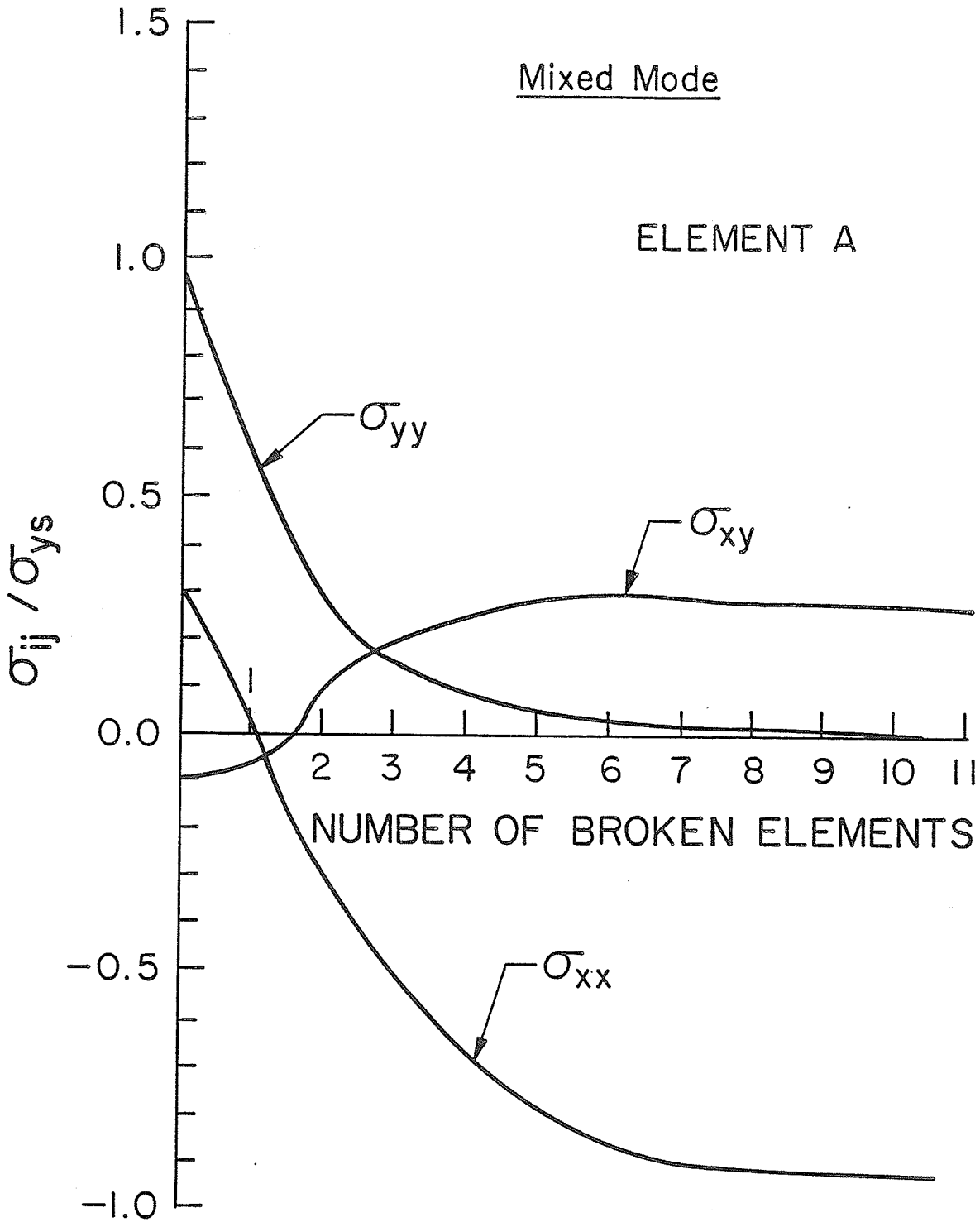

Fig. 7.14 Stress History of Element A: Mixed Mode.

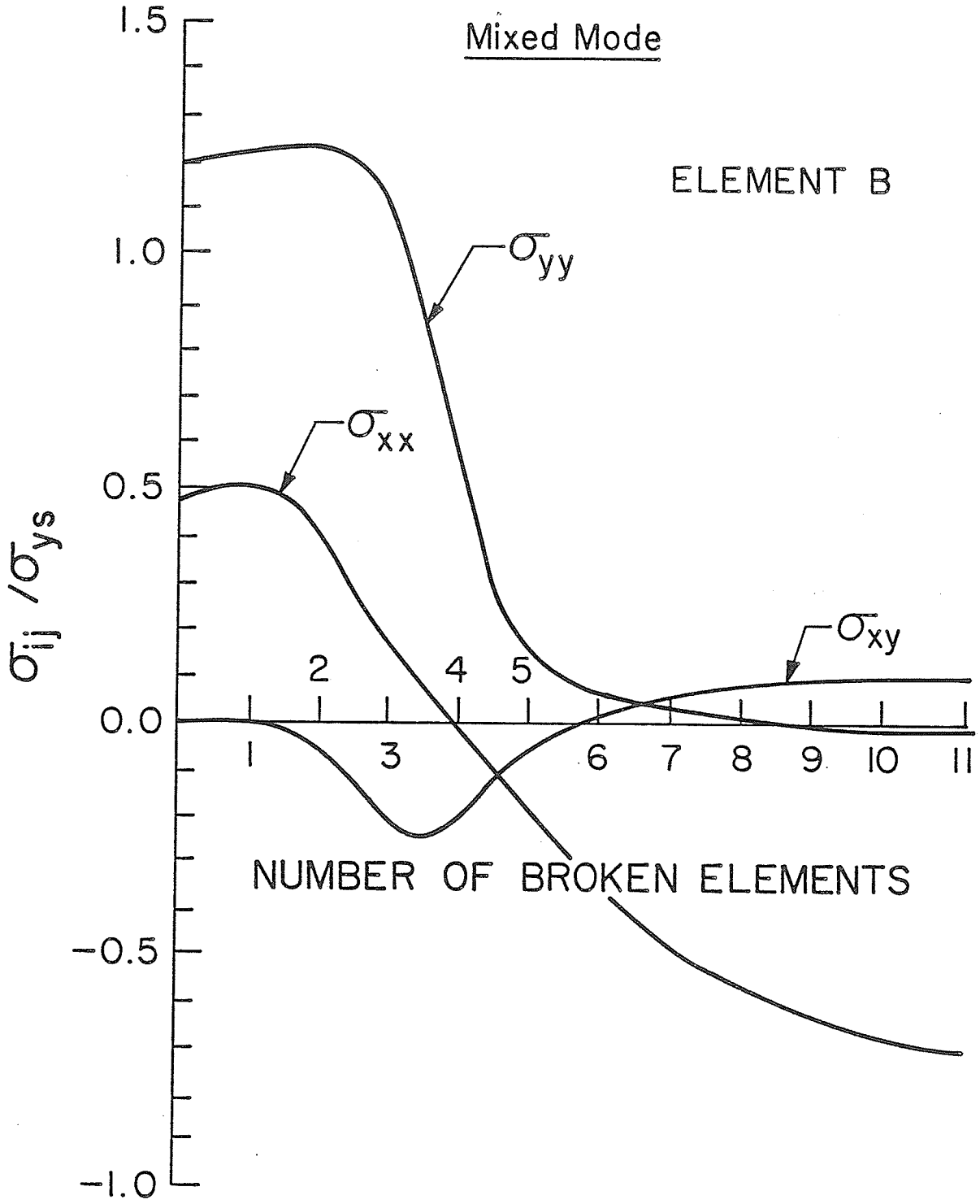

Fig. 7.15 Stress History of Element B: Mixed Mode.

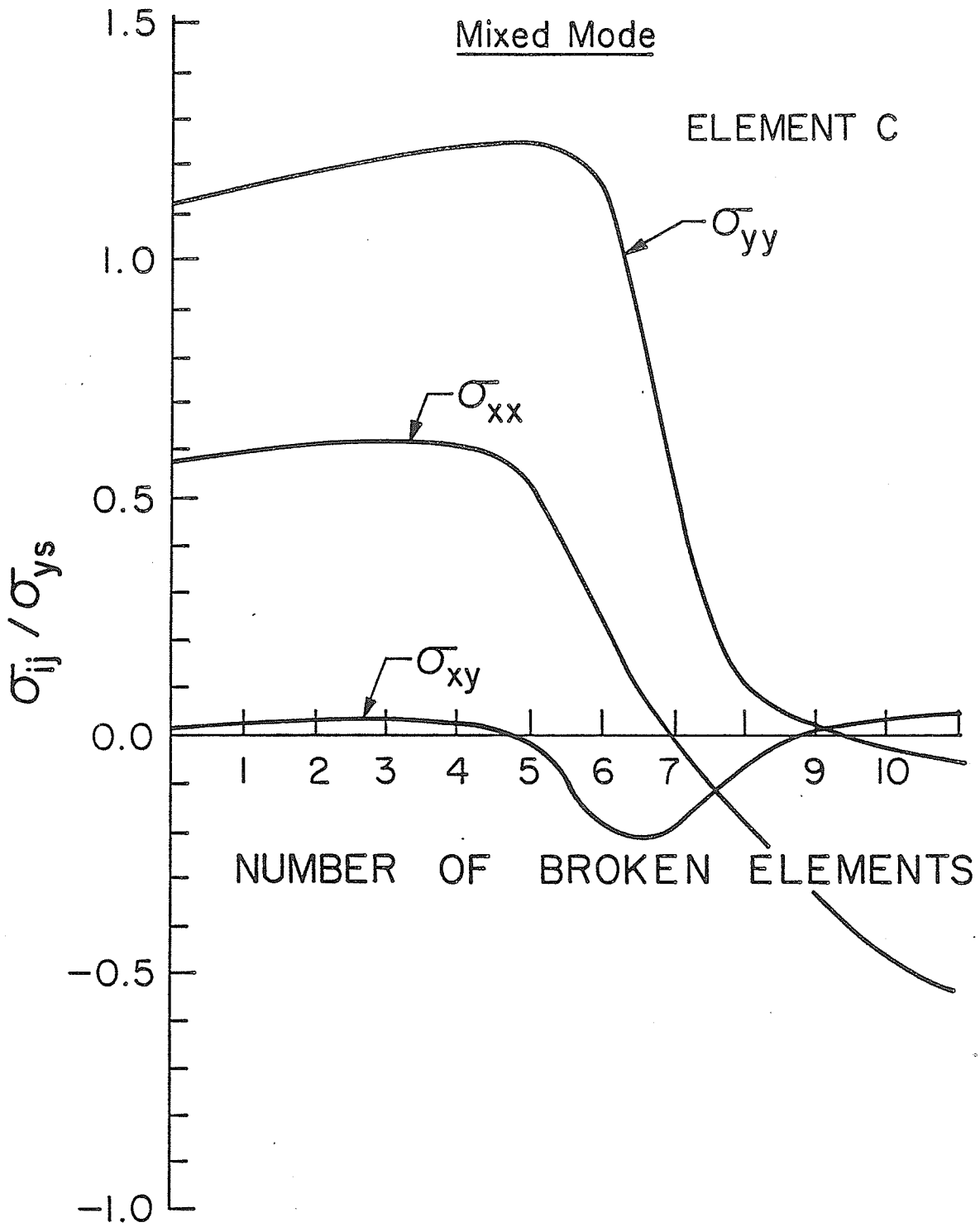

Fig. 7.16 Stress History of Element C: Mixed Mode.

element are shown in Fig. 7.17. The profile of the crack face in this figure is defined as the distance between the upper and lower crack faces. This figure illustrates that the mixed mode crack face has a more blunted profile than has the mode I crack face.

Fig. 7.18 presents the profiles of the mixed mode crack faces at various stages of crack growth. The slope discontinuity of the crack face profiles at the initial crack tip location arises due to the singularity associated with the sudden change in crack growth direction at the corner of the dog-leg. Although the initial crack face exhibits a more blunted profile in the mixed mode case than the mode I case, the subsequent crack growth produced profiles in the extended crack portion which displayed a similar shape for both cases.

The COD, COA and CTOA crack tip parameters are evaluated according to the same definitions used in the mode I analysis.

Fig. 7.19 presents the variation of the numerically computed COD with crack extension for the mixed mode specimen. This figure shows that the COD for the mixed mode specimen increases consistently as the crack extends, attaining a value slightly less than that for the mode I specimen. Obviously this is due to the less severe stress concentration

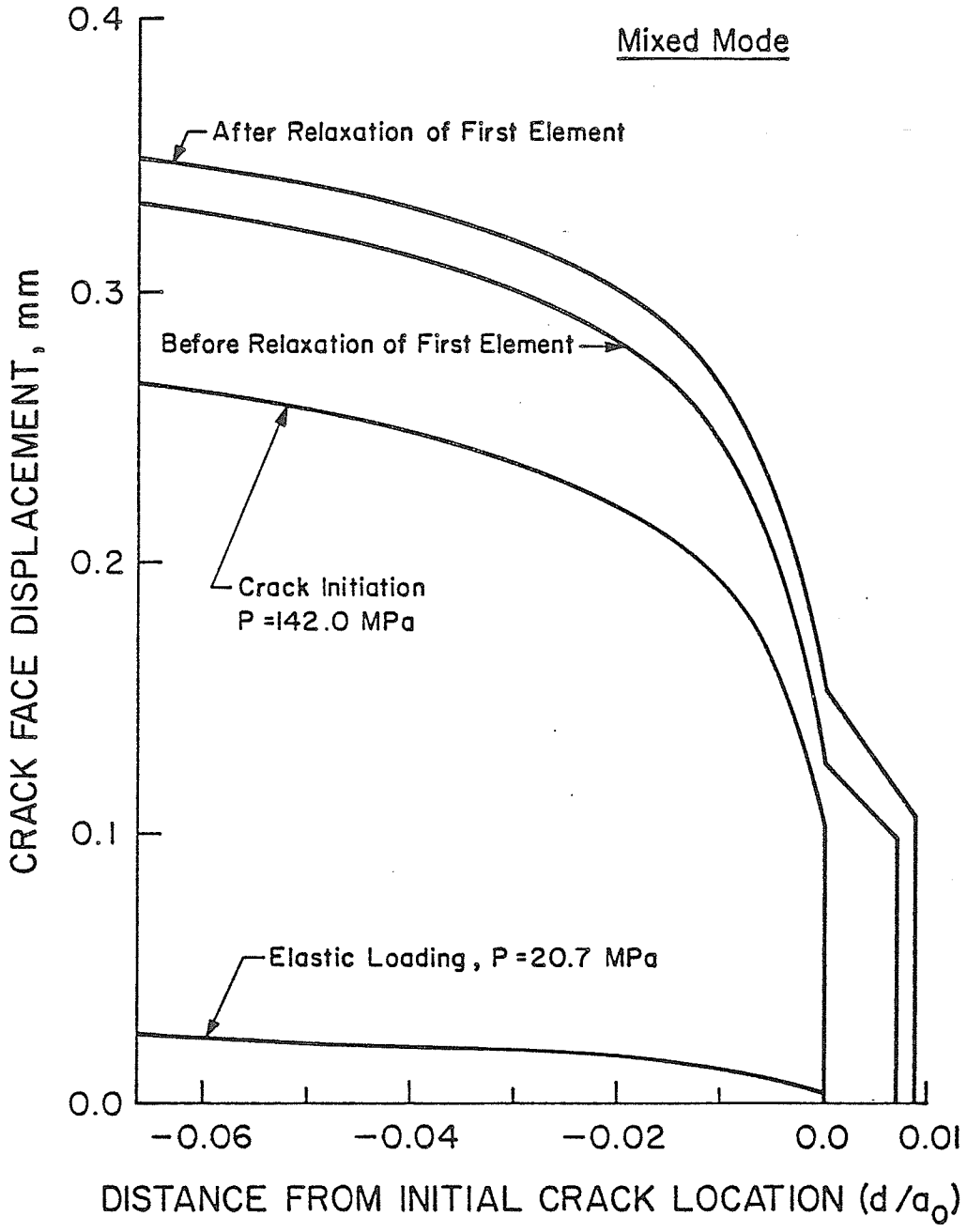

Fig. 7.17 Crack Face Profile (Stationary): Mixed Mode.

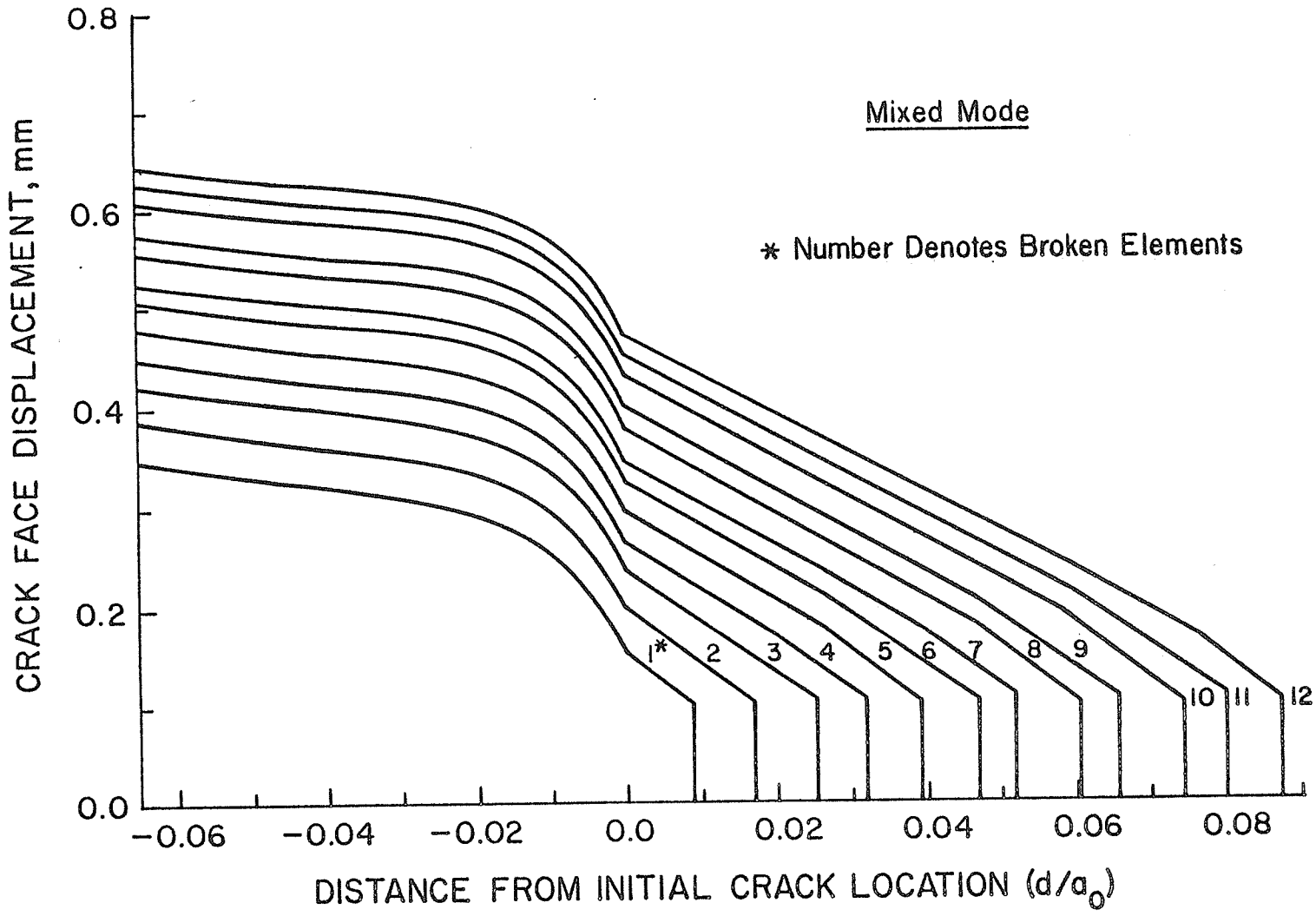

Fig. 7.18 Crack Face Profile (Growing Crack): Mixed Mode.

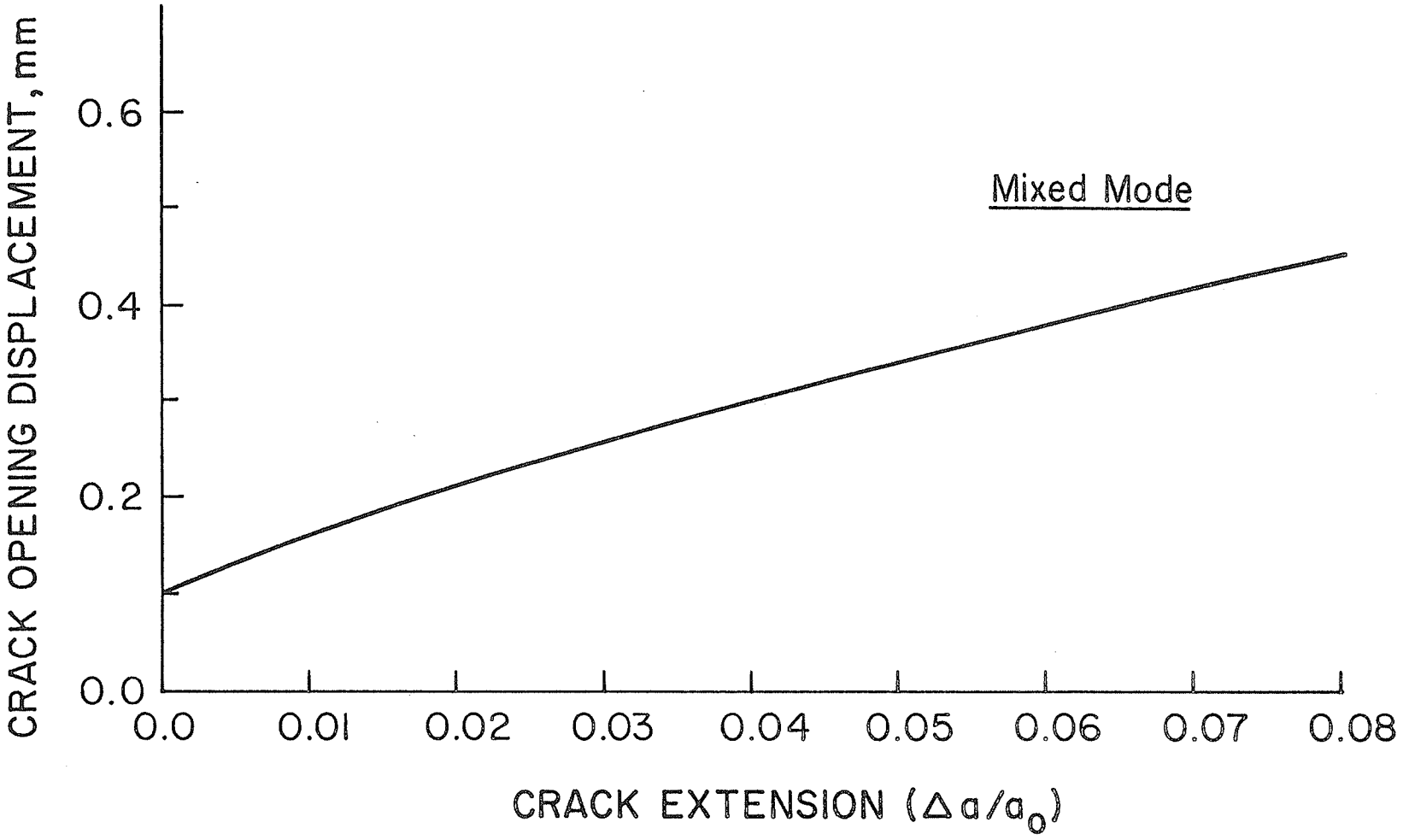

Fig. 7.19 COD vs Crack Extension: Mixed Mode.

at the mixed mode crack tip.

The variations of COA and CTOA with crack extension are shown in Fig. 7.20. As observed in the mode I case, the COA decreases consistently with crack growth. After a small amount of crack extension ($\Delta a/a_o$ = 0.025) the CTOA levels off, and remains relatively constant at approximately 0.073 radians during the subsequent crack growth. This value is roughly 10% lower than that observed in the mode I situation.

The variation of the nodal reaction force, F, of the crack tip element is shown in Fig. 7.21. This figure shows that F attains a value of about 5.2 Newtons, the same as in the mode I case.

From these observations on the various crack tip parameters, the CTOA and F show promising signs for use as fracture criteria. However, the F value appears to be more independent of the type of fracture mode.

7.7 Development of the Plastic Zone

The boundary of the numerically computed plastic zone at various stages of crack growth in the mixed mode specimen is plotted in Fig. 7.22. As observed for the mode I

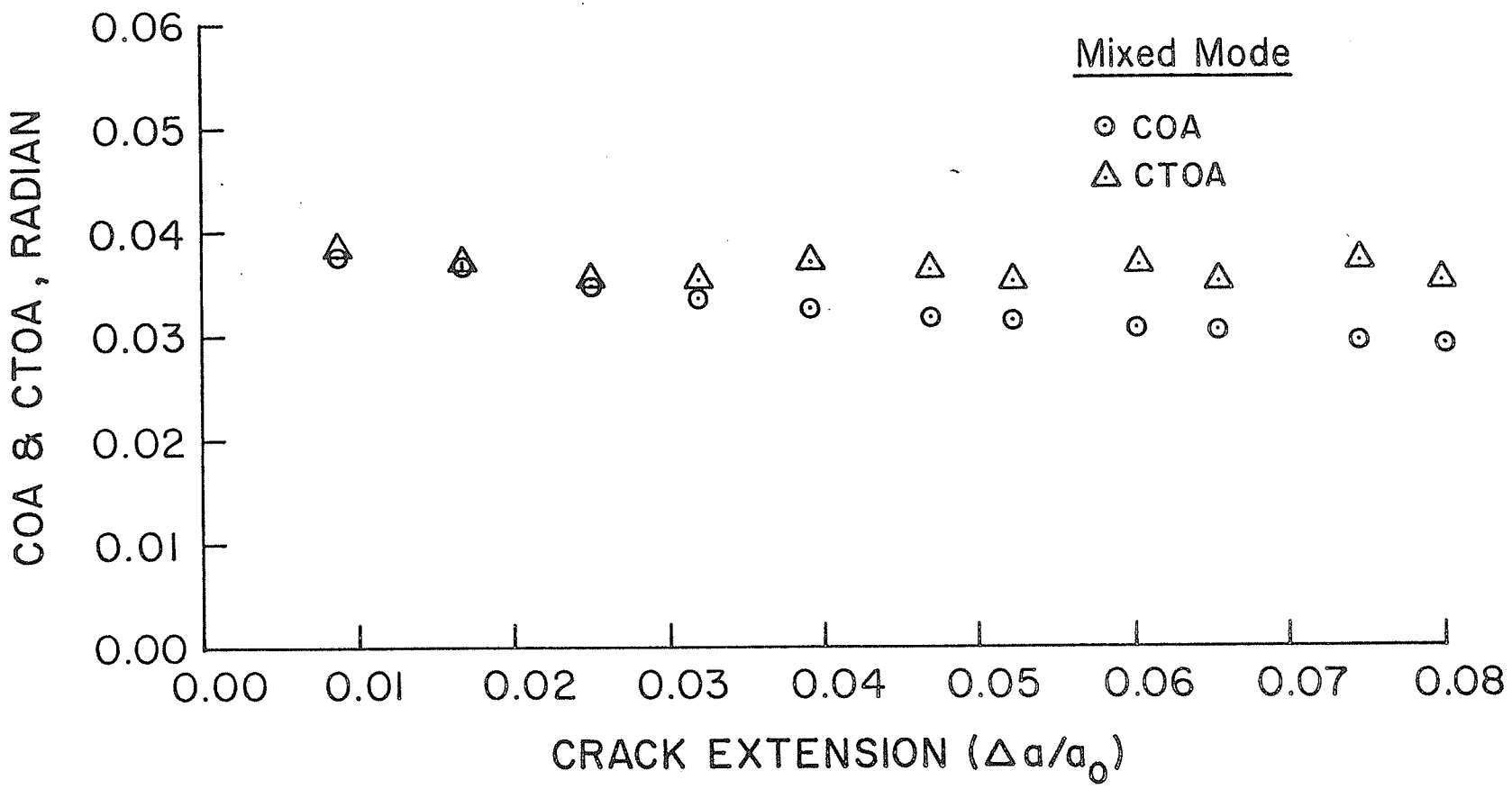

Fig. 7.20 COA, CTOA vs Crack Extension: Mixed Mode.

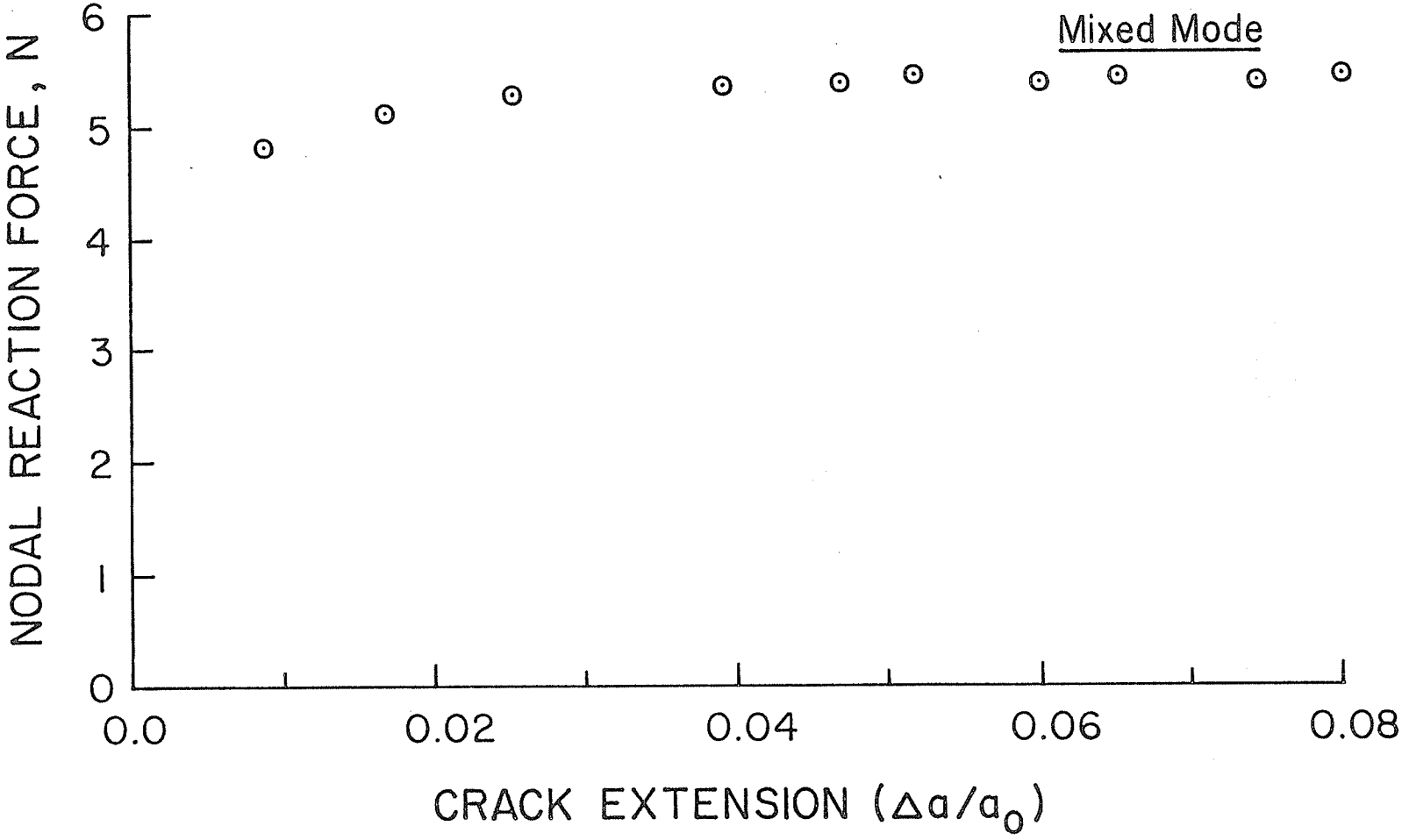

Fig. 7.21 Nodal Reaction Force vs Crack Extension: Mixed Mode.

case, the plastic zone boundary translates as the crack extends, with the most prominent direction of development occurring at $\theta \approx 0°$. Due to the influence of the inclined crack configuration, the upper half of the plastic zone was larger than the lower half of the plastic zone.

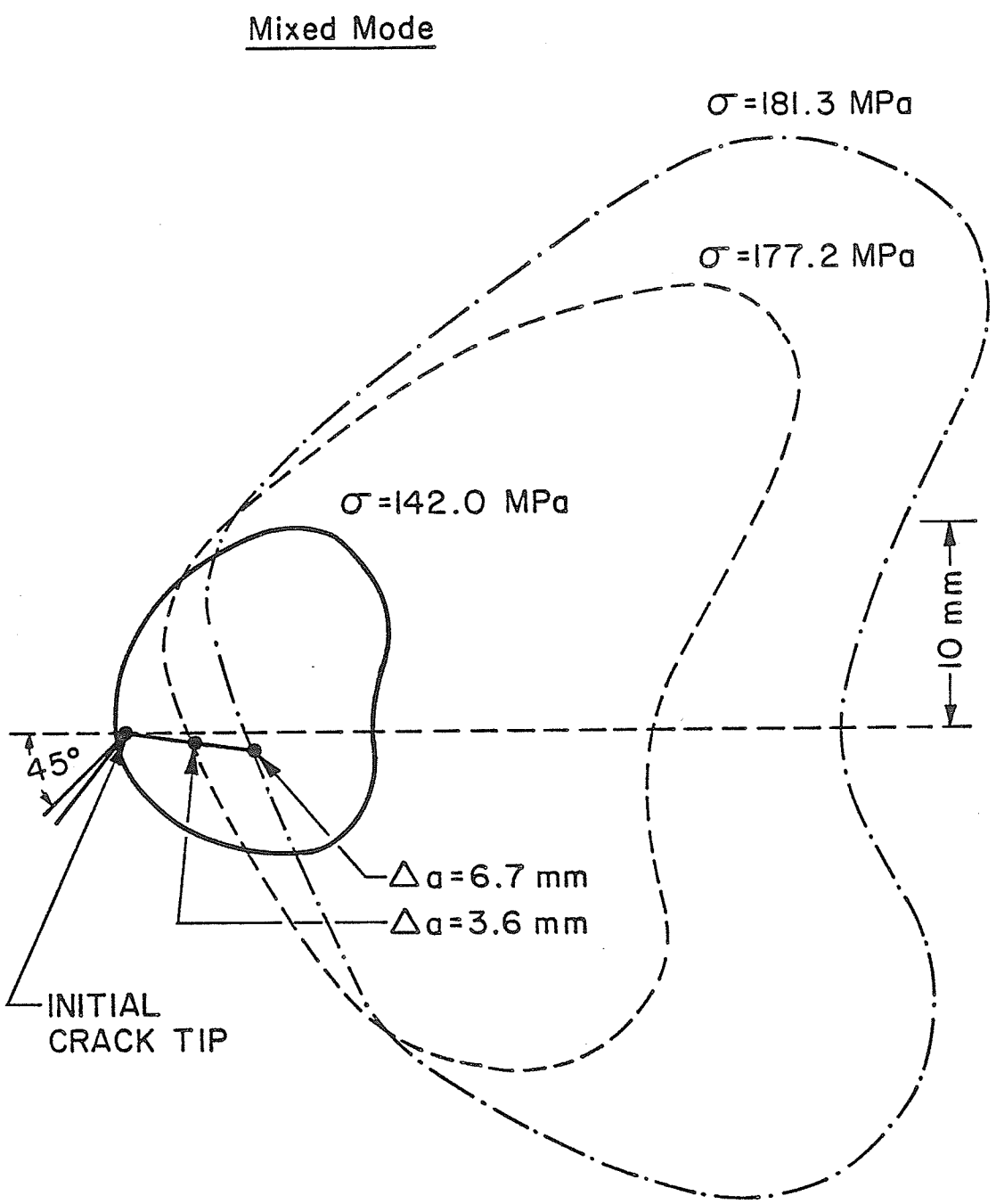

Fig. 7.22 Development of the Plastic Zone: Mixed Mode.

CHAPTER 8

CONCLUSIONS AND RECOMMENDATIONS

8.1 Conclusions

An experimental and elastic-plastic finite element investigation has been conducted to analyze stable crack growth in a center-cracked specimen subjected to monotonically increasing loads. An improved breakable element concept coupled with a nodal force relaxation technique was used to simulate the crack growth process. Although nine different requirements including geometry and computer model independence have been identified, a universally acceptable criterion for elastic-plastic fracture remains open to discussion. The present investigation has demonstrated that the effective strain value can be used not only as a fracture criterion for the mode I case but also as a direction criterion for the mixed mode case.

As shown in Figs. 6.3 and 7.10, the numerical and experimental results were in good agreement for both the mode I and mixed mode cases. Unstable fracture was deemed to occur in this analysis when a chain reaction in the crack extension process was initiated without further external load increments. The finite element results also elucidated the varying distributions of the stress and strain components

as the crack extended. Crack tip parameters such as CTOA and F were found to be fairly constant during crack growth.

The proposed technique has several advantages. It is completely general, so that it can be used with different types of elements for simulating the crack growth. By incorporating the present algorithm into any finite element program, a gradual advance of the crack within an element may be achieved without having to re-arrange the grid of the finite element model. The use of the strain extrapolation scheme allows a relatively larger element size in the vicinity of the crack tip. Finally the adoption of the effective strain (a scalar quantity) as the fracture criterion makes it suitable for all modes of fracture analysis.

8.2 Recommendations

Results from this study were encouraging. With this experience in hand, the following recommendations with regard to further work in this area are in order.

(1) An in-depth study on the rupture strain value for a variety of geometries would establish firmly the validity of using $\bar{\varepsilon}_{rup.}$ as a fracture criterion.

(2) Although quite complicated and expensive, it would be most desirable to develop a three-dimensional elastic-plastic stress analysis program, which would permit more precise analysis of slant-type fracture problems.

(3) A more precise model for stable crack growth could be achieved by refining both the strain extrapolation scheme and the nodal force relaxation technique. Further precision may be attained through the implementation of an automatic load selection scheme.

(4) A step-by-step analysis using the nodal grafting technique [95] would determine the crack path under varying loading conditions.

(5) Finally, the implementation of creep analysis into the current program would establish a computational model for low-cycle fatigue in structures of complex geometry subjected to general loading conditions.

REFERENCES

[1] Knott, J.F., Fundamentals of Fracture Mechanics, Wiley, New York (1973).

[2] Brock, D., Elementary Engineering Fracture Mechanics, Noordhoff International Publishing, Leyden (1974).

[3] Kobayashi, A.S., Experimental Techniques in Fracture Mechanics, The Iowa State University Press, Ames (1975).

[4] Griffith, A.A., The Theory of Rupture , (Proceedings of International Conference of Applied Mechanics of Delft, 1924) edited by Biezeno and Burgers (1925), 55-63.

[5] Irwin, G.R., Analysis of Stresses and Strains Near the End of a Crack Traversing a Plate, Journal of Applied Mechanics, ASME Transaction 24 (1957), 361-364.

[6] Irwin, G.R., Kies, J.A. and Smith, H.L., Fracture Strengths Relative to Onset and Arrest of Crack Propagation, Proceeding of American Society for Testing and Materials 58 (1958), 640-660.

[7] Dugdale, D.S., Yielding of Steel Sheets Containing Slits, Journal of Mechanics and Physics of Solids 8 (1960), 100-104.

[8] Wells, A.A., Application of Fracture Mechanics at and Beyond General Yield, British Welding Research Association Report M13/63 (1963).

[9] Rice, J.R., Mathematical Analysis in the Mechanics of Fracture, Fracture: An Advanced Treatise, edited by Liebowitz, H., Academic Press, New York, Vol. 2 (1968), 191-311.

[10] Hutchinson, J.W., Singular Behavior at the End of a Tensile Crack in a Hardening Materials, Journal of Mechanics and Physics of Solids 16 (1968), 13-31.

[11] Rice, J.R. and Rosengren, G.F., Plane Strain Deformation Near a Crack Tip in a Power-Law Hardening material, Journal of Mechanics and Physics of Solids 16 (1968), 1-12.

[12] Paris, P.C., Fracture Mechanics in the Elastic-Plastic Regime, Flaw Growth and Fracture, ASTM STP 631 (1977), 3-27.

[13] Heyer, R.H., Crack Growth Resistance Curves (R-Curves) - Literature Review, Fracture Toughness Evaluation by R-Curve Methods, ASTM STP 527 (1973), 1-16.

[14] Carman, C.M., Plane Stress Fracture Testing Using Center Cracked Panels, Ibid., 62-84.

[15] Sullivan, A.M., Freed, C.N. and Stoop, J., Comparison of R-Curves Determined from Different Specimen Types, Ibid., 85-104.

[16] Frediani, A., An Evaluation of the Reliability of Fracture Mechanics Methods, Engineering Fracture Mechanics 14 (1981), 289-322.

[17] McClintock, F.A. and Irwin, G.R., Plasticity Aspects of Fracture Mechanics, Fracture Toughness Testing and Its Applications, ASTM STP 381 (1965), 84-113.

[18] Rice, J.R., Elastic-Plastic Models for Stable Crack Growth in Mechanics and Mechanisms of Crack Growth, (proceedings of Conference at Cambridge, England, April 1973), edited by M.J. May, British Steel Corporation Physical Metallurgy Centre Publication (1975), 14-39.

[19] Kobayashi, A.S., Maiden, D.E., Simon, B.J., Ilda, S., Application of Finite Element Analysis Method to Two-Dimensional Problems in Fracture Mechanics, ASME Paper No. 69-WA/PVP-12.

[20] Chan, S.K., Tuba, I.S. and Wilson, W.K., On the Finite Element Method in Linear Fracture Mechanics, Engineering Fracture Mechanics 2 (1970), 1-17.

[21] Watwood, V.B., The Finite Element Method for Prediction of Crack Behavior, Nuclear Engineering and Design 11 (1969), 323-332.

[22] Wilson, W.K., Some Crack Tip Finite Elements for Plane Elasticity, Stress Analysis and Growth of Cracks, ASTM STP 513 (1972), 90-105.

[23] Byskov, E., The Calculation of Stress Intensity Factors Using the Finite Element Method with Cracked Elements, International Journal of Fracture Mechanics 6 (1970), 159-167.

[24] Hilton, P.D. and Sih, G.C., Applications of the Finite Element Method to the Calculations of Stress Intensity Factors, Methods of Analysis and Solutions of Crack Problems, edited by Sih, G.C., Noordhoff International Publishing, Leyden (1973), 426-483.

[25] Tracey, D.M., Finite Elements for Determination of Crack Tip Elastic Stress Intensity Factors, Engineering Fracture Mechanics 3 (1971), 255-265.

[26] Henshell, R.D., Crack Tip Finite Elements are Unnecessary, International Journal for Numerical Methods in Engineering 9 (1975), 495-507.

[27] Barsoum, R.S., On the Use of Isoparametric Finite Elements in Linear Fracture Mechanics, International Journal for Numerical Methods in Engineering 10 (1976), 25-37.

[28] Barsoum, R.S., Triangular Quarter-Point Elements as Elastic and Perfectly-Plastic Crack Tip Elements, International Journal for Numerical Methods in Engineering 11 (1977), 85-98.

[29] Swedlow, J.L., Williams, M.L. and Yang, W., Elasto-Plastic Stresses and Strains in Cracked Plates, (proceedings of First International Conference on Fracture at Sendai, Japan, 1965), edited by Yokobori, T. et al, Japan Society for Strength and Fracture, Tokyo, Vol. 1 (1966), 259-282.

[30] Swedlow, J.L., Elasto-Plastic Cracked Plates in Plane Strain, International Journal of Fracture Mechanics 5 (1969), 33-44.

[31] Swedlow, J.L., Initial Comparisons between Experiment and Theory of the Strain Fields in a Cracked Copper Pla te, International Journal of Fracture Mechanics 5 (1969), 25-31.

[32] Marcal, P.V. and King, I.P., Elastic-Plastic Analysis of Two-Dimensional Systems by the Finite Element Method, International Journal of Mechanical Science 9 (1967), 143-155.

[33] Miyamoto, H., Shiratori, M. and Miyoshi, T., Elastic-Plastic Response at the Tip of a Crack, in Mechanical Behavior of Materials (Proceedings of the Second International Conference on Fracture), Society of Materials Science, Japan, Vol. 1 (1972), 433-445.

[34] Larsson, S.G. and Carlsson, A.J., Influence of Non-Singular Stress Terms and Specimen Geometry on Small-Scale Yielding at Crack Tips in Elastic-Plastic Materials, Journal of the Mechanics and Physics of Solids 21 (1973), 263-277.

[35] Levy, N., Marcal, P.V., Ostergren, W.J. and Rice, J.R., Small Scale Yielding Near a Crack in Plane Strain: A Finite Element Analysis, International Journal of Fracture Mechanics 7 (1971), 143-156.

[36] Rice, J.R. and Tracey, D.M., Computational Fracture Mechanics, in Numerical and Computer Methods in Structural Mechanics (edited by S.J. Fenves et al.), Academic Press (1973), 585-623.

[37] Tracey, D.M., Finite Element Solutions for Crack Tip Behavior in Small Scale Yielding, Journal of Engineering Materials and Technology, ASME Transaction 98 (1976), 146-151.

[38] McMeeking, R.M., Finite Deformation Analysis of Crack Tip Opening in Elastic-Plastic Materials and Implications for Fracture Initiation, Journal of the Mechanics and Physics of Solids 25 (1977), 357-381.

[39] Rice, J.R., McMeeking, R.M., Parks, D.M. and Sorenson, E.P., Recent Finite Element Studies in Plasticity and Fracture Mechanics, Computer Methods in Applied Mechanics and Engineering 17/18 (1979), 411-442.

[40] Wells, A.A., Crack Opening Displacements from Elastic-Plastic Analysis of Externally Notched Tension Bars, Engineering Fracture Mechanics 1 (1969), 399-410.

[41] Turner, C.E. and Cheung, J.S.T., Computation of Post-Yield Behavior in Notch Bend and Tension Test Pieces, Journal of Strain Analysis 7 (1972), 303-312.

[42] Sumpter, J.D.G. and Turner, C.E., Use of the J Contour Integral in Elastic-Plastic Fracture Studies by Finite-Element Methods, Journal of Mechanical Engineering Science 18 (1976), 97-112.

[43] Parks, D.M., Virtual Crack Extension in a General Finite Element Technique for J-Integral Evaluation, Numerical Methods in Fracture Mechanics, edited by A.R. Luxmoore and M.J. Owen, University College of Swansea (1978), 464-478.

[44] Miyamoto, H. and Kageyama, K., Extension of J-Integral to the General Elasto-Plastic Problem and Suggestion of a New Method for its Evaluation, Ibid., 479-486.

[45] Kobayashi, A.S., Chiu, S.T. and Beenorkes, R., A Numerical and Experimental Investigation on the Use of the J-Integral, Engineering Fracture Mechanics 5 (1973), 293-305.

[46] Andersson, H., A Finite-Element Representation of Stable Crack-Growth, Journal of Mechanics and Physics of Solids 21 (1973), 337-356.

[47] Hsu, T.R. and Bertels, A.W.M., Propagation and Opening of a Through Crack in a Pipe Subjected to Combined Cyclic Thermomechanical Loading, Journal of Pressure Vessel Technology, ASME Transaction 98 (1976), 17-25.

[48] de Koning, A.U., Fracture 1977, (Proceedings of the Fourth International Conference on Fracture, University of Waterloo, June 1977), University of Waterloo Press, Vol. 3, 25-31.

[49] Varanasi, S.R., Analysis of Stable and Catastrophic Crack Growth Under Rising Load, Flaw Growth and Fracture, ASTM STP 631 (1977), 507-519.

[50] de Koning, A.U., Rooke, D.P. and Wheeler, C., Energy Dissipation During Stable Crack Growth in Aluminum Alloy 2024-T3, (Proceedings of International Conference on Numerical Methods in Fracture Mechanics, Swanesea, January 1978), edited by A.R.Luxmoore and D.R.J. Owen, 525-536.

[51] Light, M.F. and Luxmoore, A.R., A Numerical Investigation of Post-Yield Fracture, Journal of Strain Analysis 12 (1977), 293-304.

[52] Light, M.F. and Luxmoore, A.R., Crack Extension Forces in Elasto-Plastic Stress Fields, Journal of Strain Analysis 12 (1977), 305-309.

[53] Belie, R.G. and Reddy, J.N., Direct Prediction of Fracture for Two-Dimensional Plane Stress Structures, Computers & Structures 11 (1980), 49-53.

[54] Lee, J.D. and Liebowtiz, H., Considerations of Crack Growth and Plasticity in Finite Element Analysis, Computers & Structures 8 (1978), 403-410.

[55] Kfouri, A.F. and Miller, K.J., Crack Separation Energy Rates in Elastic-Plastic Fracture Mechanics, Proceedings of Institute of Mechanical Engineers (1976), 48-76.

[56] Rice, J.R. and Sorensen, E.P., Continuing Crack-Tip Deformation and Fracture for Plane-Strain Crack Growth in Elastic-Plastic Solids, Journal of Mechanics and Physics of Solids 26 (1978), 163-186.

[57] Shih, C.F., deLorenzi, H.G. and Andrews, W.R., Studies on Crack Initiation and Stable Crack Growth, Elastic-Plastic Fracture, ASTM STP 668 (1979), 65-120.

[58] Kanninen, M.F., Rybicki, E.E., Stonesifer, R.B., Broek, D., Rosenfield, A.R., Marshall, C.W. and Hahn, G.T., Elastic-Plastic Fracture Mechanics for Two-Dimensional Stable Crack Growth and Instability Problems, Ibid., 121-150.

[59] Sorensen, E.P., A Numerical Investigation of Plane Strain Stable Crack Growth Under Small-Scale Yielding Conditions, Ibid., 151-174.

[60] D'Escatha, Y. and Devaux, J.C., Numerical Study of Initiation, Stable Crack Growth, and Maximum Load, with a Ductile Fracture Criterion Based on the Growth of Holes, Ibid., 229-248.

[61] Newman, J.C., Jr., Finite Element Analysis of Crack Growth Under Monotonic and Cyclic Loading, Cyclic Stress-Strain and Plastic Deformation Aspects of Fatigue Crack Growth, ASTM STP 637 (1977), 56-80.

[62] Ohji, K., Ogura, K. and Ohkubo, Y., Cyclic Analysis of a Propagating Crack and its Correlation with Fatigue Crack Growth, Engineering Fracture Mechanics 7 (1975), 457-464.

[63] Socie, D.F., Prediction of Fatigue Crack Growth in Notched Members under Variable Amplitude Loading Histories, Engineering Fracture Mechanics 9 (1977), 849-865.

[64] Zienkiewicz, O.C., The Finite Element Method in Engineering Science, McGraw-Hill, London (1971).

[65] Desai, C.S. and Abel, J.F., Introduction to the Finite Element Method, Van Nostrand Reinhold Company, New York (1972).

[66] Ueda, Y. and Yamakawa, T., Thermal Non-Linear Behaviour of Structures, in Computational Methods in Structural Mechanics and Design, edited by Oden, Clough and Yamamoto,University of Alabama Press (1972), 375-392.

[67] Yamada, Y. and Yoshimura, N. and Sakurai, T., Plastic Stress-Strain Matrix and its Application for the Solution of Elastic-Plastic Problems by the Finite Element Method, International Journal of Mechanical Science 10 (1968), 343-354.

[68] Zienkiewicz, O.C., Valliappan, S. and King, I.P., Elasto-Plastic Solutions of Engineering Problems 'Initial Stress', Finite Element Approach, International Journal for Numerical Methods in Engineering 1 (1967), 75-100.

[69] Nayak, G.C. and Zienkiewicz, O.C., Elasto-Plastic Stress Analysis, A Generalization for Various Constitutive Relations Including Strain Softening, International Journal for Numerical Methods in Engineering 5 (1972), 113-135.

[70] Swedlow, J.L., A Procedure for Solving Problems of Elasto-Plastic Flow, Computers and Structures 3 (1973), 879-898.

[71] Hsu, T.R., Bertels, A.W.M., Banerjee, S. and Harrison, W.C., Theoretical Basis for a Transient Thermal Elasto-Plastic Stress Analysis of Nuclear Reactor Fuel Element, Whiteshell Nuclear Research Establishment Report AECL-5233, Atomic Energy of Canada (1976).

[72] Wu, R.Y., On the Application of Fourier Expansion to Elasto-plastic Finite Element Stress Analysis, M.Sc. Thesis. Department of Mechanical Engineering, University of Manitoba,Canada (1977).

[73] Cheng, S.Y. and Hsu, T.R., On Elasto-Plastic Stress-Strain Relationship for Multi-Axial Stress States, International Journal for Numerical Methods in Engineering 12 (1978), 1617-1622.

[74] Schaeffer, B.J., Liu, H.W. and Ke, J.S., Deformation and the Strip Necking Zone in a Cracked Steel Sheet, Experimental Mechanics 11 (1971), 172-175.

[75] Gavigan, W.J., Ke, J.S. and Liu, H.W., Local and Gross Deformations in Cracked Metallic Plates, International Journal of Fracture 9 (1973), 255-266.

[76] Evans, W.T., Light, M.F. and Luxmoore, A.R., An Experimental and Finite Element Invetigation of Fracture in Aluminum Thin Plates, Journal of Mechanics and Physics of Solids 28 (1980), 167-189.

[77] Dieter, G.E., Mechanical Metallurgy, McGraw-Hill, New York (1976).

[78] Bazant, Z.P. and Cedolin, L., Blunt Crack Band Propagation in Finite Element Analysis, Journal of the Engineering Mechanics Division, ASCE Transaction, 105 (1979), 297-315.

[79] Nair, P. and Reifsnider, K.L., Unimod: An Applications Oriented Finite Element Scheme for the Analysis of Fracture Mechanics Problems, Fracture Analysis, ASTM STP 560, American Society for Testing and Materials (1974), 211-225.

[80] Hsu, T.R. and Kim, Y.J., On Slow Crack Growth in Fuel Cladding by Finite Element Analysis, C3/12, 5th International Conference on Structural Mechanics in Reactor Technology (1979).

[81] Dorn, W.S. and McCracken, D.D., Numerical Methods with Fortran IV Case Study, John Wiley & Sons, New York, (1972).

[82] Tentative Recommended Practise for R-Curve Determination, Fracture Mechanics Test Methods Standardization, ASTM STP 632 (1977), 241-259.

[83] Brickstad, B. and Nilsson, F., Numerical Evaluation by FEM of Crack Propagation Experiments, International Journal of Fracture 16 (1980), 71-84.

[84] Erdogan, F., Sih, G.C., On The Crack Extension in Plates Under Plane Loading and Transverse Shear, Journal of Basic Engineering, ASME Transaction 85 (1963), 519-527.

[85] Williams, J.G. and Ewing, P.D., Fracture Under Complex Stress - The Angled Crack Problems, International Journal of Fracture 8 (1972), 441-446.

[86] Maiti, S.K. and Prasad, K.S.R.K., A Study on the Theories of Unstable Crack Extension for the Prediction of Crack Trajectories, International Journal of Solids and Structures, 16 (1980), 563-574.

[87] Maiti, S.K., Prediction of the Path of Unstable Extension of Internal and Edge Cracks, Journal of Strain Analysis 15 (1980), 183-194.

[88] Sih, G.C., Some Basic Problems in Fracture Mechanics and New Concepts, Engineering Fracture Mechanics 5 (1973), 365-377.

[89] Sih, G.C., Fracture Mechanics Applied to Engineering Problems - Strain Energy Density Fracture Criterion, Engineering Fracture Mechanics 6 (1974), 361-386.

[90] Kipp, M.E. and Sih, G.C., The Strain Energy Density Failure Criterion Applied to Notched Elastic Solids, International Journal of Solids and Structures 12 (1975), 153-173.

[91] Mau, S.T. and Yang, M.S., Some Application of a Hybrid Finite Element Method to Crack Problems, Proceedings of International Conference on Fracture Mechanics and Technology (edited by G.C. Sih and C.L. Chow), Sigthoff and Noordhoff, Alphan aan den Rijn, Vol. 2 (1977), 1467-1482.

[92] Hussain, M.A., Pu, S.L. and Underwood, J., Strain Energy Release Rate for a Crack under Combined Mode I and Mode II, Fracture Analysis, ASTM STP 560, American Society for Testing and Materials (1974), 2-28.

[93] Palaniswamy, K. and Knauss, W.G., Propagation of a Crack Under General, In-Plane Tension, International Journal of Fracture 8 (1972), 114-117.

[94] Hellen, T.K., On the Method of Virtual Crack Extensions, International Journal for Numerical Method in Engineering 9 (1975), 187-207.

[95] Ingraffea, A., Nodal Grafting for Crack Propagation Studies, International Journal for Numerical Method in Engineering 11 (1977), 1185-1187.